



**DIFFRACTION IMAGING:  
A STRATTON FIELD, TX CASE STUDY**

-----  
A Thesis Presented to  
the Faculty of the Department of Earth and Atmospheric Sciences  
University of Houston

-----  
In Partial Fulfillment  
of the Requirements for the Degree  
Master of Science

-----  
By  
Alejandro E. Juranovic

May 2013

**DIFFRACTION IMAGING:  
A STRATTON FIELD, TX CASE STUDY**

---

**Alejandro Juranovic**

APPROVED:

---

**Dr. John P. Castagna**

---

**Dr. Alexander Mihai Popovici**

---

**Dr. Robert Stewart**

---

**Dean of College of Natural Sciences and Mathematics**

## **ACKNOWLEDGEMENTS**

I would like to thank my advisor Dr. John Castagna and my committee members Dr. Alexander Mihai Popovici and Dr. Robert Stewart for believing in me, guiding me and teaching me so much. I would also like to thank my former advisor Dr. Chris Liner and Paul Murray from University of Texas, Austin for their time and dedication, especially for helping me to have access to the dataset. I am very grateful for having the unconditional support Dr. Sven Treitel, Dr. Emir Tavella, and Mr. Thomas Sawyer. They've opened the doors to make this personal achievement possible recommending me with a letter to the University of Houston.

I thank Z-Terra, Inc. for providing me the Migration and Diffraction Imaging software and the staff for helping me, guiding me and supporting me for so many hours. I would like to thank Lumina Geophysical, LLC. and their staff for providing software and knowledge for the interpretation stage of my work, especially to Carlos Moreno and Miguel Silva for his support. I would like to thank Hernan Reijenstein and Gisela Porfiri for teaching and helping me in the interpretation and discussion of the results of this work.

I would like to extend my greatest gratitude to DataSeismic Geophysical Services for sponsoring me, supporting me financially, for allowing me to use their facilities, software, hardware, and know-how. I want to thank two special ones who supported me,

helped me, mentored me, taught me geophysics from scratch, guided me, and no matter what, they have been always believed in me. It is invaluable the opportunity they gave to me. This is for you Raul Stolarza and Santiago Juranovic. I enjoyed, I enjoy, and I will enjoy growing as a professional and as a person next to you. I have no words to express my gratitude.

I want to thank my friends, classmates, colleagues, and especially my Houston family for those endless hours of support and care. Each member of my family in Argentina has supported and loved me since the very beginning of my journey, for that I am truly grateful.

Finally, I want to thank my lovely wife, Solange. She means everything to me. Her endless guidance, advice, support, kindness, wisdom, and love has no equal. Without her, I could not achieve this precious goal. Thank you so much for all these years.

**DIFFRACTION IMAGING:  
A STRATTON FIELD, TX CASE STUDY**

---

An Abstract of a Thesis

Presented to

the Faculty of the Department of Earth and Atmospheric Sciences

University of Houston

---

In Partial Fulfillment

of the Requirements for the Degree

Master of Science

---

By

Alejandro E. Juranovic

May 2013

## ABSTRACT

In recent years the Oil & Gas Industry has been searching for new technologies to increase 3D seismic resolution and fracture detection for shale unconventional reservoirs. Since most shale reservoirs are thin-layered and below seismic resolution there is a need of a new technology capable of resolving thin shale layers and small-scale faults and fractures. In this study, I will introduce, the concept of **super-resolution** and diffraction imaging to address the recovery of sub-resolution scale features in seismic imaging going beyond the well-known Rayleigh resolution limit of half the seismic wavelength (quarter of a wavelength for a two-way time).

A 3D seismic survey from Stratton Field, TX, shot by the Bureau of Economic Geology (BEG) was used to analyze and discuss the results obtained after performing a complete PSTM, PSDM and Diffraction Imaging sequence. The Stratton Field geology does not have complex structures nor salt domes. It is a vertical succession of sand-shale sequences with two major growth faults and several secondary antithetic faults that produce reservoir compartmentalization. The Diffraction Imaging results showed interesting features not seen in the PSDM and the similarity volumes. It was able to image under-resolution discontinuities that could be interpreted as faults.

After analyzing the results and observing the improvement in the image, it is recommended the use of Diffraction Imaging as a complementary tool to conventional PSTM and PSDM sequences, especially in thin-layered shale reservoirs where the identification of faults is one of the main goals. The details obtained in the image helped

to interpret the seismic volume and the idea of imaging discontinuities beyond the Rayleigh limit of resolution was supported using a synthetic model showing a very similar case.

## TABLE OF CONTENTS

1. CHAPTER 1: INTRODUCTION	
1.1. Introduction .....	01
1.2. Geological Setting .....	04
1.3. Data Description .....	13
1.4. Objectives .....	16
2. CHAPTER 2: THEORY AND IMPLEMENTATION	
2.1. Prestack Depth Migration .....	18
2.1.1. Ray-based Methods .....	19
2.1.1.1. Kirchhoff Migration .....	19
2.1.1.2. Beam Migration .....	20
2.1.2. Wave-equation-based Methods .....	20
2.1.2.1. One-way Migration .....	20
2.1.2.2. Two-way Migration .....	22
2.2. Diffraction Imaging .....	26
2.2.1. Definitions .....	26
2.2.2. Geometrical Aspects .....	27
2.2.3. Diffractions and Super-resolution .....	29
2.2.4. Theory and Method .....	31
2.2.5. Application .....	34
3. CHAPTER 3: APPLICATION AND RESULTS	
3.1. Methodology .....	41
3.1.1. Time Processing and Interpretation .....	41
3.1.2. Depth Imaging and Interpretation .....	49
3.1.3. Diffraction Imaging and Interpretation .....	56
3.2. Results .....	61
4. CHAPTER 4: CONCLUSIONS .....	79
5. APPENDIX: SEISMIC PROCESSING REPORT .....	82
5.1. Table of Contents .....	83
5.2. PSTM Final Processing Sequence .....	94
5.3. Deliverables .....	97
5.4. List of Figures .....	98
6. REFERENCES .....	136

## LIST OF FIGURES

Figure 1	<i>Index maps showing the location of the Stratton and Agua Dulce Fields, the Union Pacific Resources and the Bureau of Economic Geology seismic surveys, and the well in which the VSP survey was run. Modified from El-Mowafy, and Marfurt (2008) .....</i>	5
Figure 2	<i>Schematic 3-D reconstruction of the fluvial facies architecture interpreted for the BMF sequence, Stratton and Agua Dulce fields, south Texas. From El-Mowafy, and Marfurt (2006) .....</i>	7
Figure 3	<i>(a) Vertical slice from the migrated 3-D data crossing the VSP control well showing two continuous Frio reflection events (b) SP data from well Wardner 175 showing different reservoirs in Stratton Field. Modified from Hardage et al. (1994).....</i>	8
Figure 4	<i>Geologic cross-section showing the disparity in thickness of the BMF interval (MTE41-MTG2) on both sides of the AD Fault. The hanging wall is deformed by the rollover anticline and a set of synthetic and antithetic faults. (b) Coincident seismic line from the UPR 3D survey showing the AD listric normal fault and the associated structures. Displacement on the AD growth fault occurs during sedimentation, resulting in equivalent beds being thicker in the hanging-wall block than in the footwall block. El-mowafy and Marfurt (2008) .....</i>	9
Figure 5	<i>Time structure map constructed on top of the F11 horizon from the BEG and the UPR 3D surveys. Fault polygons indicate the locations of the major faults and several secondary faults. These secondary faults were not shown before at the F11 stratigraphic level. Modified from El-Mowafy and Marfurt (2008).....</i>	10
Figure 6	<i>(a) Seismic crossline from the UPR 3D survey showing the deformation on the hanging-wall side of the AD fault. All subsidiary faults are affecting the deeper middle Frio (G2-F11). (b) Another seismic crossline from the same survey showing deformation in the footwall block of the AD fault. Modified El-Mowafy and Marfurt (2008).....</i>	12
Figure 7	<i>Base Map showing the 21 available wells .....</i>	14
Figure 8	<i>Map showing wells and VSP locations. Modified from Hardage et al. (1994) .....</i>	15
Figure 9	<i>The downward-continuation operation of one-way wave-equation migration. For each frequency component, the recorded wavefield is downward-continued recursively from one depth to the next greater depth using the one-way wave equation. From Etgen, Gray, and Zhang (2009) .....</i>	21
Figure 10	<i>(a) Kirchhoff Migration. Modified Etgen, Gray, and Zhang (2009).....</i>	23

Figure 10	<i>(b) Beam Migration. Modified from Etgen, Gray, and Zhang (2009) .....</i>	24
Figure 10	<i>(c) One-way Wave-Equation Migration. Modified from Etgen, Gray, and Zhang (2009).....</i>	25
Figure 10	<i>(d) Two-way Wave-Equation Migration or Reverse Time Migration. Modified from Etgen, Gray, and Zhang (2009).....</i>	26
Figure 11	<i>Geometry of reflection and diffraction. S, R denote source and receiver locations, respectively; S' the imaginary reflection source; A the reflection/diffraction hyperbola apex; and t the travelttime. (a) Reflections on a horizontal plane reflector. (b) Reflections on a strongly curved reflector. (c) Reflections on a dipping reflector. (d) Diffractions on a point diffractor (denoted by D). Khaidukov et al. (2004) .....</i>	28
Figure 12	<i>Common data point gather at distance=3.5 km in the model of Fig. 1, after NMO correction with constant velocity. Modified Moser and Howard (2008) .....</i>	30
Figure 13	<i>Two-layer model with curved and faulted interfaces. Velocities within the layers are constant and equal to 2500 m/s and 2700 m/s. The fault offset is 20 m. Khaidukov et al. (2004) .....</i>	35
Figure 14	<i>One of the shot gathers over Figure 13. Modified from Khaidukov et al. (2004) .....</i>	35
Figure 15	<i>Depth migration of full-wave shot gathers. Khaidukov et al. (2004) .....</i>	36
Figure 16	<i>Shot gather of Figure 14 with reflections suppressed. Modified Khaidukov et al. (2004).....</i>	37
Figure 17	<i>Depth migration of diffraction shot gathers. Fault positions as well as reflector edges are clearly visible (and easy to interpret) compared to Figure 15. Modified from Khaidukov et al. (2004) .....</i>	37
Figure 18	<i>Zoom on full-wave image (top, zoom from Figure 15) and diffraction image (bottom, zoom from Figure 17) at (1000 m, 1200 m). The diffraction image allows for a much better and less ambiguous interpretation of the fault geometry than the full-wave image. Modified from Khaidukov et al. (2004).....</i>	38
Figure 19	<i>Velocity Model and Synthetic shot gather from the point above the intersection of the two slides. Modified from Sturzu et al. (2012).....</i>	39
Figure 20	<i>Kirchhoff migration stack using the exact velocity model and Offset gather in the location of the shot. Modified from Sturzu et al. (2012) .....</i>	40
Figure 21	<i>Diffraction imaging migration result and offset gather for the same location as Figure 20. Modified from Sturzu et al. (2012).....</i>	40

Figure 22	<i>Conventional Time Processing Sequence</i> .....	43
Figure 23	<i>Fold Map with IL and XL Distribution</i> .....	44
Figure 24	<i>PSTM Stack – IL 80</i> .....	44
Figure 25	<i>PSTM Stack – XL 110</i> .....	45
Figure 26	<i>PSTM Stack – IL 45 with WELL_07 and Interpretation</i> .....	45
Figure 27	<i>Synthetic Seismogram in WELL_07 created with the velocity from resistivity log</i> .....	47
Figure 28	<i>Synthetic Seismogram in WELL_07 created with the velocity from density log</i> .....	47
Figure 29	<i>PSTM Stack - Time Slice at 1800 ms</i> .....	48
Figure 30	<i>PSTM Stack after ESP - Time Slice at 1800 ms</i> .....	49
Figure 31	<i>Depth Imaging Processing Sequence</i> .....	50
Figure 32	<i>Initial Velocity Model from the Time Processing – IL 76 (from ZTK)</i> .....	51
Figure 33	<i>Final Velocity Model in Depth – IL 76 (from ZTK)</i> .....	52
Figure 34	<i>(a) Interpretation done in Time</i> .....	53
Figure 34	<i>(b) Interpretation done in Depth</i> .....	54
Figure 35	<i>(a) PSDM Stack - Depth Slice at 7230 ft</i> .....	55
Figure 35	<i>(b) PSDM Stack after ESP - Depth Slice at 7230 ft</i> .....	56
Figure 36	<i>Diffraction Imaging Processing Sequence</i> .....	58
Figure 37	<i>The specularity taper Function (ZTK Manual, Sturzu, I., Popovici, A. M. and Musat, I.)</i> .....	58
Figure 38	<i>Diffraction Imaging Stack - Depth Slice at 7230 ft</i> .....	60
Figure 39	<i>(a) PSDM Volume - Horizon Slice at Formation F39</i> .....	62
Figure 39	<i>(b) DI Volume - Horizon Slice at Formation F39</i> .....	63
Figure 40	<i>(a) PSTM Volume – IL 64</i> .....	64

Figure 40	<i>(b) PSDM Volume – IL 64</i> .....	65
Figure 40	<i>(c) DI Volume – IL 64</i> .....	66
Figure 41	<i>(a) PSTM Volume – XL 100</i> .....	67
Figure 41	<i>(b) PSDM Volume – XL 100</i> .....	68
Figure 41	<i>(c) DI Volume – XL 100</i> .....	69
Figure 42	<i>PSDM Stack - Horizon Slice at Formation F11</i> .....	70
Figure 43	<i>PSDM Stack after ESP - Horizon Slice at Formation F11</i> .....	71
Figure 44	<i>Diffraction Imaging - Horizon Slice at Formation F11</i> .....	72
Figure 45	<i>Diffraction Imaging - Horizon Slice at Formation F11 with IL 99 showing the discontinuity</i> .....	73
Figure 46	<i>PSDM Stack - Horizon Slice at Formation C38</i> .....	74
Figure 47	<i>PSDM Stack after ESP - Horizon Slice at Formation C38</i> .....	75
Figure 48	<i>Diffraction Imaging Stack - Horizon Slice at Formation C38</i> .....	76
Figure 49	<i>Diffraction Imaging - Horizon Slice at Formation C38 with an Arbitrary Line showing a possible discontinuity</i> .....	77
Figure 50	<i>Cross-section of PSDM Volume (top) and Diffraction Imaging (bottom) – Formation C38 (Orange)</i> .....	78
Figure A1	<i>Shot before shot domain noise attenuation</i> .....	99
Figure A2	<i>Shot after shot domain noise attenuation</i> .....	100
Figure A3	<i>Attenuated noise</i> .....	101
Figure A4	<i>Base Map</i> .....	102
Figure A5	<i>Processing grid</i> .....	103
Figure A6	<i>Fold map</i> .....	104
Figure A7	<i>Topography map</i> .....	105
Figure A8	<i>Refraction Statics map</i> .....	106
Figure A9	<i>First Residual Statics map</i> .....	107

Figure A10	<i>Second Residual Statics map</i> .....	108
Figure A11	<i>Location of IL 70 and XL 110</i> .....	109
Figure A12	<i>Brute stack with Elevation Statics – IL 70</i> .....	110
Figure A13	<i>Brute stack with Refraction Statics – IL 70</i> .....	111
Figure A14	<i>Stack with First Velocity Analysis and Residual Statics – IL 70</i> .....	112
Figure A15	<i>Stack with Second Velocity Analysis and Residual Statics – IL 70</i> .....	113
Figure A16	<i>Final Stack – IL 70</i> .....	114
Figure A17	<i>Post-stack Migration – IL 70</i> .....	115
Figure A18	<i>PSTM Stack – IL 70</i> .....	116
Figure A19	<i>Brute stack with Elevation Statics – XL 110</i> .....	117
Figure A20	<i>Brute stack with Refraction Statics – XL 110</i> .....	118
Figure A21	<i>Stack with First Velocity Analysis and Residual Statics – XL 110</i> .....	119
Figure A22	<i>Stack with Second Velocity Analysis and Residual Statics – XL 110</i> .....	120
Figure A23	<i>Final Stack – XL 110</i> .....	121
Figure A24	<i>Post-stack Migration – XL 110</i> .....	122
Figure A25	<i>PSTM Stack – XL 110</i> .....	123
Figure A26	<i>PSTM stack -Time Slice 750 ms</i> .....	124
Figure A27	<i>PSTM stack -Time Slice 1000 ms</i> .....	125
Figure A28	<i>PSTM stack -Time Slice 1250 ms</i> .....	126
Figure A29	<i>PSTM stack -Time Slice 1500 ms</i> .....	127
Figure A30	<i>PSTM stack -Time Slice 1750 ms</i> .....	128
Figure A31	<i>PSTM stack -Time Slice 2000 ms</i> .....	129
Figure A32	<i>PSTM stack -Time Slice 2250 ms</i> .....	130
Figure A33	<i>PSTM stack -Time Slice 2500 ms</i> .....	131

Figure A34	<i>PSTM stack -Time Slice 2750 ms</i> .....	132
Figure A35	<i>PSTM stack -Time Slice 3000 ms</i> .....	133
Figure A36	<i>PSTM stack -Time Slice 3250 ms</i> .....	134
Figure A37	<i>PSTM stack -Time Slice 3500 ms</i> .....	135

## LIST OF ABBREVIATIONS

<b>ABA</b>	Air Blast Attenuation
<b>AD</b>	Agua Dulce Growth Fault
<b>AGC</b>	Automatic Gain Control
<b>BEG</b>	Bureau of Economic Geology
<b>BMF</b>	Basal part of the middle Frio Formation
<b>CVS</b>	Constant Velocity Stack
<b>DECON</b>	Surface Consistent Deconvolution
<b>DI</b>	Diffraction Imaging
<b>ESP</b>	Event Similarity Prediction
<b>GLI</b>	Generalized Linear Inversion
<b>GRI</b>	Gas Research Institute
<b>IL</b>	In-line
<b>NMO</b>	Normal Moveout
<b>PSDM</b>	Prestack Depth Migration
<b>PSTM</b>	Prestack Time Migration
<b>RMS</b>	Root Mean Square
<b>SCAC</b>	Surface Consistent Amplitude Compensation
<b>TAR</b>	True Amplitude Recovery
<b>VSP</b>	Vertical Seismic Profile
<b>XL</b>	Cross-line

## LIST OF EQUATIONS

Equation 1	<i>Common-shot Kirchhoff Migration (Schneider, 1978)</i> .....	19
Equation 2	<i>One-way wave-equation Migration: Downward continuation of recorded wavefield “U”</i> .....	20
Equation 3	<i>One-way wave-equation Migration: Downward continuation of source wavefield “D”</i> .....	20
Equation 4	<i>One-way wave-equation Migration: Image Condition (Claerbout 1971)</i> .....	21
Equation 5	<i>Two-way wave-equation Migration</i> .....	22
Equation 6	<i>Conventional Kirchhoff Migration</i> .....	31
Equation 7	<i>Traveltimes Function</i> .....	32
Equation 8	<i>Modified Kirchhoff Diffraction Imaging</i> .....	32
Equation 9	<i>Diffraction Imaging Weight Function</i> .....	33
Equation 10	<i>Gradient of traveltimes from source to image point</i> .....	33
Equation 11	<i>Gradient of traveltimes from image point to receiver</i> .....	33
Equation 12	<i>Normal Vector: Angle bisector of the wave vectors for the incoming and outgoing waves</i> .....	33
Equation 13	<i>Faust’s Empirical Equation</i> .....	46
Equation 14	<i>Gardner’s Equation</i> .....	46
Equation 15	<i>Inverted Gardner’s Equation</i> .....	46

# CHAPTER 1: INTRODUCTION

## 1.1. Introduction

In the last two decades the focus in the Direct Hydrocarbon Indicators (DHI) such as Amplitude vs. Offset (AVO) or Impedance Inversion (EI) analysis among others, and the need of higher resolution studies to identify complex features drove seismic data processors to change their workflows and improve algorithms in order to maintain the relative amplitude and waveform, allowing interpreters to perform their analysis based on more reliable and accurate geological-geophysical models.

According to Sturzu et al. (2012), in the last ten years the shale gas grew up from 1 to 30 percent of the American gas supplies, and it keeps increasing. Usually shale formations are just a few hundred feet (approximately 100 meters) thick, and the need for higher resolution it's now a reality. The production and recovery efficiency of these reservoirs is based on the accuracy of the drilling and hydraulic fracturing (commonly known as fracking). The natural faults are the main target to identify before drilling, helping to reduce cost and decreasing the environmental impact of developing the field with the use of fewer wells.

The difference in the seismic response of shale reservoirs (unconventional) compared with sand reservoirs creates the necessity of new technology able to resolve

thin shale layers and small scale fractures. Diffraction Imaging in depth could be used to complement conventional processing by adding a high resolution unconformities volume that could represent small faults, pinch-outs or salt flanks.

The theory of Diffraction Imaging will be address in the Chapter 2, but in order to keep the reader interested we will explain just a few ideas. The first one is **Diffraction Imaging**, which can be defined as the process of using diffractions to focus and image the structural element that produces diffraction surfaces. Since the diffractions, by definition, are smaller than the wavelength, we will introduce our second idea of **super-resolution**, which refers to the recovery of sub-wavelength scale details in the seismic image going beyond the well-known Rayleigh limit of half the seismic wavelength (quarter of a wavelength for a two-way time).

According to Khaidukov, Landa and Moser (2004) there is no sharp difference between reflections and diffractions, rather than extreme cases of the same backscattering phenomenon. We will have to rely on the difference in the move-out and the position of the traveltime apex in the shot gather to differentiate one from the other.

Several techniques for diffraction imaging have been proposed by Khaidukov, Landa, and Moser (2004), Taner, Fomel and Landa (2006), and Moser and Howard (2008). Another approach to Diffraction Imaging have been proposed by Berkovitch et al. (2009) using diffraction multifocusing stack to separate diffractions and reflections. This

work will be based on the method proposed by Moser and Howard (2008) and Moser (2009) and implemented as a modified Kirchhoff migration by Z-Terra Inc.

Through this work we will use 92-BEG 3D survey from Stratton Field located in Kleberg and Nueces counties, South Texas, shot by the Texas Bureau of Economic Geology (BEG) in 1992. This is a very well-known area with dozens of geophysical and geological papers. The main characteristic of this area is the amount of faults present that creates many compartmented reservoirs. In the geologic setting we will show the geological model proposed by El-Mowafy and Marfurt (2008) and it will be evident the necessity of high resolution image since the reservoir units to be analyzed are thin compartmented layers.

We will try to achieve a better definition, positioning, and understanding of the faults by combining the structural images from the Prestack Time Migration (PSTM), the improved image from the Prestack Depth Migration (PSDM) and the super-resolution unconformities from the Diffraction Imaging (DI).

We will show the main steps of a conventional processing sequence in time highlighting the processes that enhance the lateral coherency of reflections, but attenuates the diffractions. The difference in the move-out between reflections and diffractions will be a key point to identify those processes that could hurt the diffractions. ProMAX/SeisSpace, Focus/Echos and Seismic Studio will be used for the Prestack Time

Migration (PSTM) sequence. Since the proposed Diffraction Imaging method is a modification of the full wave Kirchhoff migration, we will explain the basic concepts of migration and the different types of the depth imaging techniques. We will perform a Prestack Depth Migration (PSDM) sequence using ZTK from Z-Terra, Inc. followed by the Diffraction Imaging.

## **1.2. Geological Setting**

The Stratton Field (Figure 1) is located in Kleberg and Nueces Counties, South Texas. This area consists of multiple vertically-stacked sand-shale sequences. The characteristics of this field have been addressed by El-Mowafy and Marfurt (2008) identifying a complex channel system with two major growth faults and several secondary faults creating reservoir compartments (Figure 2).

The Oligocene middle Frio formation, one of the major Tertiary progradational wedges of the Texas Gulf coastal plain, is a major hydrocarbon producer in the U.S. Gulf Coast. According to Galloway, Hobday and Magara (1982) it consists of deposits of two large fluvial and associated deltaic systems centered in the Houston embayments. The complex internal architecture of the middle Frio fluvial reservoirs along with the structural complexity caused by growth faults may result in bypassed reservoirs or compartments with additional reserves.

El-Mowafy and Marfurt (2008) counted with 92-BEG 3D (7.6 sq mi shot by BEG covering Stratton Field) and 93-UPR 3D (90 sq mi shot by Anadarko covering Agua Dulce Field) surveys allowing them to analyze and understand the geologic setting with more detail.

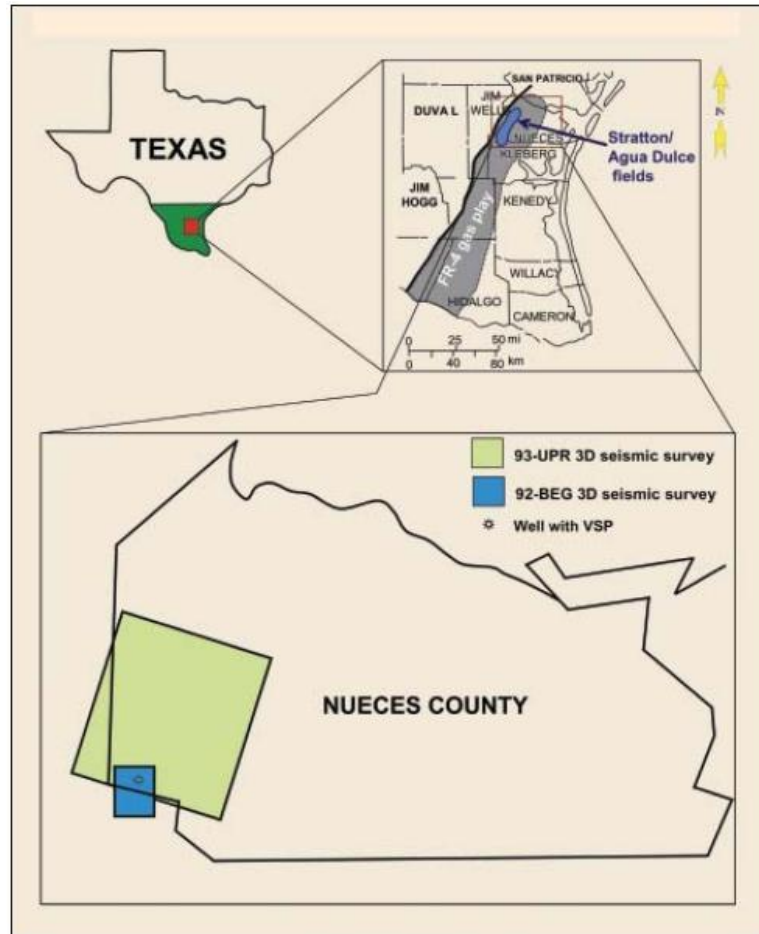


**Figure 1.** Index maps showing the location of the Stratton and Agua Dulce Fields, the Union Pacific Resources and the Bureau of Economic Geology seismic surveys, and the well in which the VSP survey was run. Modified from El-Mowafy, and Marfurt (2008)

The target for their study was the basal part of the middle Frio Formation (BMF) and they focused in three main analyses: major and subsidiary faults, structural framework, and the nature of the growth faults. With these three analyses a new structural model was proposed. We showed this model in (Figure 2).

In order to understand the nomenclature used through the entire work we show the studied interval in Figure 3 identifying E41 horizon to F44 horizon between 1.55 and 1.67 s. The horizons of interest are F11 at 1.58 s and F39 at 1.65 s. A Vertical Seismic Profile (VSP) was used to tie the seismic with the reservoir units. To understand the major and subsidiary faults they analyzed Figure 4a and identified a change in thickness of the interval between E41 horizon and the marker for the top lower of the Frio horizon in both the hanging-wall and the footwall sides of Agua Dulce (AD) fault. The change in thickness of the BMF interval in the hanging-wall at different locations relative to the AD Fault indicates that, the fault had significant control over the thickness variation of the BMF.

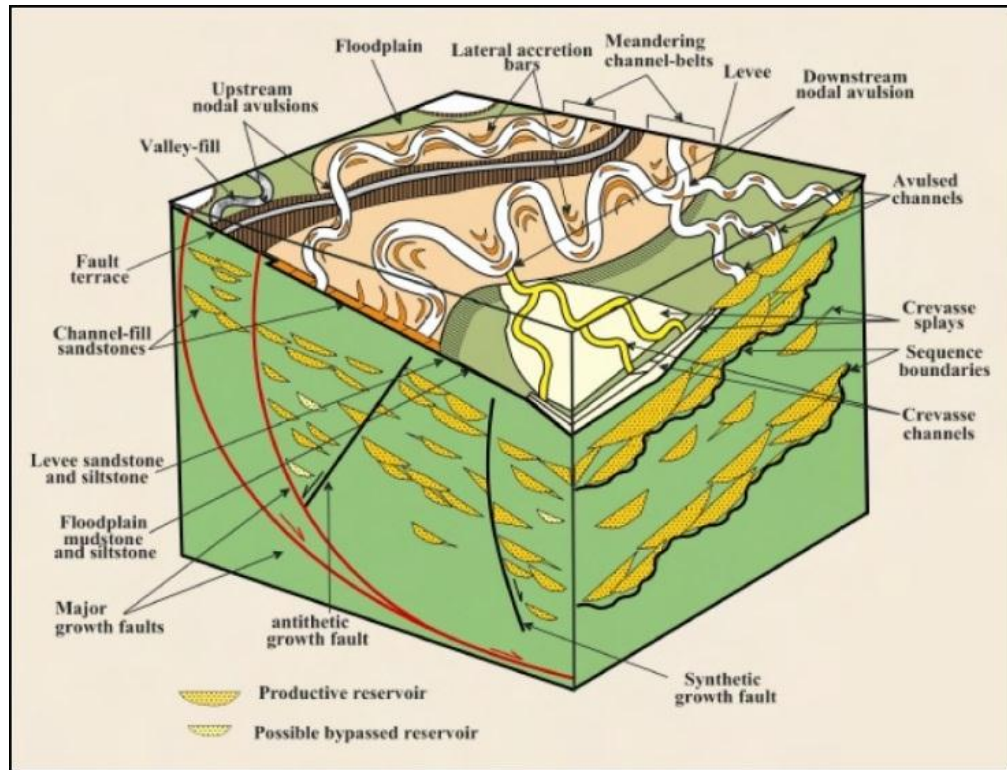
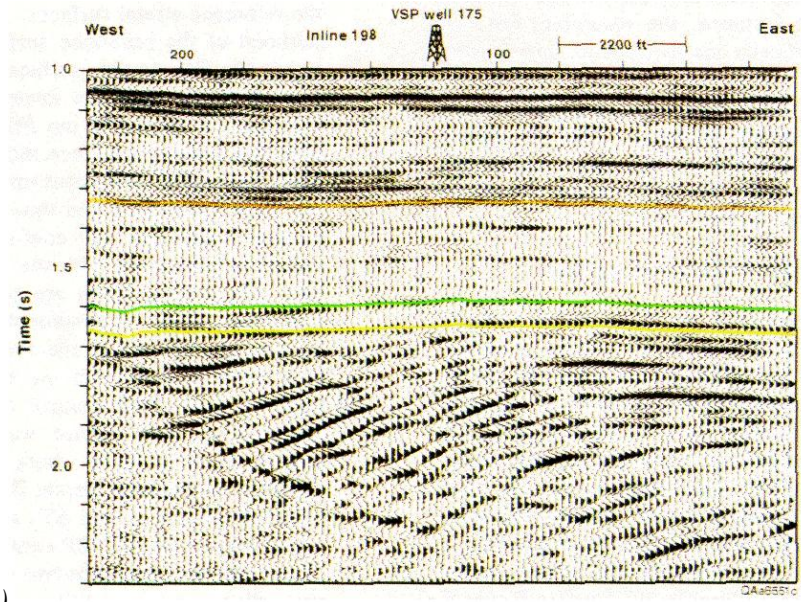
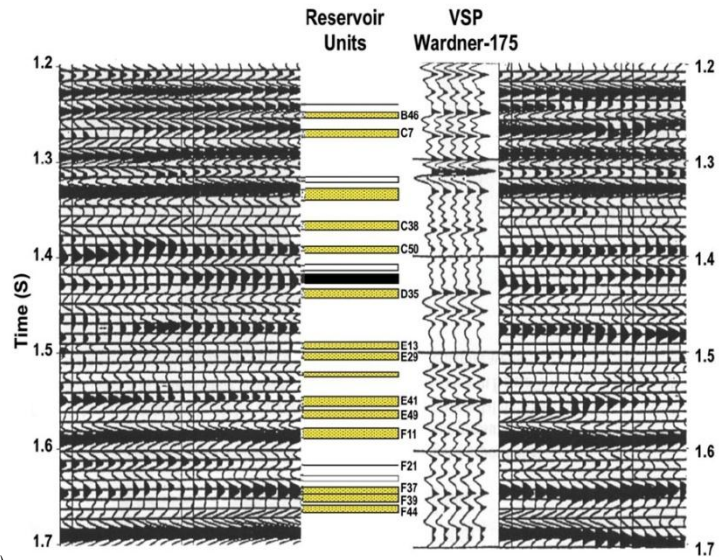


**Figure 2.** Schematic 3-D reconstruction of the fluvial facies architecture interpreted for the BMF sequence, Stratton and Agua Dulce fields, south Texas. From El-Mowafy, and Marfurt (2006)



a)



b)

**Figure 3.** (a) Vertical slice from the migrated 3-D data crossing the VSP control well showing two continuous Frio reflection events (b) SP data from well Wardner 175 showing different reservoirs in Stratton Field. Modified from Hardage et al. (1994)

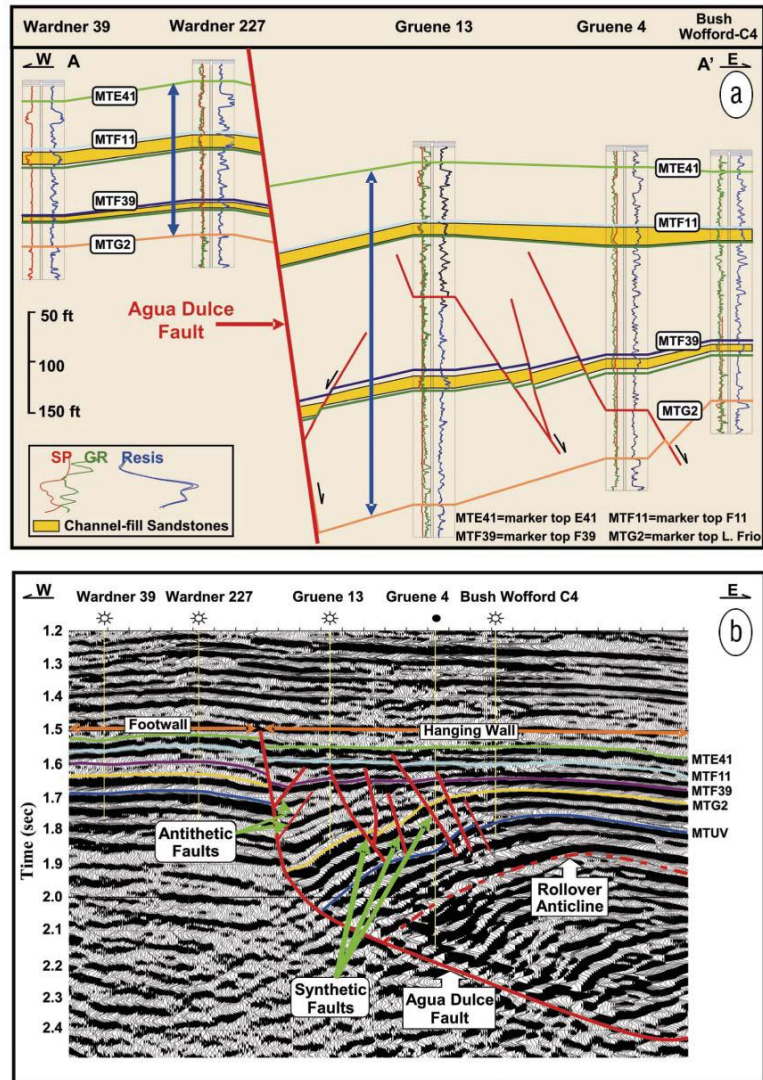


**Figure 4.** Geologic cross-section showing the disparity in thickness of the BMF interval (MTE41-MTG2) on both sides of the AD Fault. The hanging wall is deformed by the rollover anticline and a set of synthetic and antithetic faults. (b) Coincident seismic line from the UPR 3D survey showing the AD listric normal fault and the associated structures. Displacement on the AD growth fault occurs during sedimentation, resulting in equivalent beds being thicker in the hanging-wall block than in the footwall block. El-Mowafy and Marfurt (2008)

To test whether the synthetic and antithetic faults associated with the major growth faults (AD Fault) were active during deposition they constructed two geologic models and concluded that the synthetic and antithetic faults associated with the growths

fault are syndepositional (means that sedimentation was occurring at the same time as faulting) that cut through the BMF interval between G2 and F11.

Analyzing the structural framework they noticed that a contour map built for F11 horizon using only Stratton Field survey from BEG showed the major growth fault AD Fault and the subtle synthetic and antithetic faults were not recognized. Once they added the UPR 3D they identified two major faults bounding to the western side of the area and several subtle faults not shown in Stratton Field (Figure 5). Since our study was performed only using 92-BEG 3D from Stratton Field, we will not be able to show the two major faults and it will be limited to the Agua Dulce (AD) Fault.

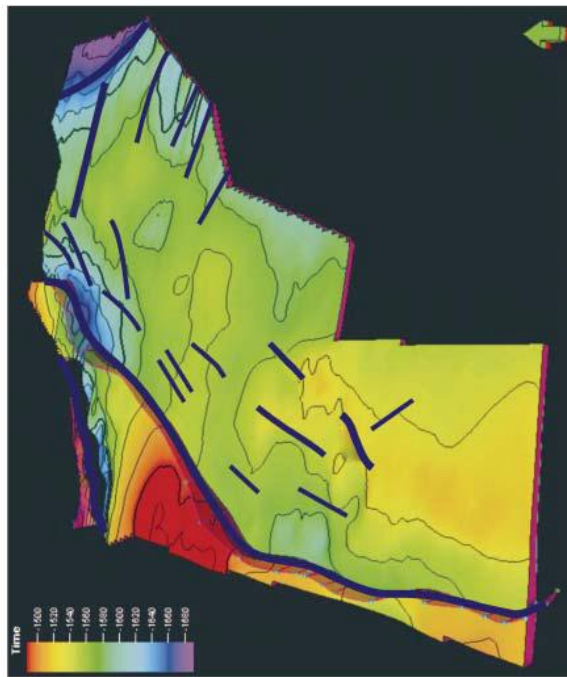


**Figure 5.** Time structure map constructed on top of the F11 horizon from the BEG and the UPR 3D surveys. Fault polygons indicate the locations of the major faults and several secondary faults. These secondary faults were not shown before at the F11 stratigraphic level. Modified from El-Mowafy and Marfurt (2008)

To understand the nature of the growth fault they analyzed several vertical lines from both surveys, but UPR 3D is the one that shows both growth faults Vicksburg (V) and Agua Dulce (AD). Figure 6a, from UPR 3D, shows that the BMF interval is deformed by the subsidiary faults on the hanging-wall side of the AD fault and accommodated mainly by synthetic faults. It is evident that the closer to the AD fault, the greater the deformation.

It can be noticed that a group of five secondary faults affects the stratigraphic units of the BMF interval (F39-F11) with the deeper horizons being more deformed than the shallower horizons. Using vertical seismic sections and well logs, they measured the vertical displacements of the major and subsidiary growth faults.

It was found that the throw of major and minor faults varies from line to line, increasing in the northern part of UPR 3D survey (Agua Dulce Field). The throw depth ranges from 850 ft (259 m) to 1600 ft (487.7 m) for the growth faults and from 15 ft (4.6 m) to 145 ft (44 m) for the synthetic and antithetic faults. These subtle faults could generate multiple reservoir compartments within the middle Frio Formation.

Since the scope of this work is to analyze geophysical methods, we will not add more details in the geological setting. We encourage the reader to follow up the geological description in Galloway, Hobday, and Magara (1982) and El-Mowafy, and

Marfurt (2008) in order to have better understanding of the structural and stratigraphic framework and the details of each reservoir unit.

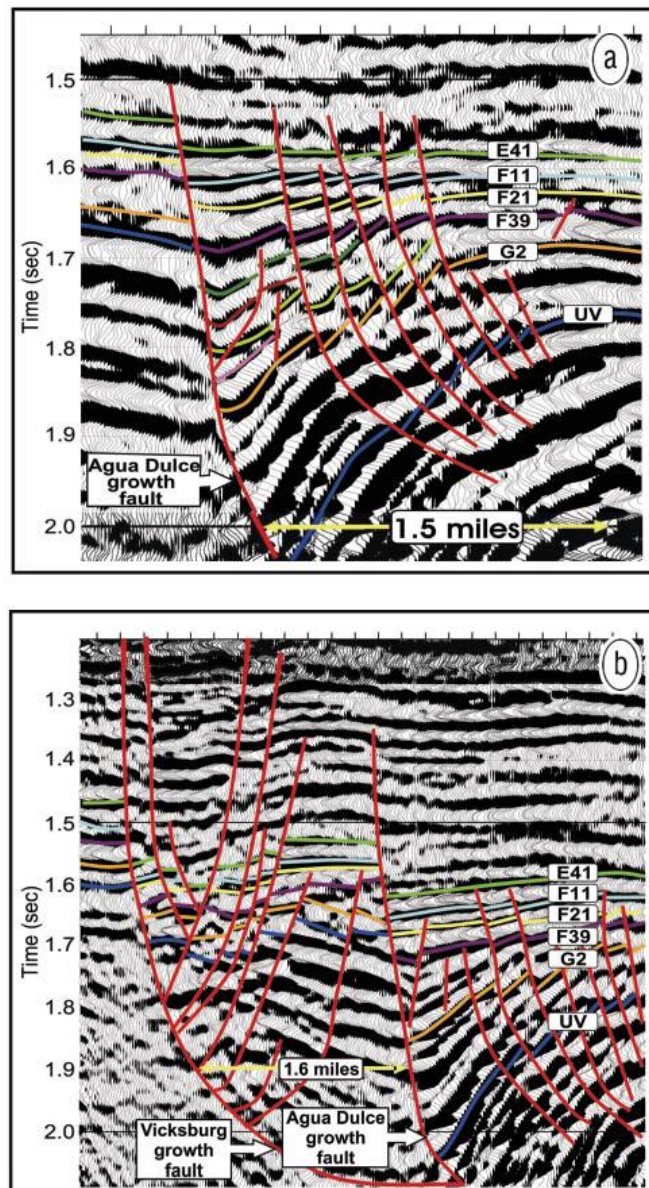


**Figure 6.** (a) Seismic crossline from the UPR 3D survey showing the deformation on the hanging-wall side of the AD fault. All subsidiary faults are affecting the deeper middle Frio (G2-F11). (b) Another seismic crossline from the same survey showing deformation in the footwall block of the AD fault. Modified El-Mowafy and Marfurt (2008)

### 1.3. Data Description

According to Hardage et al. (1994), the 7.6 sq mi (19.7 km<sup>2</sup>) area 3-D seismic data, acquired in 1992 by the Texas Bureau of Economic Geology (BEG), was recorded in four overlapping swaths. Each swath consisted of six east-west receiver lines with 1320 ft (402 m) spacing. The source lines were oriented north-south with 880 ft (268 m) spacing. The source lines were straight and uniformly spaced because bulldozers could be used to clear lanes through the mesquite-covered property. Due to permitting restrictions the northern part shows irregular paths along existing roads (Base map shown in Figure A4 from the Seismic Processing Report).

This survey has been the subject of dozens of geophysics and geology papers and counts with a large number of wells, some of those 40 years old, but we only had access to 21 wells as shown in Figure 7. Almost all the wells include SP logs and resistivity logs, some of them include density logs but none of them presents sonic logs.

In addition to the well logs, vertical seismic profile (VSP) data was recorded in two closely spaced wells inside the triangle shown in Figure 8. The VSP was used in Hardage et al. (1994) to build the thin-bed depth-to-time calibration that helps to relate the stratigraphic column with the seismic (Figure 3). This saved few steps in our interpretation.

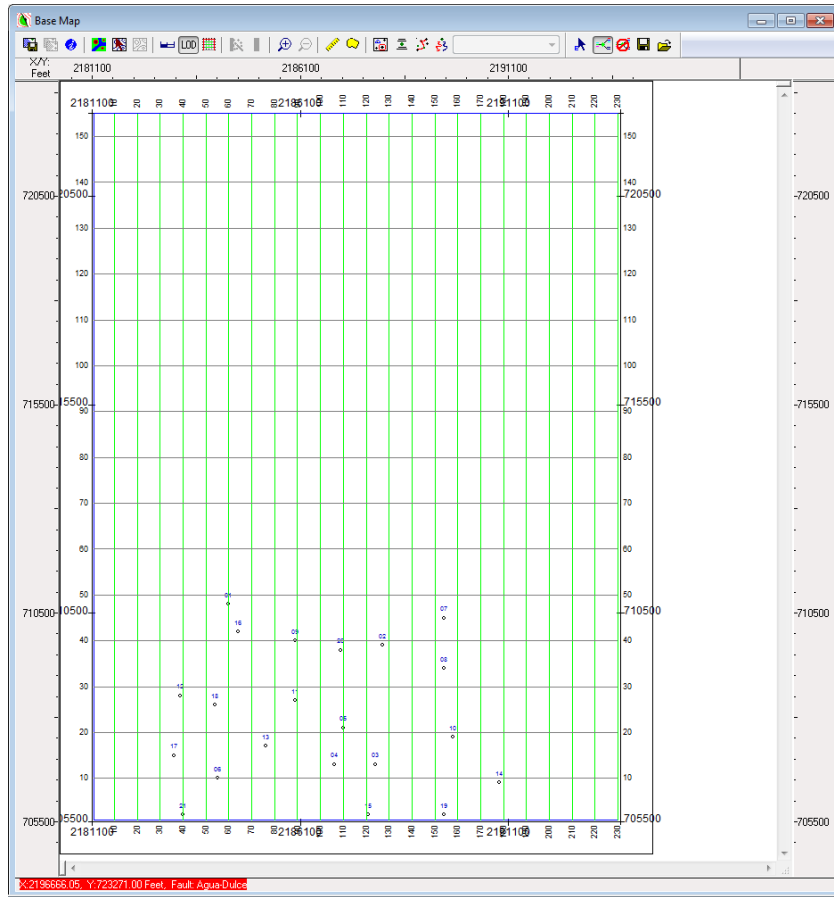


**Figure 7.** Base Map showing the 21 available wells

A full seismic processing report is shown in Chapter 3, where the details of the acquisition design and processing sequence are presented. The intention of the processing report is to serve as guideline for future work with this dataset. Also the same processing report was included in the USB drive that contains the a full standard delivery donated to the University of Houston, Department of Earth and Atmospheric Science and the Bureau of Economic Geology (BEG).

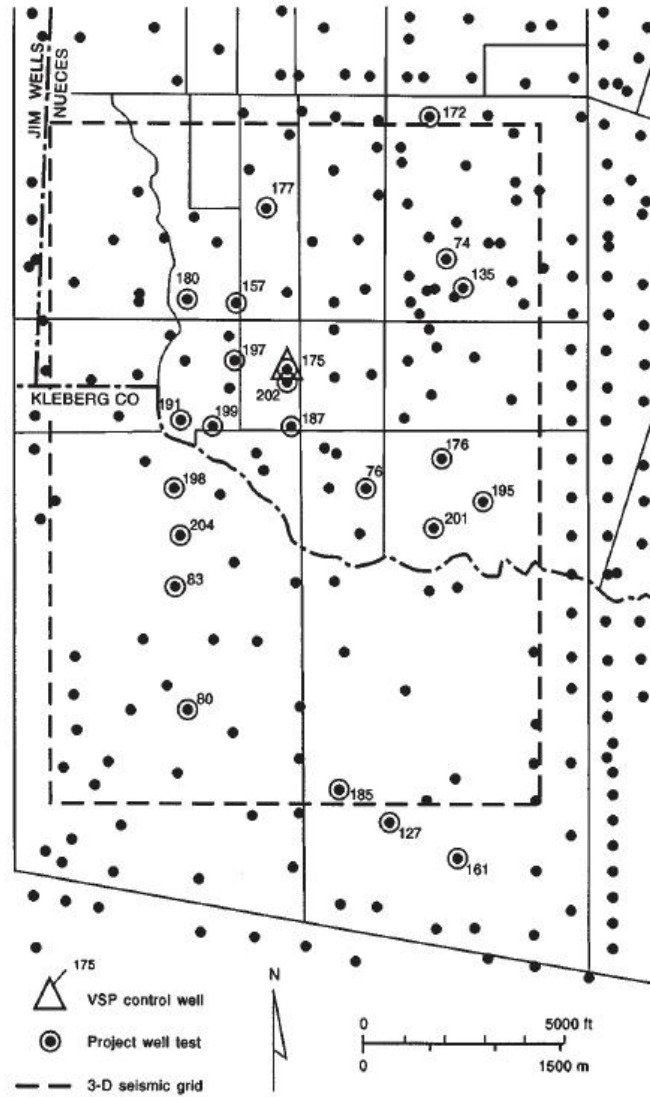


*Figure 8. Map showing wells and VSP locations. Modified from Hardage et al. (1994)*

## 1.4. Objectives

The focus of this study is to analyze and discuss the use of Diffraction Imaging technology to create an additional volume of high resolution discontinuities that could represent small faults, pinch-outs or salt flanks in 92-BEG 3D dataset from Stratton Field, South Texas.

Since we will start our work from field RAW data, all the way up to Diffraction Imaging (DI), and passing through Pre-stack Time Migration (PSTM) and pre-stack depth migration, we will be able to evaluate the definition and positioning of the faults at each step.

We will also compare the results obtained from Diffraction Imaging with conventional Similarity volume generated in ProMAX/SeisSpace in order to analyze and discuss the weaknesses and strengths of each method.

Based on the theoretical definition of the diffractions we expect to obtain a super-resolution volume of unconformities, that will show more details and bypassed faults that were not evident in the conventional seismic, and as a consequence in the similarity volume.

Since Stratton Field is well-known for the thin-bed and extremely faulted geology that creates compartmented reservoirs and the dozens of geophysical and geological papers, plus high density well control we will be able to determine the accuracy of the Diffraction Imaging technology and relate it with thin shale layers.

With the oil & gas industry focused on shale plays (unconventionals) and constantly looking for new technology that could help to understand shale reservoirs it is evident the need for research and development in that direction.

In consequence, our ultimate goal for this study will be to propose a small scale fractures identification technique in depth for shale plays, where the visualization of the natural fracture distribution and orientation is extremely important and could reduce drilling, fracking and production costs. This new volume combined with the PSTM and the PSDM structural volumes should explain the geology with more detail and accuracy.

## CHAPTER 2: THEORY AND IMPLEMENTATION

### 2.1. Prestack Depth Migration

According to Etgen, Gray and Zhang (2009), migration has three purposes: to estimate migration velocity, to produce a structural image, and to render an image whose amplitudes or other attributes give an interpreter clues about rock and fluid properties.

Two major types of prestack depth migration can be identified:

#### 2.1.1. Ray-based methods

2.1.1.1. Kirchhoff Migration

2.1.1.2. Beam Migration

#### 2.1.2. Wave-equation methods

2.1.2.1. One-way Migration

2.1.2.2. Two-way Migration (Reverse Time Migration)

Since rays represent an asymptotic solution to the wave equation, we could assume that wave-equation methods are more accurate than ray-based methods, but this statement will depend on the particular application. If the wave-equation method imaged a particular feature better than ray-based migration, then we can say that wave-equation method would be better than the ray-based method. One example of this particular

situation is observed when the ray-based method is better than the one-way wave-equation method in the imaging of dips beyond 90 degrees (overturned beds).

In this particular study the ray-based beam migration, one-way wave-equation and two-way wave-equation (Reverse Time Migration) methods will not be covered. The scope of the work is limited to understand Kirchhoff migration and the modification for Diffraction Imaging.

### Description of the Migration Methods

2.1.1. Ray-based methods: Either traces are migrated separately or an entire gather can be migrated at once to obtain the image.

2.1.1.1. Kirchhoff Migration: it is the most familiar of the ray-based methods. Its formulation is an approximate integral solution to the wave equation (Schneider, 1978). The common-shot Kirchhoff migration expression is given by:

$$I(x; x_s) = \int dx_r \int dt W \frac{\partial p_u(x_r; x_s; t)}{\partial t} \delta[t - (t_s + t_r)] \quad (1)$$

where

$x$  = image location       $x_s$  = source location

$x_r$  = receiver location       $W$  = weight function

$t_s$  = traveltime from the source to the image location

$t_r$  = traveltime from the receiver to the image location

$p_u = \text{recorded wavefield}$

$\delta = \text{Dirac delta function}$

2.1.1.2. Beam Migration: it is a directional Kirchhoff migration performed on spatial windows of the recorded data. It has potential advantages over the Kirchhoff migration, because it can overcome a major limitation that consists in the restriction to single-value travel times.

2.1.2. Wave-equation-based methods: downward-continuation of the entire wavefield followed by imaging.

2.1.2.1. One-way migration: this method applies Green's identity to the recorded wavefield in order to express the wavefield at a particular depth using a known wavefield at shallower or greater depth. The downward continuation from the recording surface is illustrated in Figure 9.

To start the one-way wave-equation migration, the source wavefield  $D$  and the recorded wavefield  $U$  are downward-continued from the surface into the earth using:

$$\left[ \frac{\partial}{\partial z} + i \frac{\omega}{V} \sqrt{1 + \frac{V^2}{\omega^2} \left( \frac{\partial^2}{\partial x^2} + \frac{\partial^2}{\partial y^2} \right)} \right] U = 0 \quad (2)$$

$$\left[ \frac{\partial}{\partial z} + i \frac{\omega}{V} \sqrt{1 + \frac{V^2}{\omega^2} \left( \frac{\partial^2}{\partial x^2} + \frac{\partial^2}{\partial y^2} \right)} \right] D = 0 \quad (3)$$

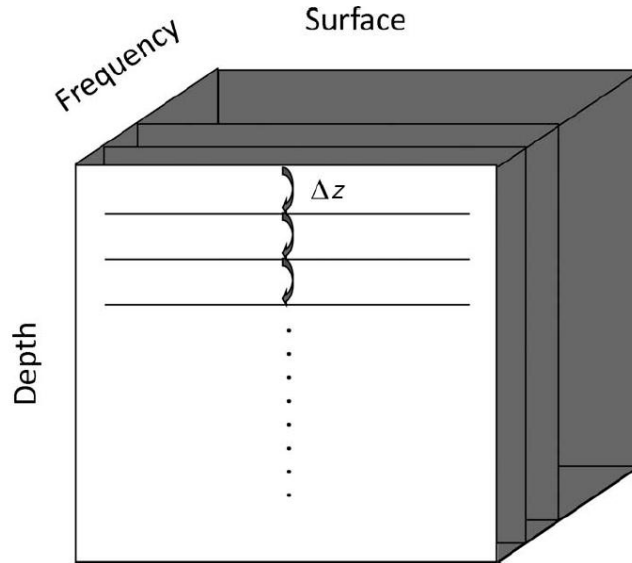


**Figure 9.** The downward-continuation operation of one-way wave-equation migration. For each frequency component, the recorded wavefield is downward-continued recursively from one depth to the next greater depth using the one-way wave equation. From Etgen, Gray, and Zhang (2009)

After this, an imaging condition has to be applied combining the wavefields and creating an image of the subsurface. Claerbout (1971) proposed two types of imaging conditions, but only the cross correlation imaging condition is going to be shown as it is often used thanks to its stability:

$$R(x) = \int U(x; \omega) D^*(x; \omega) d\omega \quad (4)$$

From the four main categories of the one-way extrapolators: Implicit finite-difference algorithms, Stabilized explicit extrapolation methods,

Phase-shift propagation with multireference velocities, and Dual-space (x-k) methods, only the last one is going to be used for this study due to software limitations.

The Dual-space (x,k) methods approximate the square-root operator by using separable functions in the space and wavenumber domains. In this category the split-step Fourier (SSF) migration (Stoffa et al., 1990), and generalized-screen methods (Le Rousseau and de Hoop, 2001) are included, the second one being the base of the software is going to be used for this particular study.

2.1.2.2. Two-way migration (Reverse Time Migration): it propagates the recorded wavefield from the recording surface into the earth using full wave equation with time running backwards.

$$\left( \frac{1}{V^2} \frac{\partial^2}{\partial t^2} - \frac{\partial^2}{\partial x^2} - \frac{\partial^2}{\partial y^2} - \frac{\partial^2}{\partial z^2} \right) p(x;t) = 0 \quad (5)$$

Unlike Kirchhoff and Beam migration there is no high frequency assumptions and unlike one-way wave-equation migration there are no approximations to the wave equation that limit the propagation angle or the ability to handle strong lateral velocity variations. It propagates waves

in all possible directions, and its ability to image dips up to  $180^\circ$  gives it an advantage over the other methods.

A comparison of the different methods of prestack depth migration is shown in Figure 10, highlighting the superior solution of the two-way wave-equation (Reverse Time Migration) method over the others three.

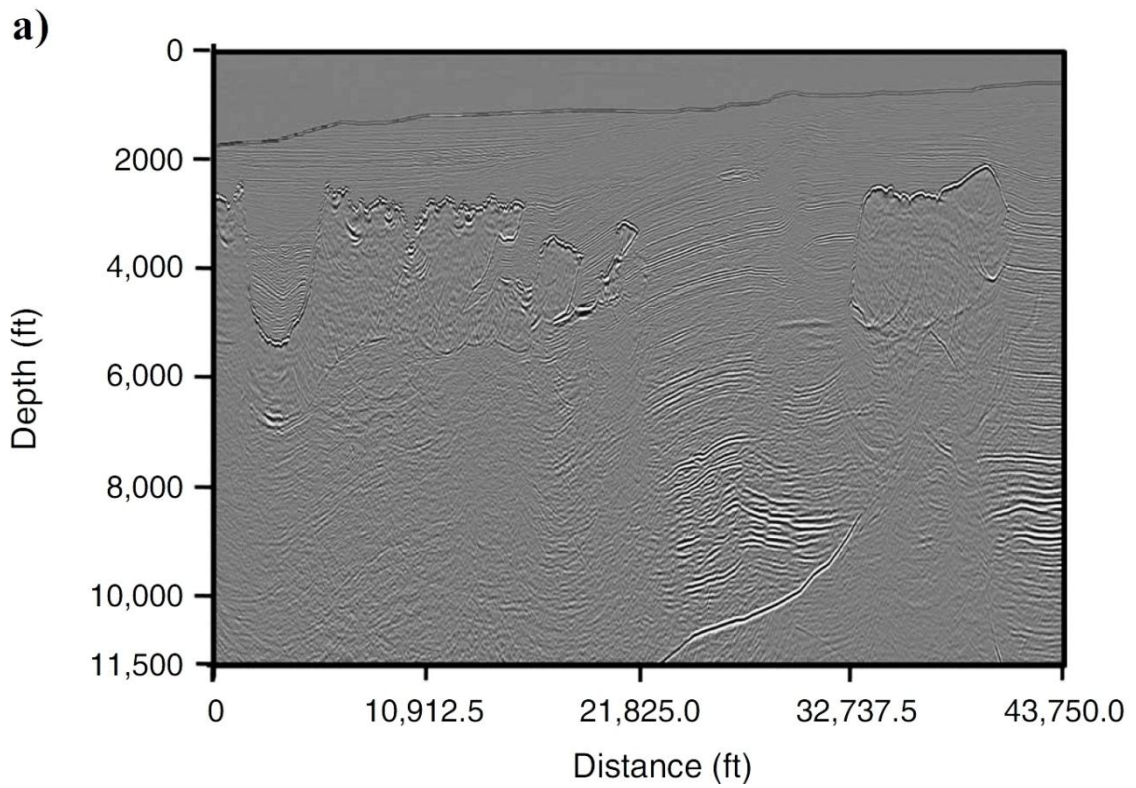


**Figure 10.** (a) Kirchhoff Migration. Modified from Etgen, Gray, and Zhang (2009)

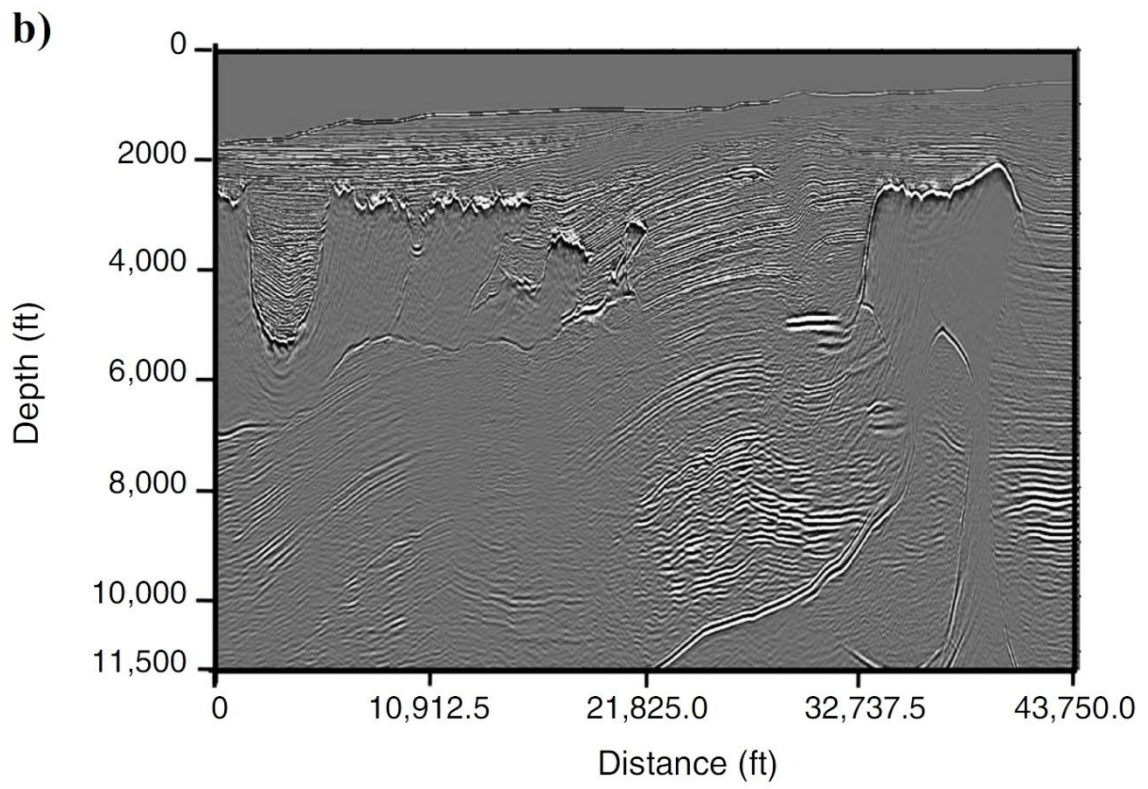


*Figure 10. (b) Beam Migration. Modified from Etgen, Gray, and Zhang (2009)*

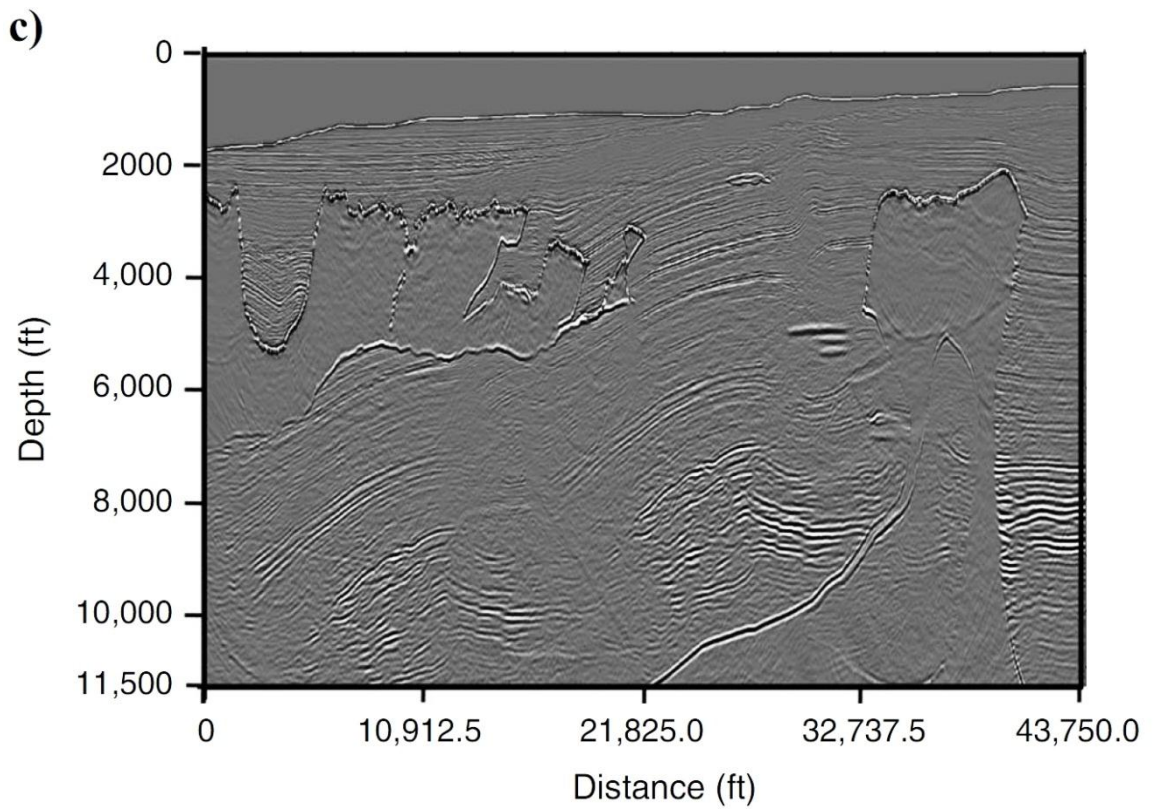


**Figure 10.** (c) *One-way Wave-Equation Migration. Modified from Etgen, Gray, and Zhang (2009)*

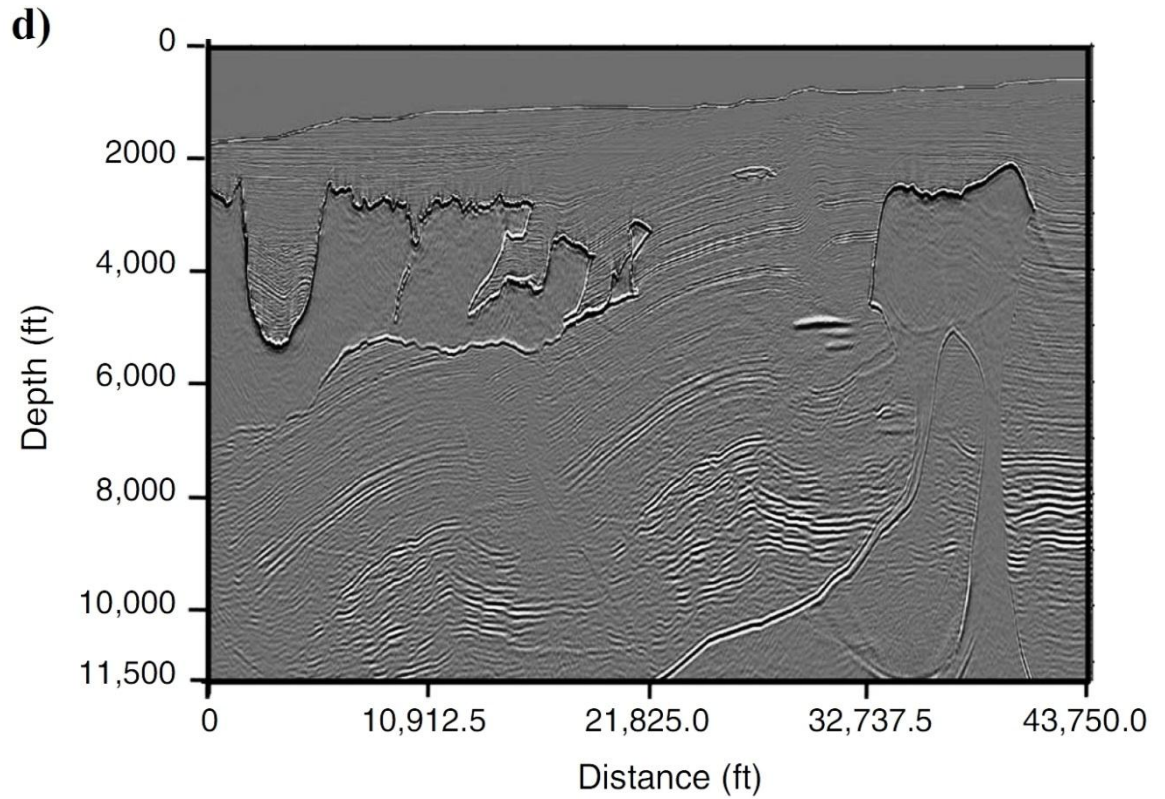


*Figure 10. (d) Two-way Wave-Equation Migration or Reverse Time Migration. Modified from Etgen, Gray, and Zhang (2009)*

## 2.2. Diffraction Imaging

### 2.2.1. Definitions

In order to understand what Diffraction Imaging is, the definition of reflection and diffraction has to be introduced and understood. According to Khaidukov, Landa and Moser (2004) and following the conditions of ray theory (Červený, 2001), **reflection** is defined as the seismic response from a sufficiently smooth interface where the

wavelength is small compared to the radius of curvature of the boundary. Therefore, **diffraction** is defined as the seismic response from a strongly curved interface, where its radius becomes of the order of the wavelength itself, and the ray theory is no longer valid.

There is not a sharp distinction between reflections and diffractions, because the ray-theory criteria are only qualitative.

### 2.2.2. Geometrical Aspects

Reflections and diffractions can be separated based on some geometrical aspects explained in this section. According to Khaidukov, Landa and Moser (2004) and as a rule of thumb, reflections and diffractions from a discontinuity at the same depth differ in moveout and the position of the travetime apex in the shot gather. Figure 11a to 11c shows three examples of reflections for a horizontal plane, a strongly curved plane and a dipping plane. It is evident that the travetime apex changes with the location of the source and the receiver.

On the other hand Figure 11d is an example of a point diffractor, where the travetime apex remains just above the point, independently of the position of the source and the receiver. If the source moves to a next location, the diffraction hyperbola does not move laterally, but only vertically. As a consequence, diffractions can be found anywhere in the shot gather.

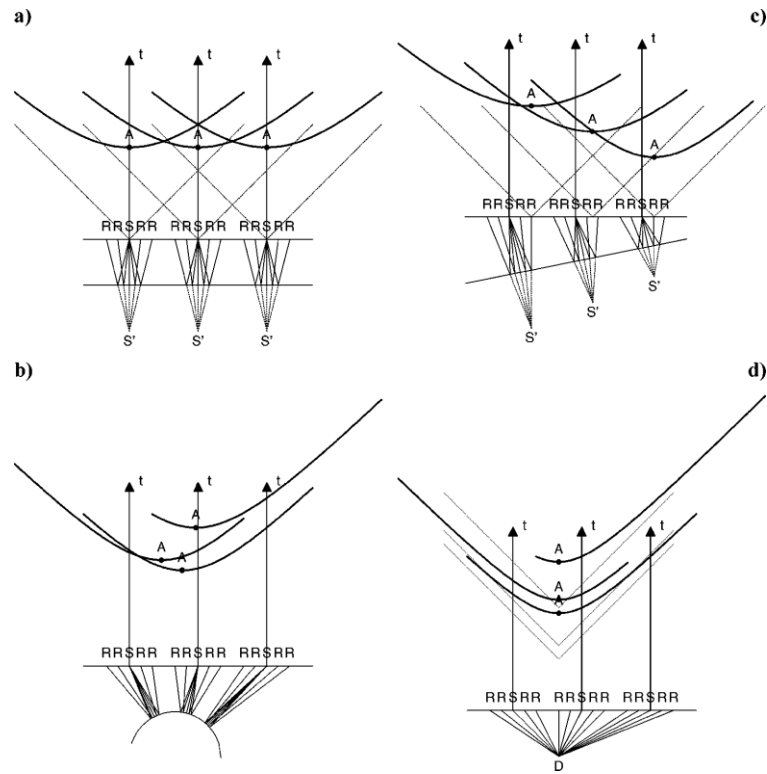


**Figure 11.** Geometry of reflection and diffraction. *S, R* denote source and receiver locations, respectively; *S'* the imaginary reflection source; *A* the reflection/diffraction hyperbola apex; and *t* the travelttime. (a) Reflections on a horizontal plane reflector. (b) Reflections on a strongly curved reflector. (c) Reflections on a dipping reflector. (d) Diffractions on a point diffractor (denoted by *D*). Khaidukov et al. (2004)

For a simple horizontal reflector model with a point diffractor at the same depth, the diffraction curves have a steeper dips and exist over a more narrow range of offsets in the shot gather than the reflection curves. For more complex models with non-hyperbolic moveout it doesn't exactly apply, but it helps to qualitatively separate reflection from diffraction.

Since the travelttime apex of diffractions is laterally invariant, a multisource acquisition could be used as an advantage. One shot gather can show the diffraction too

close to the reflection, make it very difficult to separate them, but if moved to a different source, the apex of the diffraction remains just above the point diffractor, creating a separation from the reflection.

### 2.2.3. Diffractions and Super-resolution

In this chapter a new concept will be introduced, **Super-resolution**. Since the Diffraction Imaging goal is to extract high resolution fracture patterns, the concept of super-resolution will help to understand why higher resolution than conventional seismic is observed.

According to Khaidukov et al. (2004) the Rayleigh criterion of resolution explains that no details smaller than half the wavelength (quarter of a wavelength for a two-way time) are recoverable for a band-limited data. Below this limit, the uncertainty grows for location, dip and curvature of discontinuities. The interpreter's eyes become a double-edged sword. Migration artifact generally creates apparent edges that could mislead the interpreter to identify structural details that are not real. This becomes an advantage of diffraction images, since it doesn't suffer from apparent edges caused by migration artifacts.

Super-resolution is defined by Khaidukov et al. (2004) as the recovery of sub-wavelength scale details in a seismic image. The diffractive component of the full

wavefield is identified as a carrier of super-resolution information coming from scatterers of sub-wavelength scale.

It is clear that recovering the information carried by diffractions could be very useful for interpretation, but the separation between reflections and diffraction could be difficult as presented in the previous section. Moreover, many of the conventional processing steps in time processing as normal moveout (NMO), velocity analysis and stack are biased towards reflection events, attenuating diffraction events. Figure 12 shows the difference in moveout for reflections and diffractions. It is evident that once the CDP gather is stack the non-flat events will cancel each other losing the diffraction events. The next step in Diffraction Imaging research will include the analysis of each of those steps in the processing sequence and how those affect the final result.

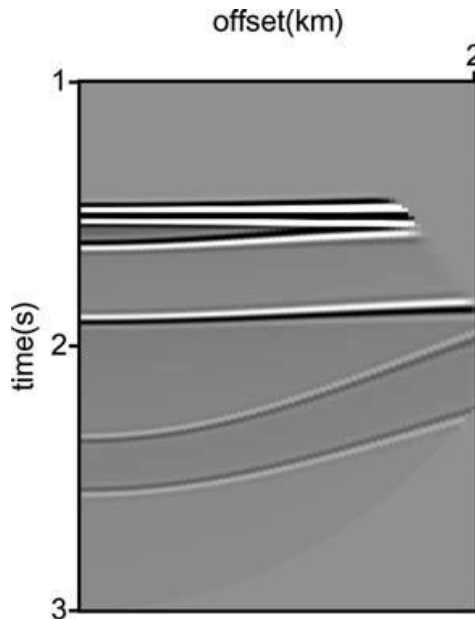


**Figure 12.** Common data point gather, after NMO correction with constant velocity. Modified Moser and Howard (2008)

## 2.2.4. Theory and Method

The diffraction imaging techniques can be divided in two categories:

- a) The first one separates the input seismic data in two parts, one containing the wave energy from the reflections and the other containing the wave energy from the diffractions. After the separation, each component is used to provide an image using traditional imaging methods.
- b) The second one does not separate the input data. It uses an imaging technique proposed by Moser and Howard (2008), that suppresses reflecting surfaces in the image expressed as a reflection suppressing kernel for Kirchhoff migration.

Starting with the conventional Kirchhoff migration expression:

$$V_{Kirch}(x) = \sum_{s,r} \int U(t, s, r) \delta[t - t_d(s, x, r)] dt \quad (6)$$

where

$V_{Kirch}(x)$  = seismic image

$U(t, s, r)$  = seismic data

$(s, r)$  = source and receiver pairs

$t_d(s, x, r)$  = travelttime source – image – receiver

$\delta$  = Dirac delta function

The traveltimes function can be expressed as:

$$t_d(s, x, r) = T(s, x) + T(x, r) \quad (7)$$

where the  $T(s, x)$  represents the traveltime from the source to the image location and  $T(x, r)$  the traveltime from the image location to the receiver. The idea behind Diffraction Imaging is to modify the equation (6) with a weight function  $w(s, x, r)$ , that is biased towards diffractions. The modified Kirchhoff diffraction imaging is given by:

$$V_{diff}(x) = \sum_{s,r} \int w(s, x, r) U(t, s, r) \delta[t - t_d(s, x, r)] dt \quad (8)$$

where  $w(s, x, r)$ , is capable of attenuating the reflections. The process is divided in two steps. The first one is to get the image using the conventional Kirchhoff equation (6). Once the structural image is available the second step is analyzing the structures in the Kirchhoff image and determines the normal vector  $n$  to these structures at each image point. This is probably the most difficult part of Diffraction Imaging. The analysis of the structures is done using plane wave destruction (PWD) filter technique. The technique was

introduced by Claerbout (1992) and improved by Fomel (2002). The weight function can be expressed as:

$$w(s, x, r) = 1 - \frac{\hat{n} \cdot (p^s + p^r)}{\|p^s + p^r\|} \quad (9)$$

where the functions  $p$  represents the gradient of the traveltimes from source to image location (10) and from the image location to the receiver (11) given by:

$$p^s(x) = \nabla_x T(s, x) \quad (10)$$

$$p^r(x) = \nabla_x T(x, r) \quad (11)$$

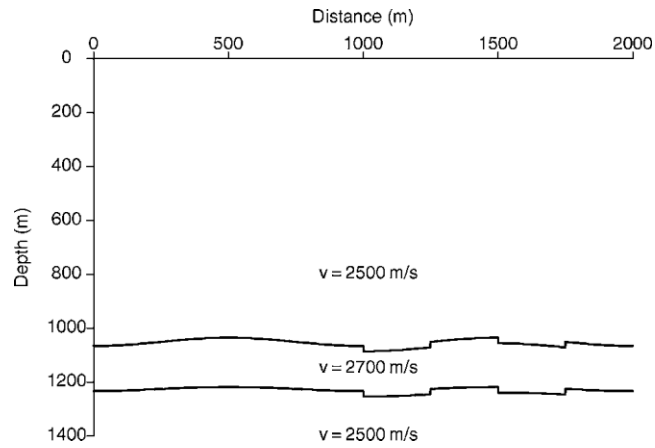
$$\frac{(p^s + p^r)}{\|p^s + p^r\|} \quad (12)$$

The normal vector described in equation (12) is the angle bisector of the wave vectors for the incoming and outgoing waves. The weight function will be approximately zero for a reflector, since the direction of the bisector is co-linear with the normal vector. For diffractions will not be zero for most of the wave propagation directions, because the seismic waves propagate in all directions. The available algorithm in ZTK has a gain function in order to moderate the filter for angles close to zero and 90 degrees.

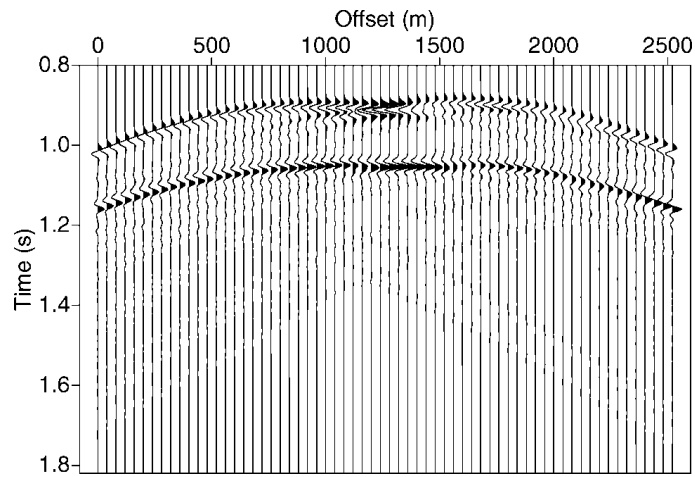
### 2.2.5. Application

In the previous sections the theory behind Diffraction Imaging technique was introduced and explained. Since the objective of this work is to find a useful tool to identify small discontinuities in order to reduce fracking and drilling costs, several examples on synthetic and real data are going to be presented, showing the added value of this technique.

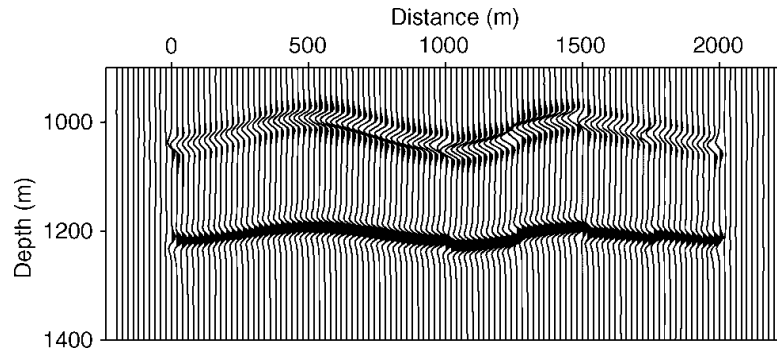
Figure 13 show a three layer model separated by faulted interfaces. Each layer has a constant velocity of 2500, 2700 and 2500 m/s. The faults displacement is 20 m and the wave-field has frequencies up to 60 Hz, therefore the displacement is under resolution, based in Rayleigh limit of half wavelength (quarter of a wavelength for a two-way time). More details of the geometry of this model can be found in Khaidukov et al. (2004). Figure 14 show a shot gather and it is easy to see that the amplitude of the diffractions is several orders of magnitude weaker than the reflections. In Figure 15 the shots were full-wave depth migrated. Even the discontinuities can be inferred from the image, even more if looking at the model before seeing the image.



**Figure 13.** Two-layer model with curved and faulted interfaces. Velocities within the layers are constant and equal to 2500 m/s and 2700 m/s. The fault offset is 20 m. Khaidukov et al. (2004)



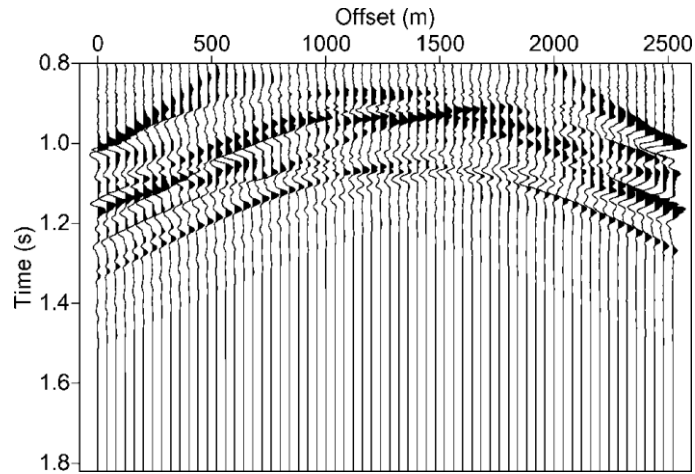
**Figure 14.** One of the shot gathers over Figure 13. Modified from Khaidukov et al. (2004)



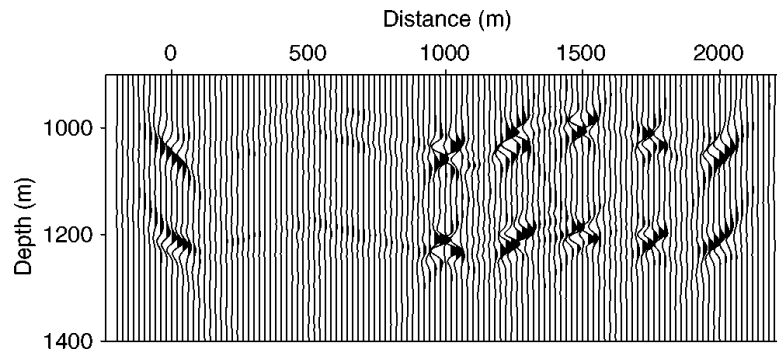
**Figure 15.** Depth migration of full-wave shot gathers. Khaidukov et al. (2004)

Figure 16 shows the same shot gather after attenuating the reflection. The diffractions are boosted automatically and start having a main role. Figure 17 show the depth migration of diffraction shot gathers. As expected, the high amplitudes are found where the discontinuities are present. The reflections were attenuated. Figure 18 show clearly the difference in fault definition between the depth migration of conventional shot gathers (Figure 18a) and the depth migration of diffraction shot gathers (Figure 18b). Around 1000m, in conventional depth migration it is observed a small change in time between traces. If no other information is available, it could be assumed that a processing artifact is causing that difference.

A problem in the velocity field or in the statics could easily create this type of difference. On the other hand, a radical change between traces is observed for the diffraction image. The discontinuities are now observed properly. This proves that the resolution obtained with Diffraction Imaging goes beyond the Rayleigh limit.



**Figure 16.** Shot gather of Figure 14 with reflections suppressed. Modified Khaidukov et al. (2004)



**Figure 17.** Depth migration of diffraction shot gathers. Fault positions as well as reflector edges are clearly visible (and easy to interpret) compared to Figure 15. Modified from Khaidukov et al. (2004)

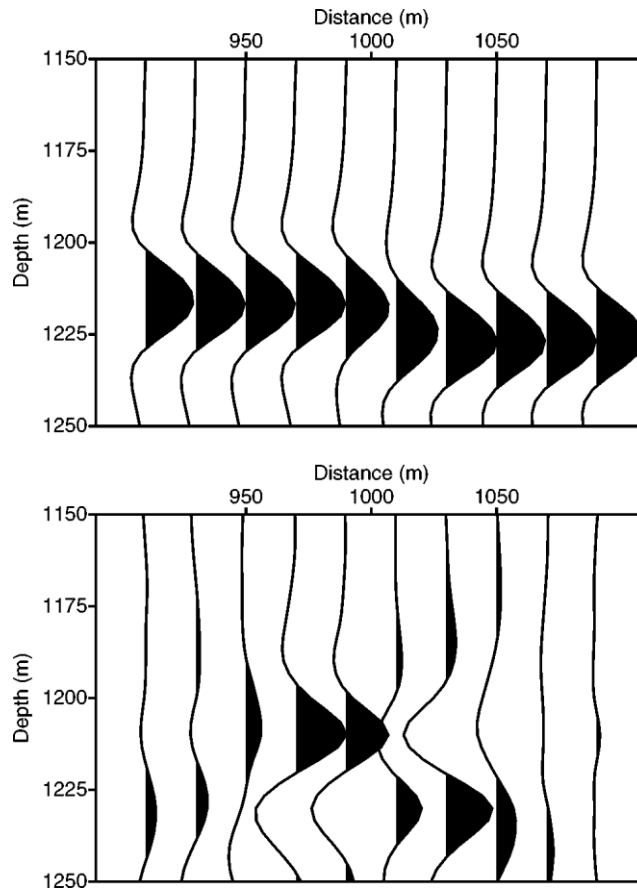


**Figure 18.** Zoom on full-wave image (top, zoom from Figure 15) and diffraction image (bottom, zoom from Figure 17) at (1000 m, 1200 m). The diffraction image allows for a much better and less ambiguous interpretation of the fault geometry than the full-wave image. Modified from Khaidukov et al. (2004)

Another synthetic example is shown in Figures 19 to 21. Figure 19 shows a synthetic velocity model with two discontinuous slides and a shot gather located above the intersection of the two slides (marked with the red arrow). The model was obtained using straight forward finite-difference. Figure 20 shows a full-wave Kirchhoff migration stack and an offset gather in the same location as the shot gather from Figure 19.

Finally in Figure 21 the Diffraction Imaging migration is shown with the corresponding gather. The difference in the amplitudes is evident. As it was expected, the Diffraction Imaging enhanced the diffraction energy and attenuated the reflection energy. The five points of discontinuity are now isolated and showed as main events. The gather shows a concentration of energy in the intersection of the two slides. The potential of Diffraction Imaging is observed in synthetic datasets and it will be supported with real data.

In the next chapter we will show the results of Diffraction Imaging technique applied to 92-BEG 3D dataset from Stratton Field located in Kleberg and Nueces counties, South Texas. The discussion of the results will help to determine whether Diffraction Imaging helps to better identify discontinuities.

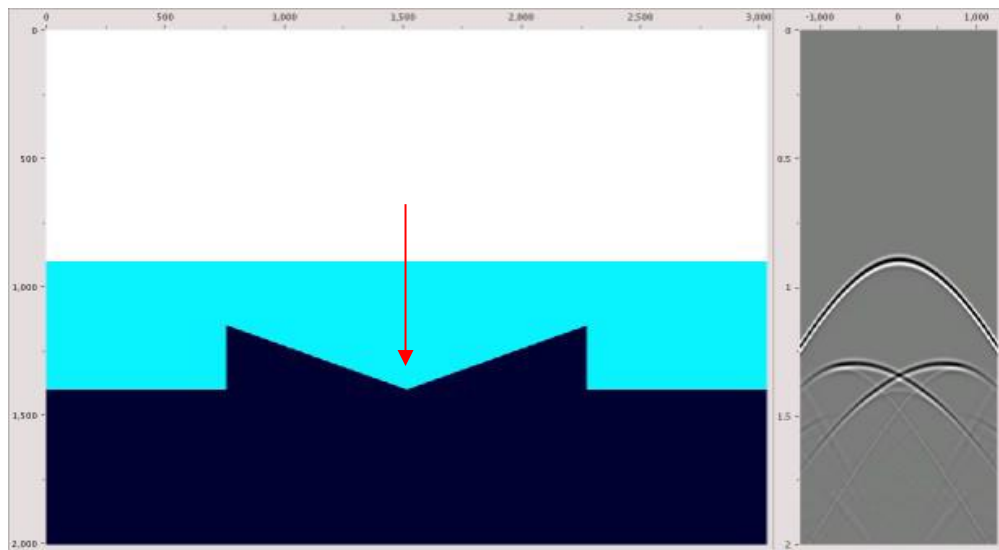


**Figure 19.** Velocity Model and Synthetic shot gather from the point above the intersection of the two slides. Modified from Sturzu et al. (2012)

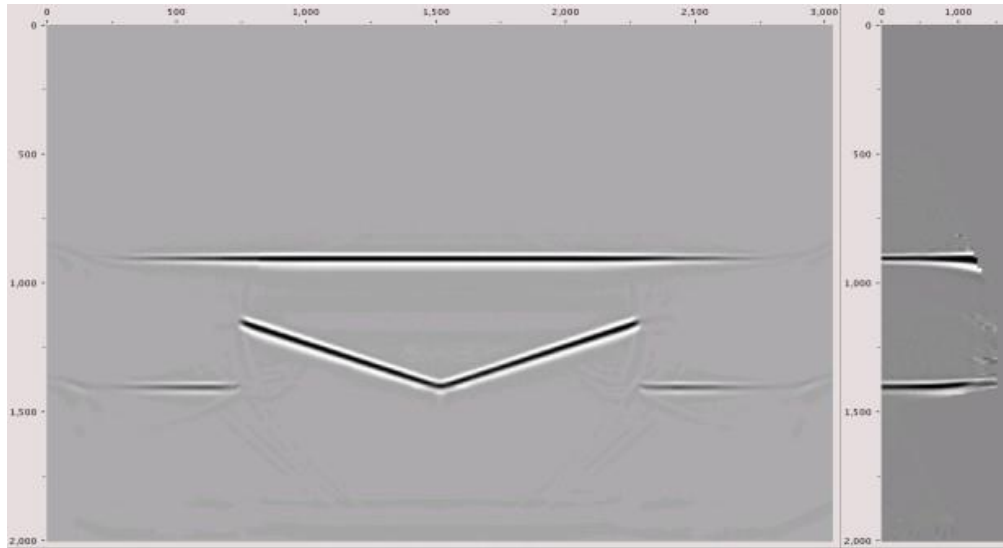


**Figure 20.** Kirchhoff migration stack using the exact velocity model and Offset gather in the location of the shot. Modified from Sturzu et al. (2012)

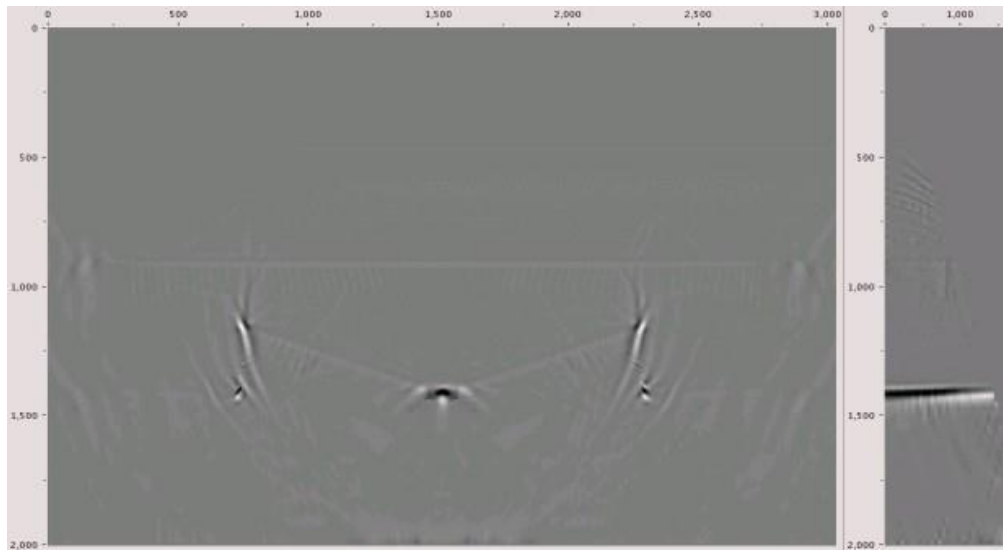


**Figure 21.** Diffraction imaging migration result and offset gather for the same location as Figure 20. Modified from Sturzu et al. (2012)

## CHAPTER 3: APPLICATION AND RESULTS

### 3.1. Methodology

#### 3.1.1. Time Processing and Interpretation

As mentioned in the previous chapter and the appendix, the 92-BEG 3D dataset from Stratton Field located in Kleberg and Nueces counties, South Texas was used. In order to control the processes applied to the dataset, a conventional time processing sequence was applied starting from field raw data without geometry.

The available software for the time processing included ProMAX/SeisSpace R5000.0.2.0, Focus 5.4 and Seismic Studio V1.6.20.0 for refraction statics. All the interpretation was done with IHS Kingdom Suite V8.7.1.

The applied conventional processing sequence can be separated in three main stages. The first stage included the **Geometry Building** which in this particular case was built from scratch following the acquisition Observer Reports; the **Preprocess** including Shot Domain Noise Attenuation, True Amplitude Recovery (TAR), Deconvolution (DECON) and Surface Consistent Amplitude Compensation (SCAC); and **Refraction Statics**.

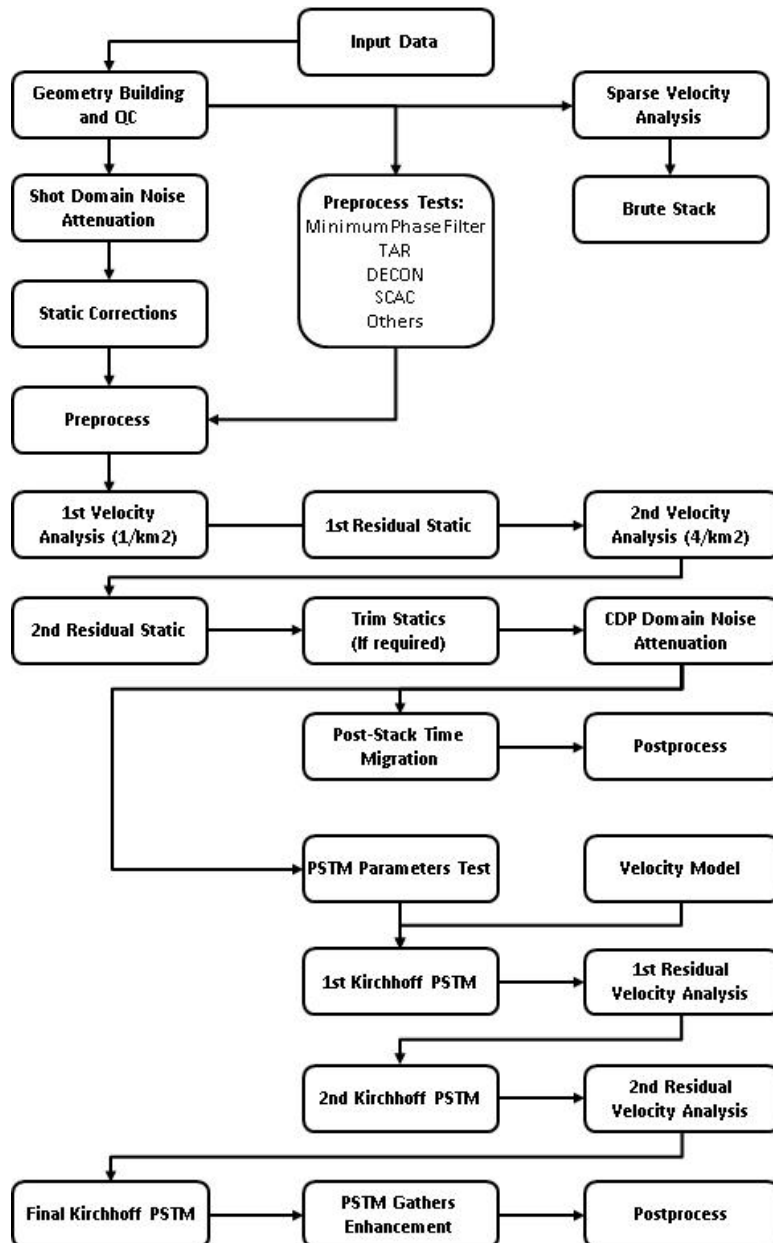
The second stage considers the **Velocity Analysis**, the first one with a 1000x1000m grid and the second one with a 500x500m grid. After each velocity analysis, automatic **Residual Statics** were applied. Once the velocity analysis and the residual statics were done **Trim Statics** were computed and applied using the best stack as a pilot. A **CDP Domain Noise Attenuation** was applied to improve the signal-to-noise ratio.

Finally a **Post-stack Time Migration** was applied after stacking the clean CDP gathers in order to have a migrated volume to compare with the PSTM results.

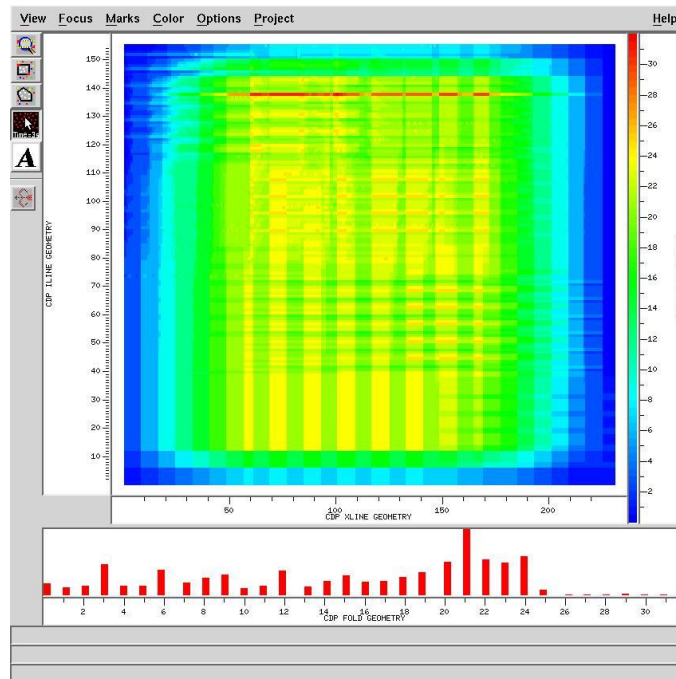
The third and last stage is the prestack migration stage. Once the parameters were selected, two runs of **Kirchhoff PSTM** were performed every 500m. After each run, Residual Velocity Analysis was performed in order to flatten the CRP Gathers. Once the best velocity model was obtained, a final Kirchhoff PSTM was run to the entire volume. After the migration, a workflow for PSTM gathers enhancement was applied.

Figure 22 shows a conceptual scheme of the Conventional Time Processing Sequence and the Appendix contains a Seismic Processing Report with the details of the processing sequence and the selected parameters. Figures 23, 24 and 25 shows the fold map with the IL and XL distribution and the PSTM stack for IL 80 and XL 110.

Once the time processing was finished, the PSTM volume RAW and with post-processing were loaded into IHS Kingdom Suite to perform a basic horizon interpretation and fault picking. Figure 26 shows IL 45 passing through WELL\_07 with the Agua Dulce fault, formation tops and horizons C38, F11, and F39.



*Figure 22. Conventional Time Processing Sequence*



*Figure 23. Fold Map with IL and XL Distribution*

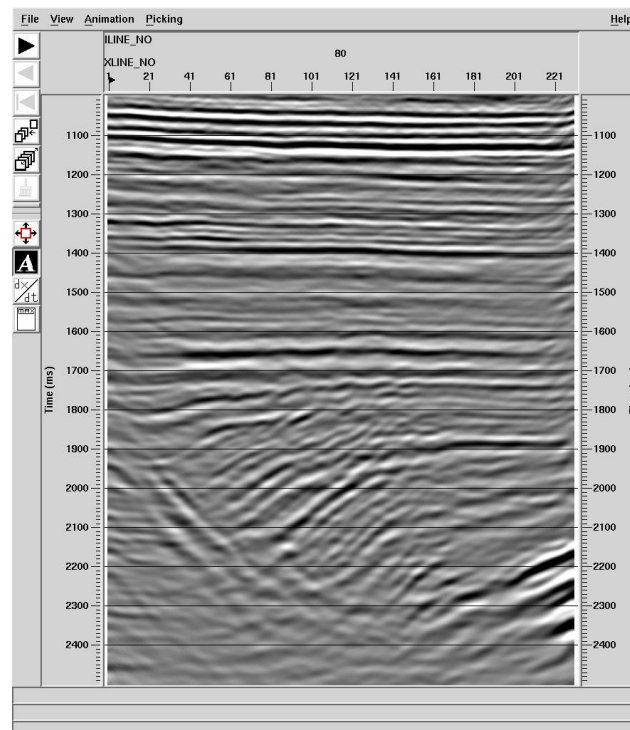


*Figure 24. PSTM Stack – IL 80*

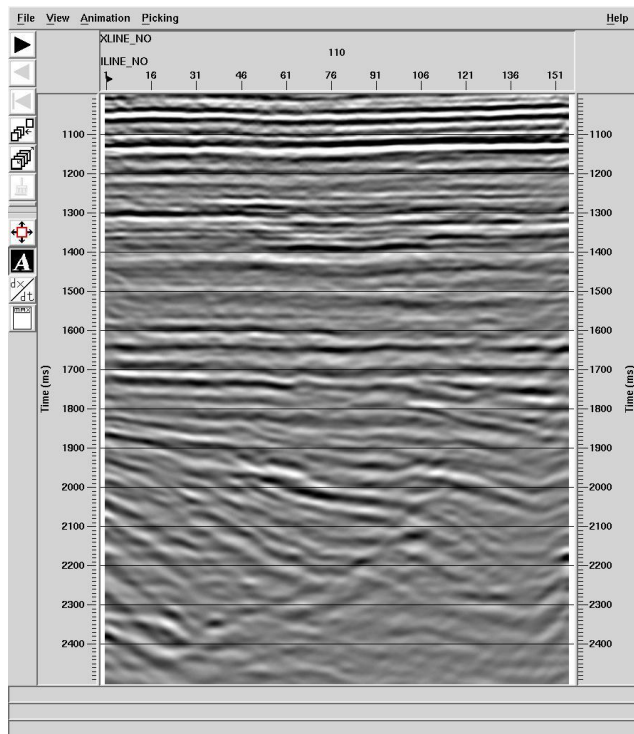


*Figure 25. PSTM Stack – XL 110*

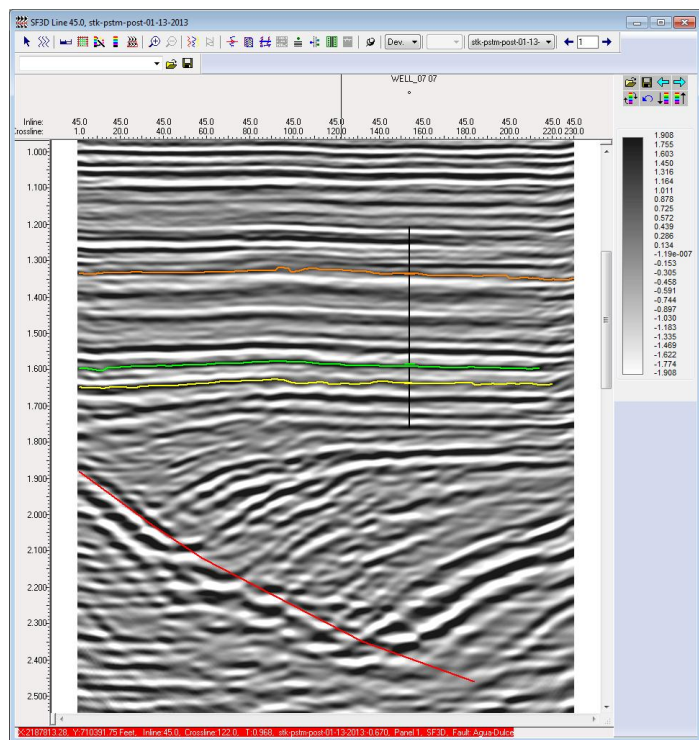


*Figure 26. PSTM Stack – IL 45 with WELL\_07 and Interpretation*

Horizons C38 (orange), F11 (green), and F39 (yellow) from Figure 26 were used to tie the seismic with the well information. Figure 3a from Hardage et al. (1994), shows the relation between the available VSP with the formations and the seismic. The Agua Dulce fault (AD) and the other minor faults (F01 to F04) were picked to analyze how were being imaged through the different stages of this work.

Figure 7 shows the base map in IHS Kingdom Suite with the well locations. From the 21 available wells only wells 7 to 21 had density log. Since none of the wells had sonic log, those had to be calculated from the resistivity logs using Faust's empirical Equation:

$$V = 2000(\delta z)^{1/6} \quad (13)$$

Where  $z$  is the measured depth in feet,  $\delta$  is the measured resistivity in ohm-m and 2000 is an empirical value. Since the velocity obtained from the previous equation is not robust, the velocity was calculated for a second time from the density logs using the inverted Gardner's Equation (15):

$$\rho = 0.23(V_p)^{0.25} \quad (14)$$

$$V_p = \left( \frac{\rho}{0.23} \right)^4 \quad (15)$$

Where  $V_p$  is the P-wave velocity in ft/s and  $\rho$  is the measured density from the density log in g/cc. The two different velocities obtained from resistivity and density logs were used to create synthetic seismograms and refine the well tie with the seismic. Figure 27 and 28 shows the synthetic seismograms in WELL\_07 created from the resistivity log and from the density log.

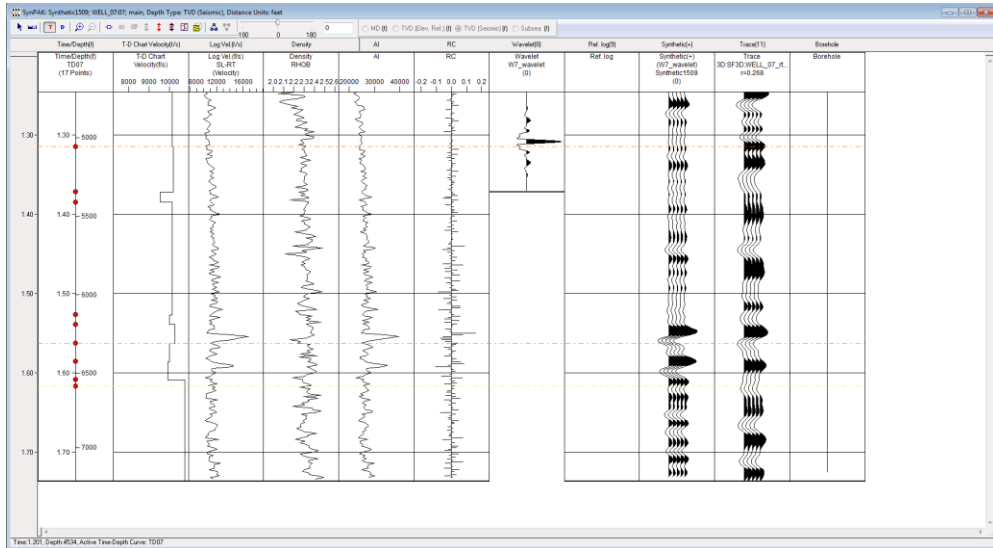


**Figure 27.** Synthetic Seismogram in WELL\_07 created with the velocity from resistivity log

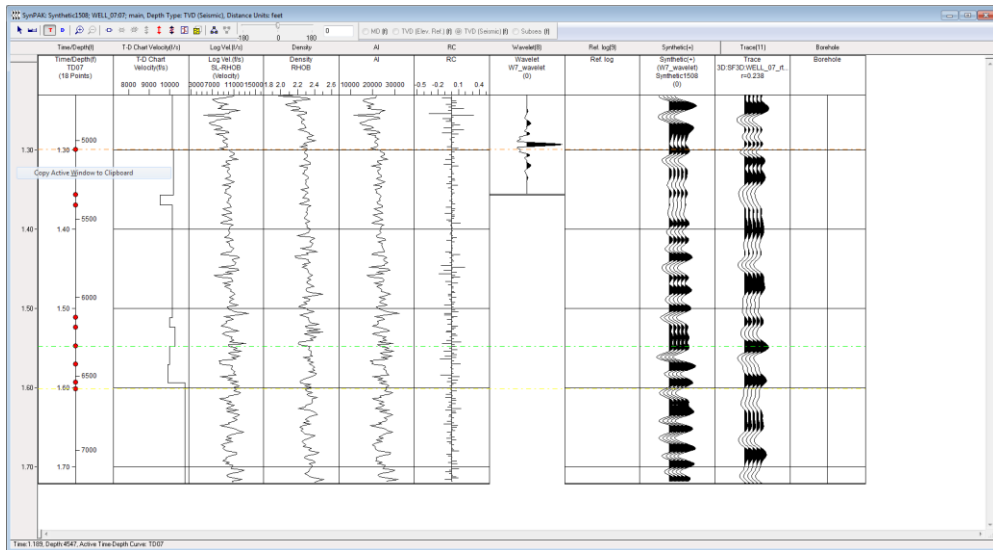


**Figure 28.** Synthetic Seismogram in WELL\_07 created with the velocity from density log

In addition to the conventional PSTM processing, an Event Similarity Prediction algorithm (ESP) was applied to enhance the discontinuities. ESP calculates the dissimilarity of each trace relative to up to eight of its neighbors. Figures 29 and 30 shows a time slice at 1800 ms of the PSTM stack and the same stack after ESP.

It is well known that the use of similarity and coherence type of attribute improves the quality of the image and has been used to identify discontinuities for a long time. The ESP will be applied to the results of the Depth Imaging and later will be compared with the results from the Diffraction Imaging.

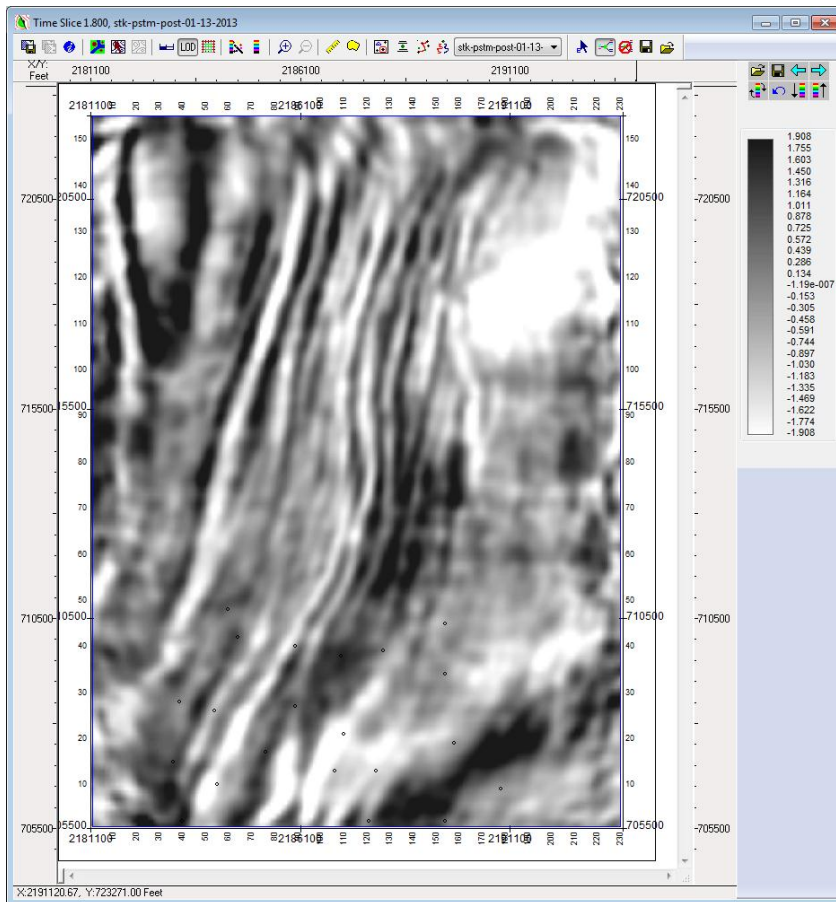


**Figure 29. PSTM Stack - Time Slice at 1800 ms**

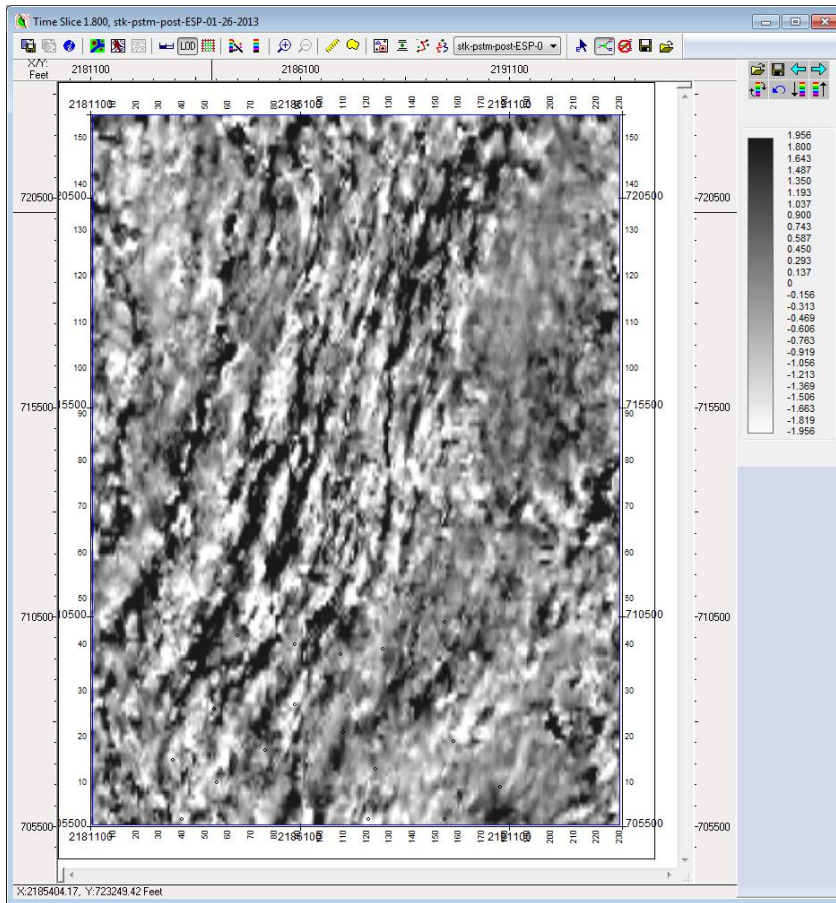


**Figure 30. PSTM Stack after ESP - Time Slice at 1800 ms**

It is expected to find differences between the comparison of the ESP applied to the depth imaging results and the diffraction imaging since the theory behind both techniques is different.

### 3.1.2. Depth Imaging and Interpretation

After finishing the time processing, a conventional Depth Imaging sequence was applied. Figure 31 shows a conceptual scheme of the processing sequence used in this

work. The entire depth imaging sequence was done using ZTK, Kirchhoff Prestack Depth Migration software from Z-Terra, Inc.

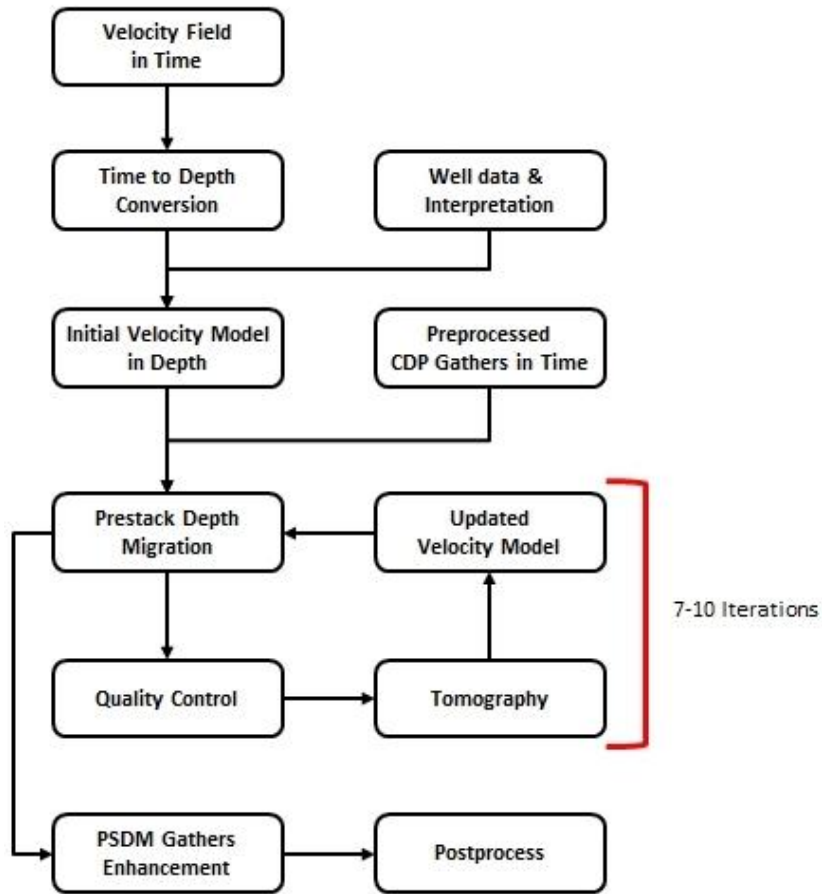


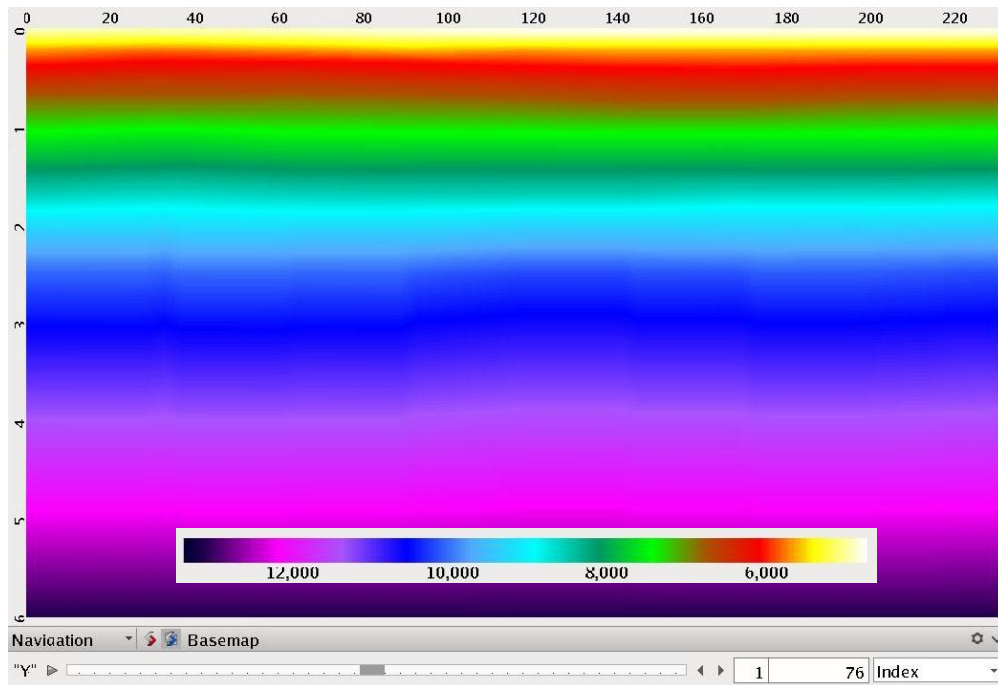
**Figure 31.** Depth Imaging Processing Sequence

Using the velocity field from the time processing, the well information, the interpretation and the available bibliography, the initial velocity model in depth was created. Since the velocity model building could represent an entire work by itself, it will not be explained in detail in this work. Figure 32 and 33 shows the initial velocity model

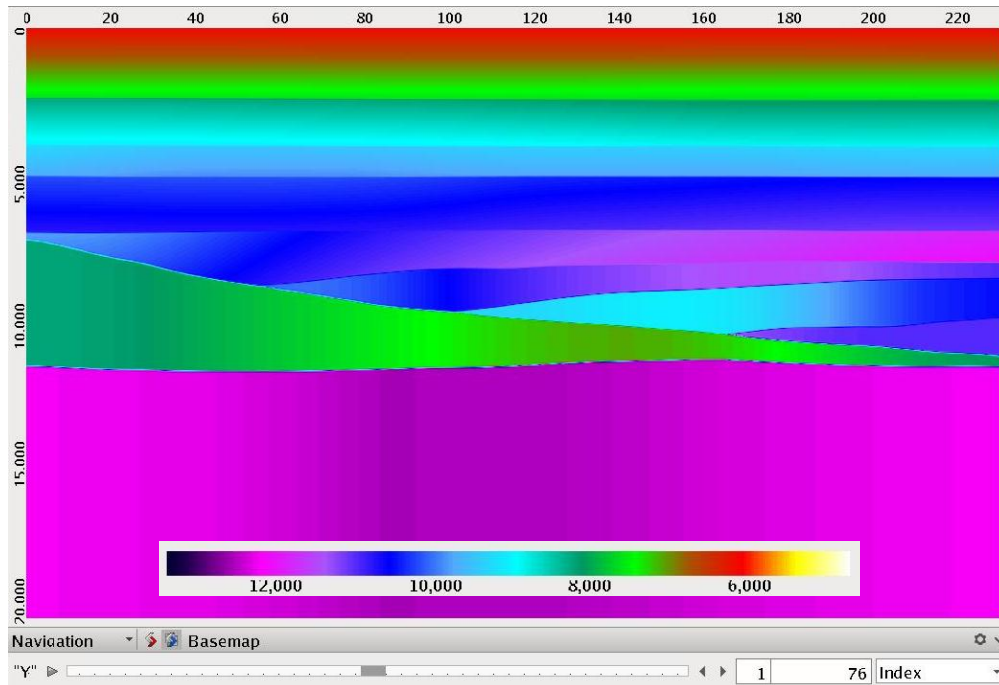
in time from the Time Processing and final velocity model in depth for IL 76. The final velocity model was obtained after 7 iterations of tomography.

The final velocity model in depth was used to run a Kirchhoff prestack Depth Migration (PSDM). The aperture parameter selection was done based on the complex geology and steep dips. A variable aperture was selected to allow up to 70 degrees in the deeper part and 20 degrees in the shallow part.

A basic post-processing sequence was applied to the PSDM stack in order to improve the signal-to-noise ratio. The stack was loaded into IHS Kingdom Suite and formations C38 (orange), F11 (green), and F39 (yellow). The Agua Dulce fault and faults F1 to F4 were interpreted again in order to compare with the time processing results.



**Figure 32.** Initial Velocity Model from the Time Processing – IL 76 (from ZTK)



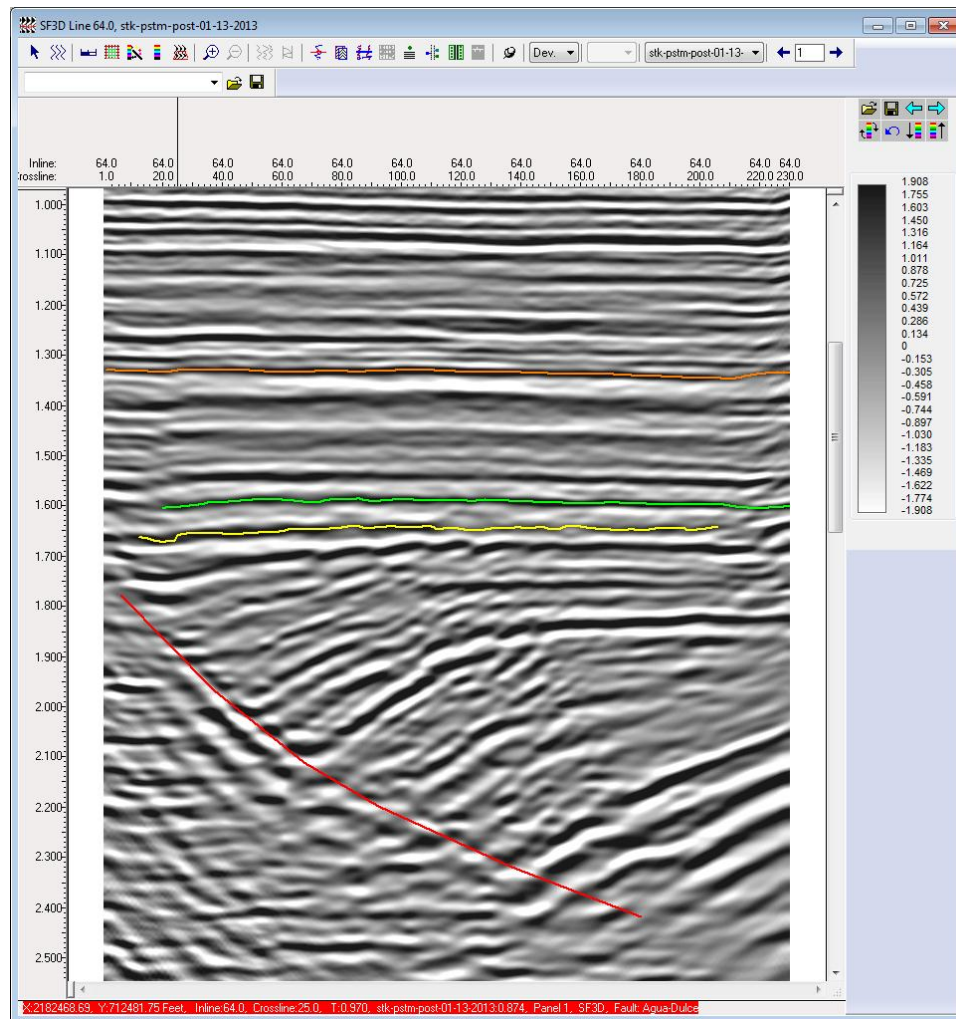
**Figure 33.** *Final Velocity Model in Depth – IL 76 (from ZTK)*

Figure 34 shows a comparison between the interpretation done in the time volume and the depth volume. It can be noticed that the definition of the faults was improved after the prestack depth migration was applied.

After performing the interpretation in depth, the same Event Similarity Algorithm (ESP) applied to the PSTM volume was applied to the PSDM volume. Figure 35 shows a comparison at 7230 ft of the PSDM stack and PSDM stack after ESP.

A quick analysis of the previous comparison shows that the details observed in the ESP volume are greater than the PSDM volume. The attribute enhances the discontinuities, improving the image and helping the interpretation of the faults. It is

expected to even improve the fault definition after Diffraction Imaging. It is important to note that the quality of the Diffraction Imaging relies in a good preprocess of the data in time and a robust velocity model in depth, that gives the best PSDM stack. For this reason, this work shows the processing procedures from field raw data, allowing the reader to follow each step and understand any possible issue.



**Figure 34.** (a) Interpretation in Time – IL 64

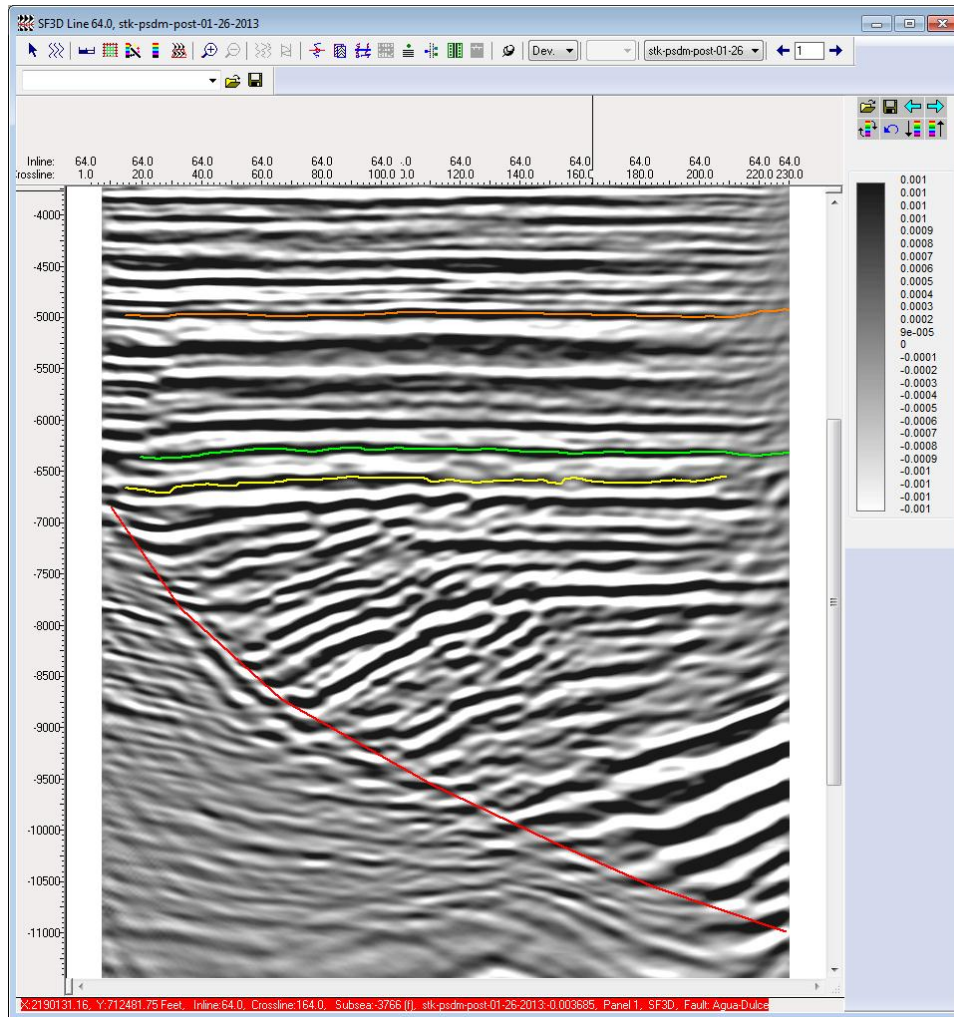


*Figure 34. (b) Interpretation done in Depth – IL 64*

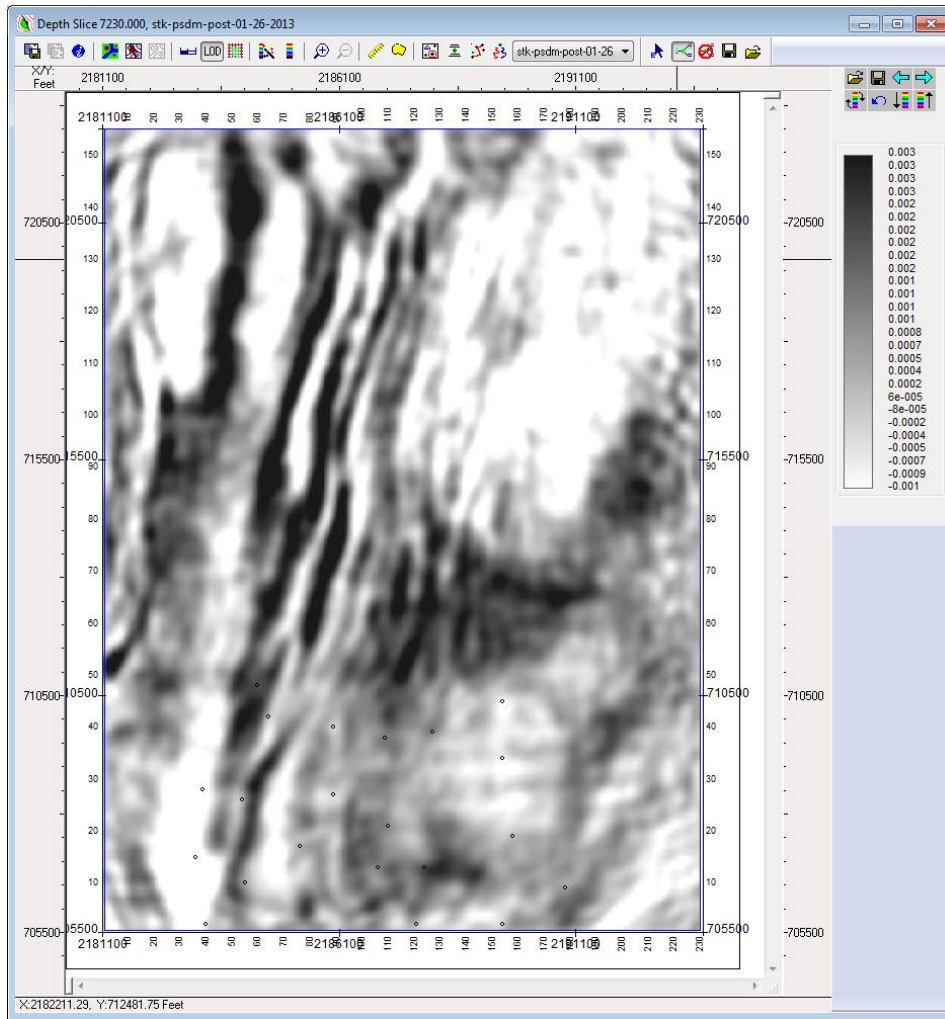


*Figure 35. (a) PSDM Stack - Depth Slice at 7230 ft*

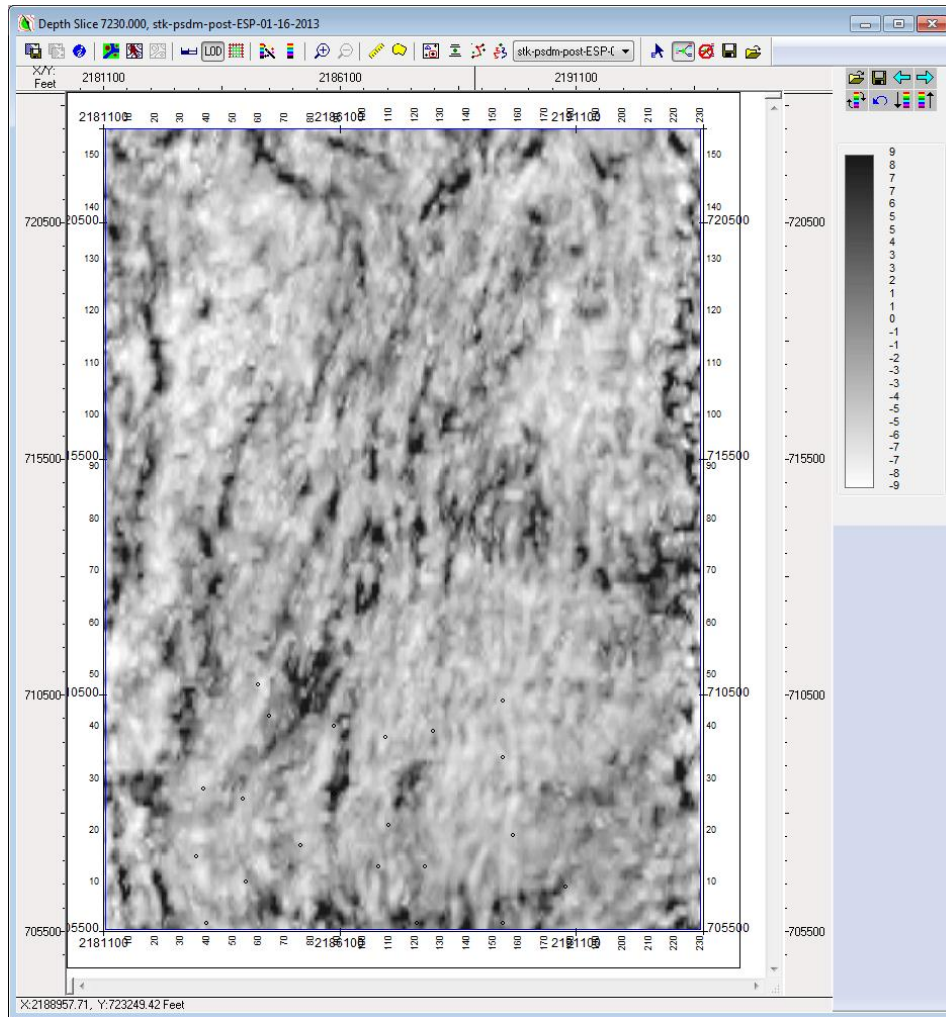


**Figure 35. (b) PSDM Stack after ESP - Depth Slice at 7230 ft**

### 3.1.3. Diffraction Imaging and Interpretation

Once the Depth Imaging (PSDM) and its interpretation was finished, the Diffraction Imaging (DI) sequence was applied. Figure 36 shows a conceptual scheme of the processing sequence used to produce the DI results. It consists in two major stages. The first one is to obtain the dips in the Inline and Xline directions from the PSDM stack

with post-processing. To achieve that, the plane wave destruction (PWD) filter technique introduced in the previous chapter was used.

The second stage takes the computed dips, the CDP Gathers in time and the best velocity model in depth and applies the modified Kirchhoff migration algorithm that attenuates the reflections and enhances the diffractions.

The migration software ZTK, from Z-Terra, Inc., obtains the diffraction image using a taper filter in the migration kernel. It computes the specularity, defined as the cosine of the angle between local reflector dip and the bisector of the ray vectors from the image point to the source and receiver, respectively.

The parameter selection was simple, since there are only two main parameters that control the results: internal specularity filter threshold and filter smoothness. The filter **threshold** is equal to the center point of the transition ( $u_0$  in Figure 37). The second one is the filter **smoothness**. It is equal to the width of the transition interval ( $du$  in Figure 37). Figure 37 shows the specularity taper function that is chosen as a piecewise cubic function of the specularity defined in three intervals. It can be noticed that if the taper is equal to 1, it preserves the diffractions and if it is equal to 0 it suppresses the reflections.

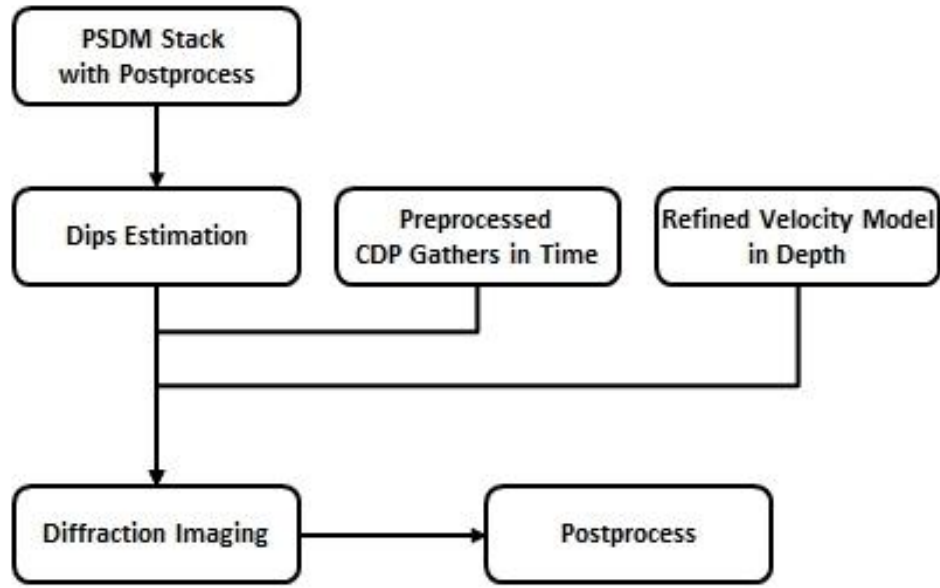


**Figure 36.** *Diffraction Imaging Processing Sequence*

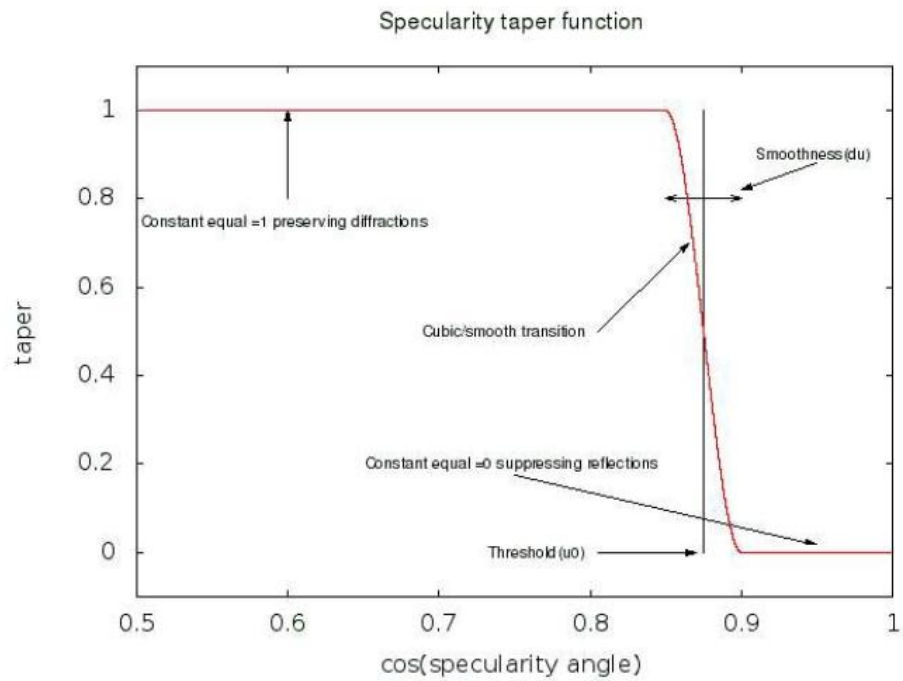


**Figure 37.** *The specularity taper Function (ZTK Manual, Sturzu, I., Popovici, A. M. and Musat, I.)*

Figure 38 shows a depth slice at 7230 ft with the results from the diffraction imaging. A mild post-processing was applied to the raw output from ZTK to improve signal-to-noise ratio. The DI volume with post-processing was loaded into IHS Kingdom Suite to do the interpretation and the comparison with the results obtained after PSTM and PSDM stages. Since DI is basically used to identify small scale discontinuities in map view, the interpretation was reviewed and analyzed mostly in map view.

The interpretation done at this stage of the work was focused on the fault definition and the analysis of the discontinuities that the DI volume shows.

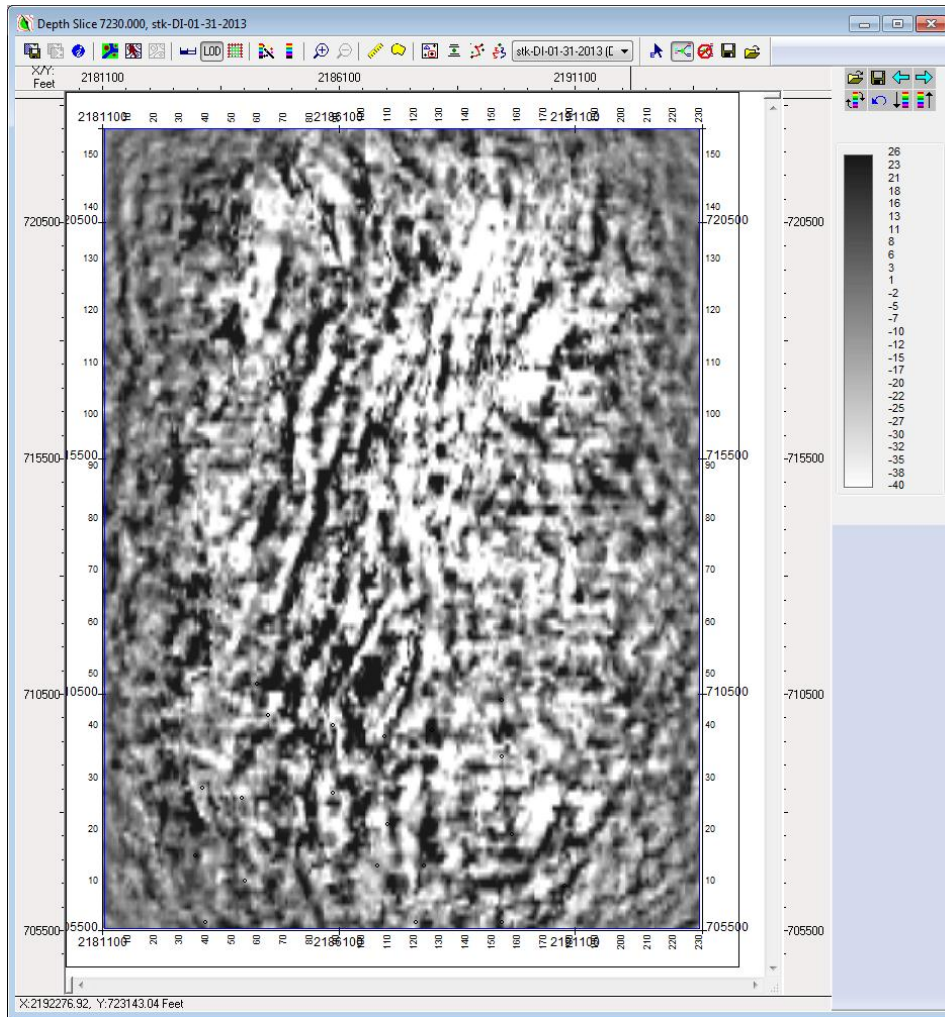
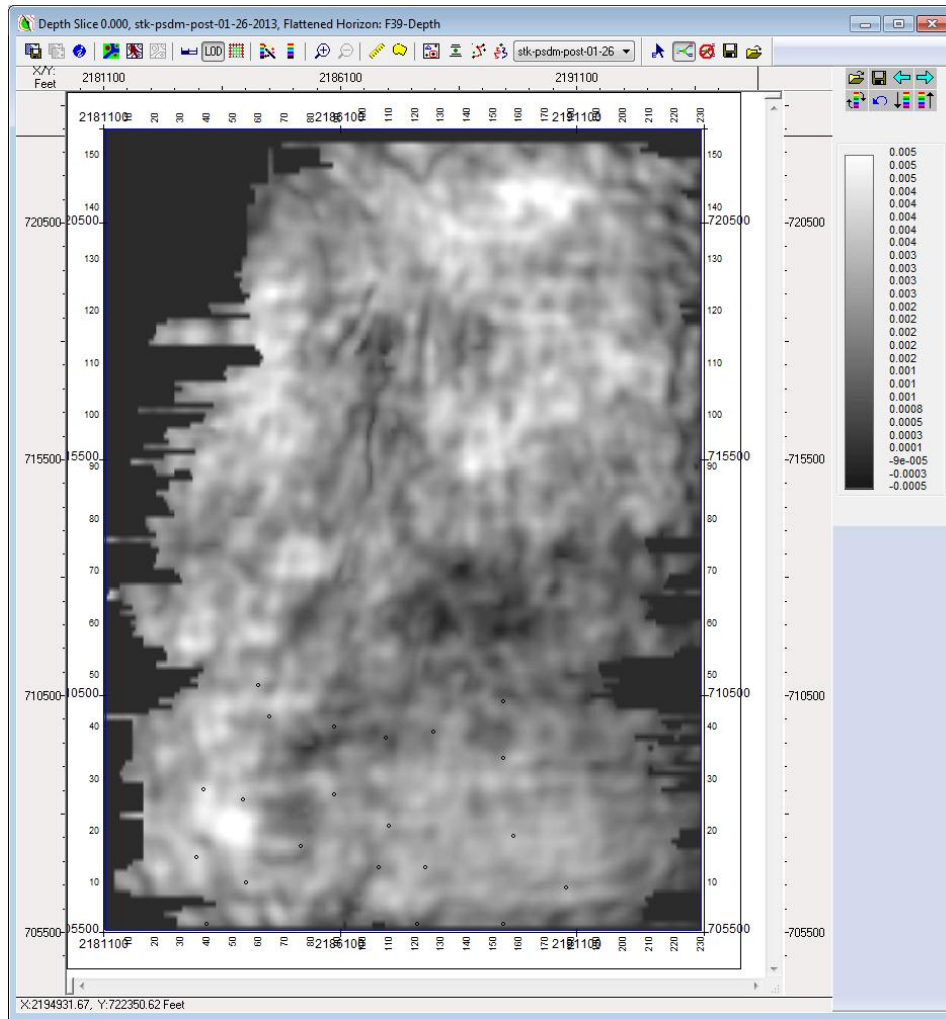


**Figure 38.** *Diffraction Imaging Stack - Depth Slice at 7230 ft*

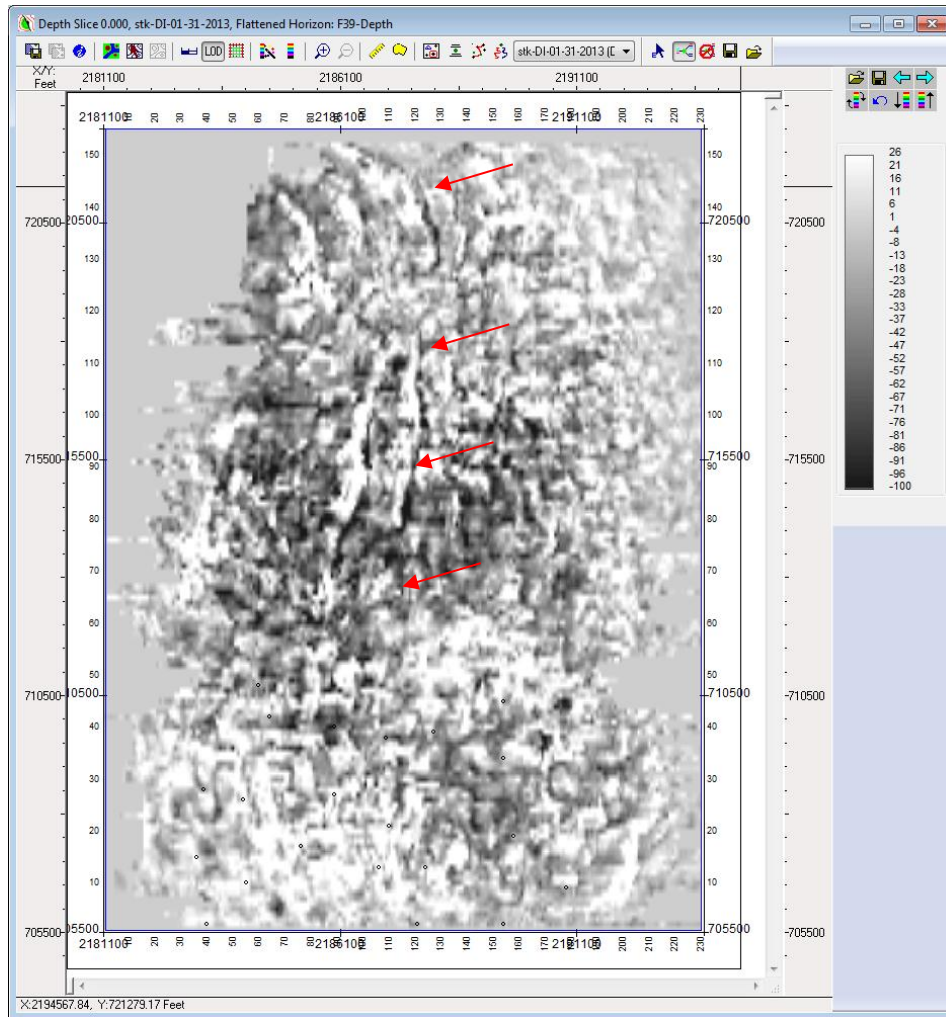
### **3.2. Results**

In the previous chapters and sections, the PSTM, the PSDM, and the DI processing sequences have been described and reviewed separately. Most of the main parameters have been informed and explained in order to understand the results.

Figure 39 shows horizon slices at formation F39 comparing the results from the PSDM (a) and the DI (b). It can be noticed the difference in resolution between the two results. The amount of detail observed in the DI results is higher than the one presented in the PSDM volume. The red arrows show specific features that could represent faults not identified in the PSDM volume.



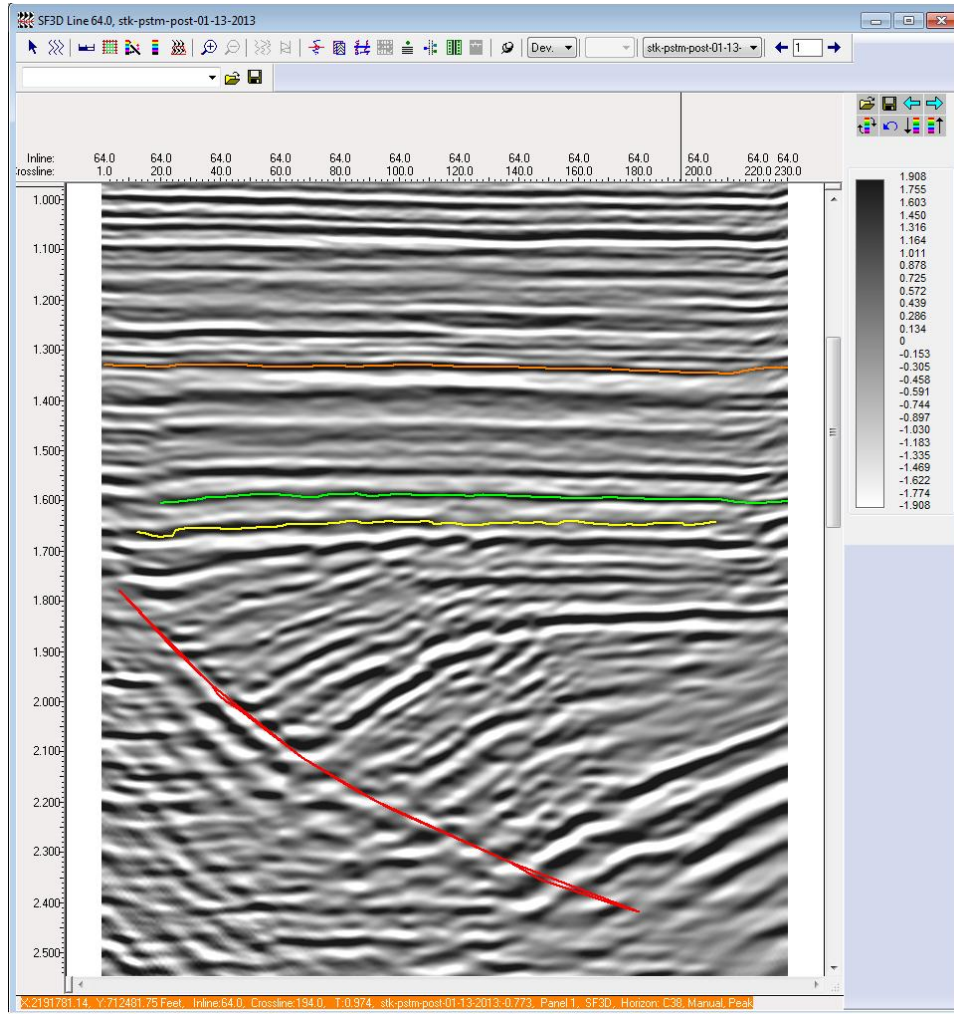
**Figure 39. (a) PSDM Volume - Horizon Slice at Formation F39**



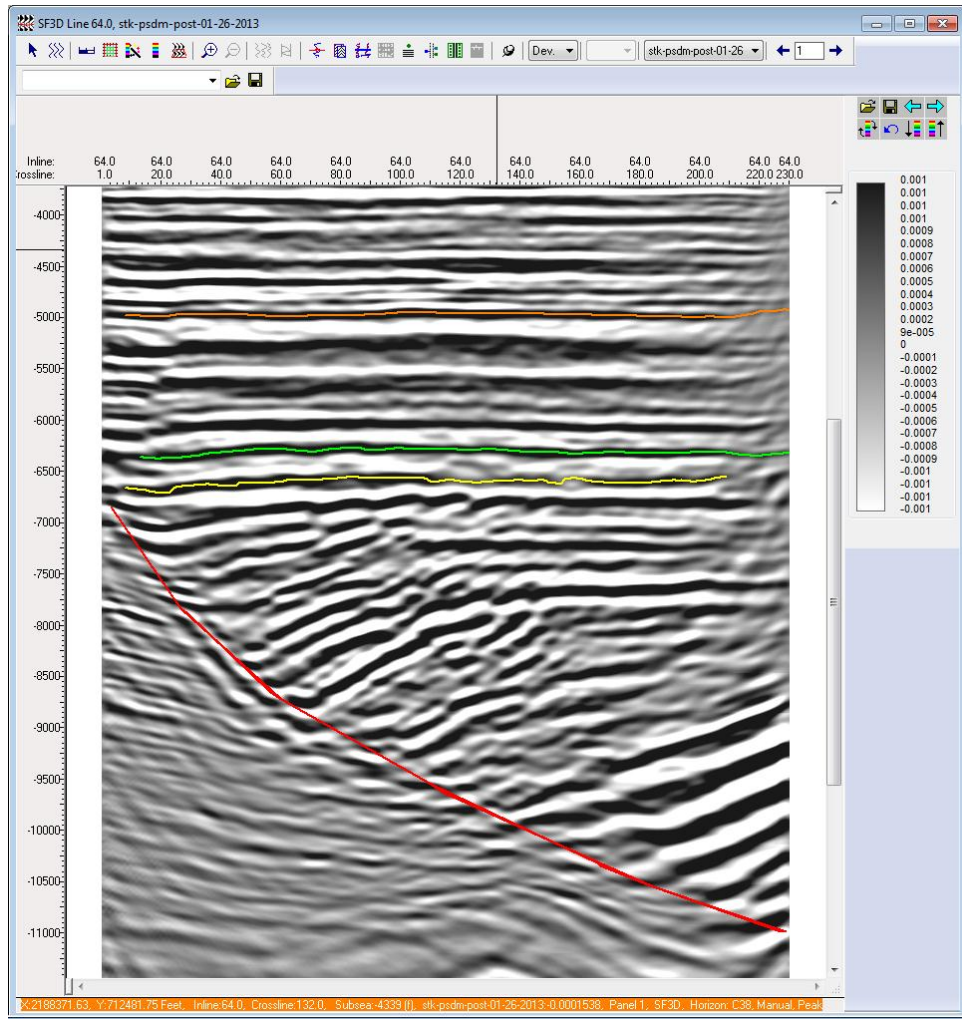
**Figure 39. (b) DI Voume - Horizon Slice at Formation F39**

Figure 40 and 41 shows a comparison in cross-section of the three stages of this work at IL 64 and XL 100. Formations C38 (orange), F11 (green), and F39 (yellow) were used as a reference and were calibrated using the well logs and the available formation tops. The mistie between the formation tops and the PSDM stack for C38 had an average of 80 ft (24 m) representing 1.58% at an average depth of 5067 ft (1544 m) using 18 wells. F11 at an average depth of 6335 ft (1930 m), the average mistie for all the wells

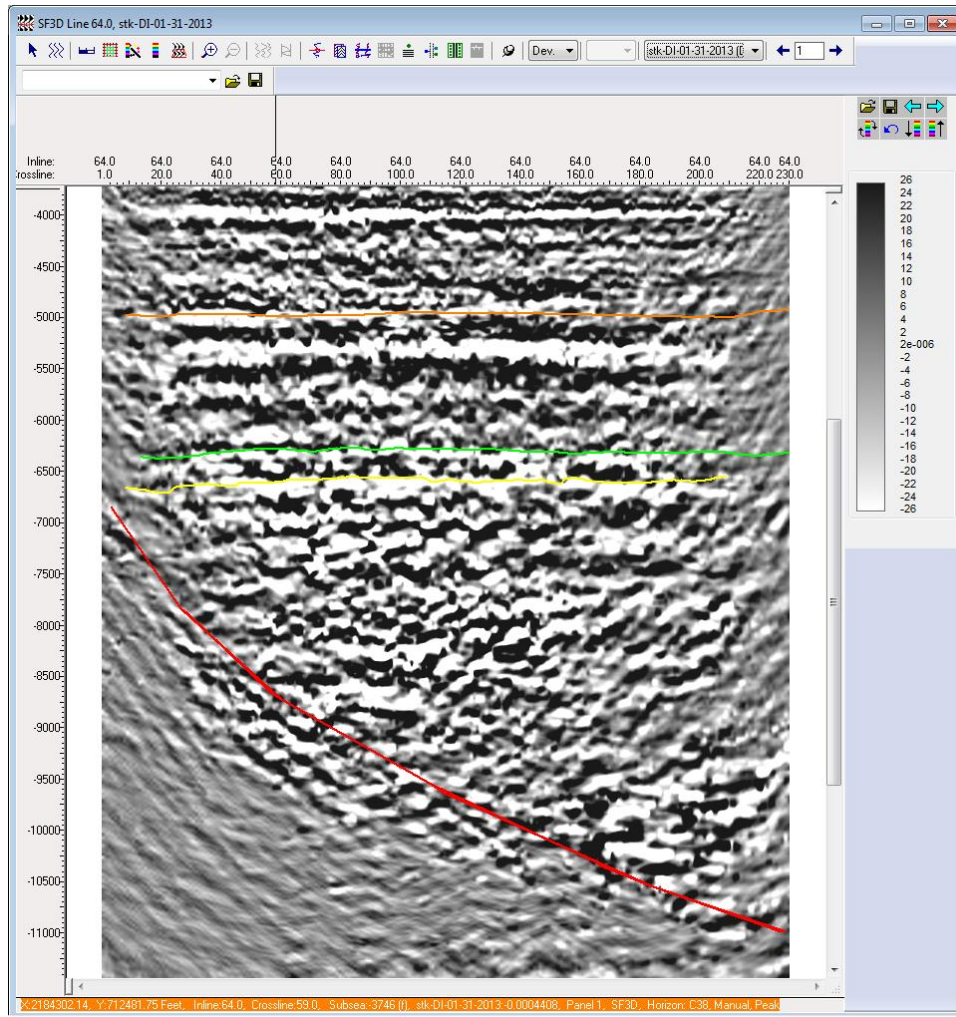
(21) was 19 ft (5.8 m) representing 0.3%. Finally at an average depth of 6674 ft (2034 m), F39, the mistie was 85 ft (26 m) approximately 1.28%. The average mistie considering the three formations in the 21 wells was 61 ft (18.6 m). The percentages showed were within the allowed error for the method.



**Figure 40. (a) PSTM Volume – IL 64**

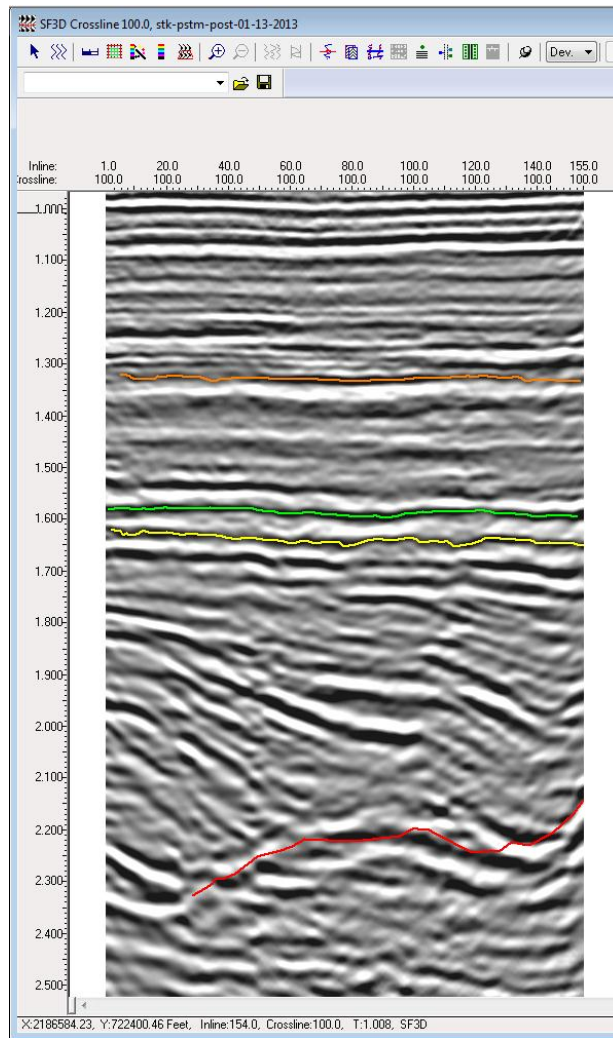


**Figure 40. (b) PSDM Volume – IL 64**

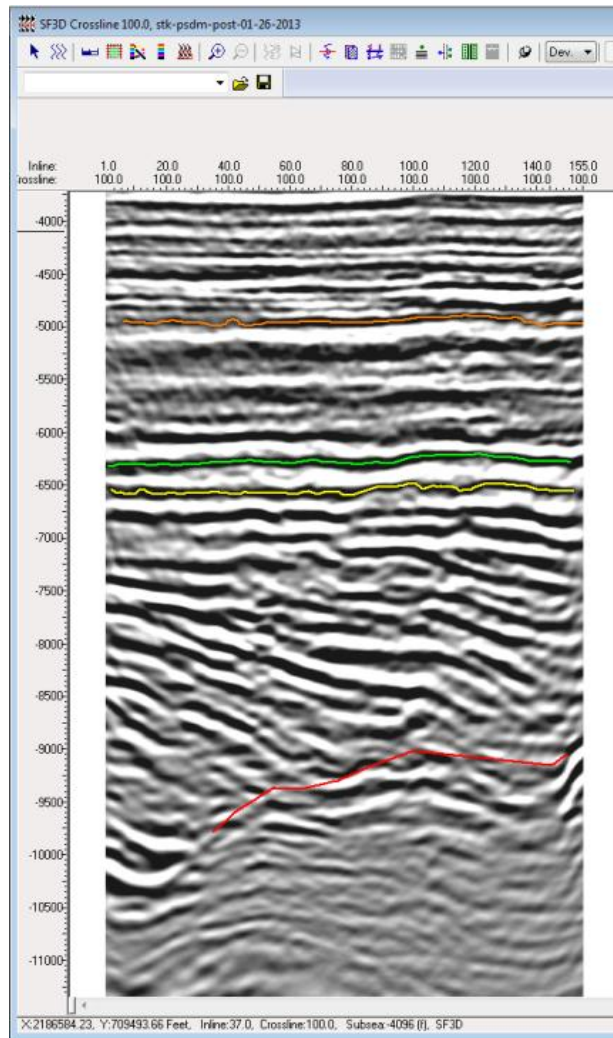


**Figure 40. (c) DI Volume – IL 64**

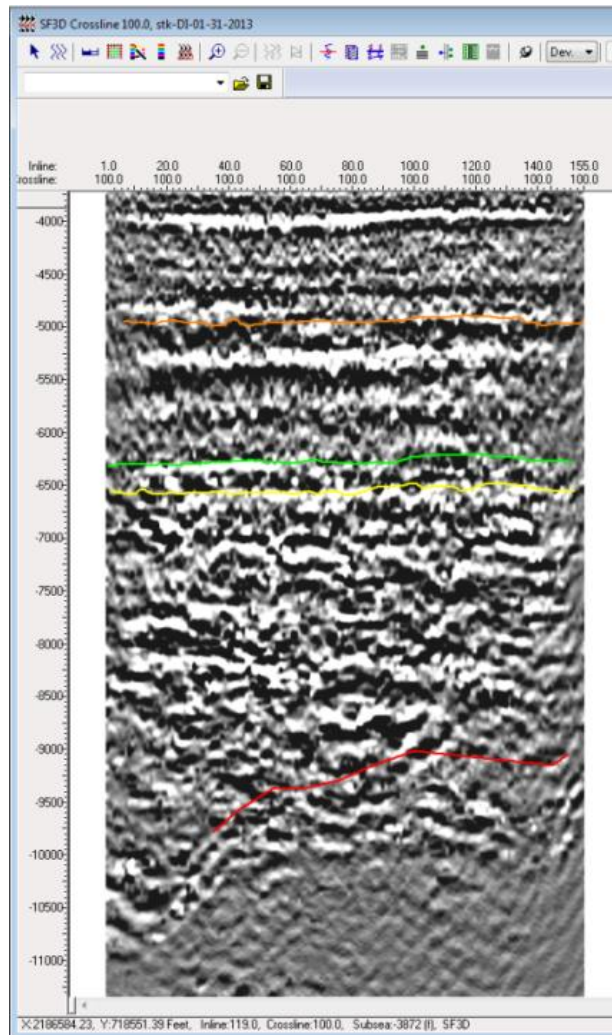
As it was expected, the PSDM stack shows the best image. The faults were better defined than the PSTM stack. Usually attributes such as Coherency, Similarity or Variance, are very useful in base map or time slice, but the image in cross section is very poor. This can be observed in the cross-section view of the DI when compared with the PSTM and PSDM stacks.



**Figure 41. (a) PSTM Volume – XL 100**



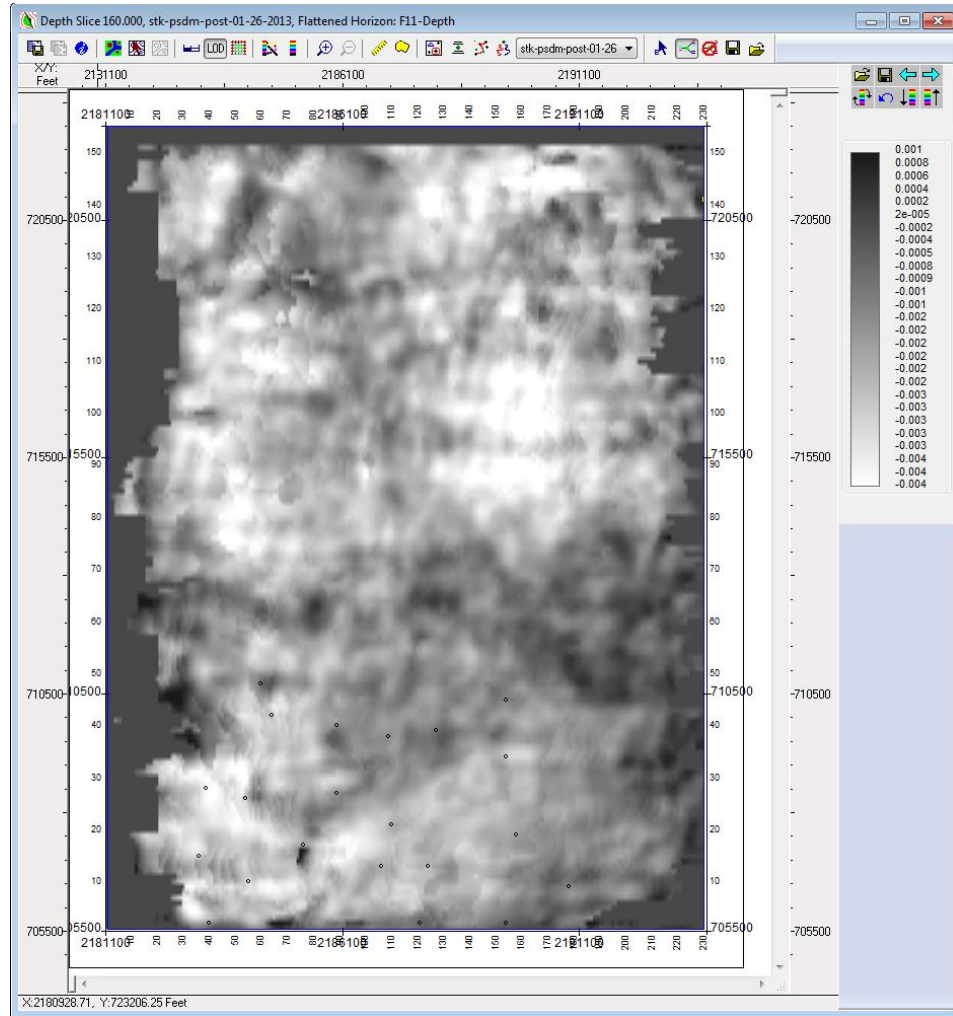
*Figure 41. (b) PSDM Volume – XL 100*



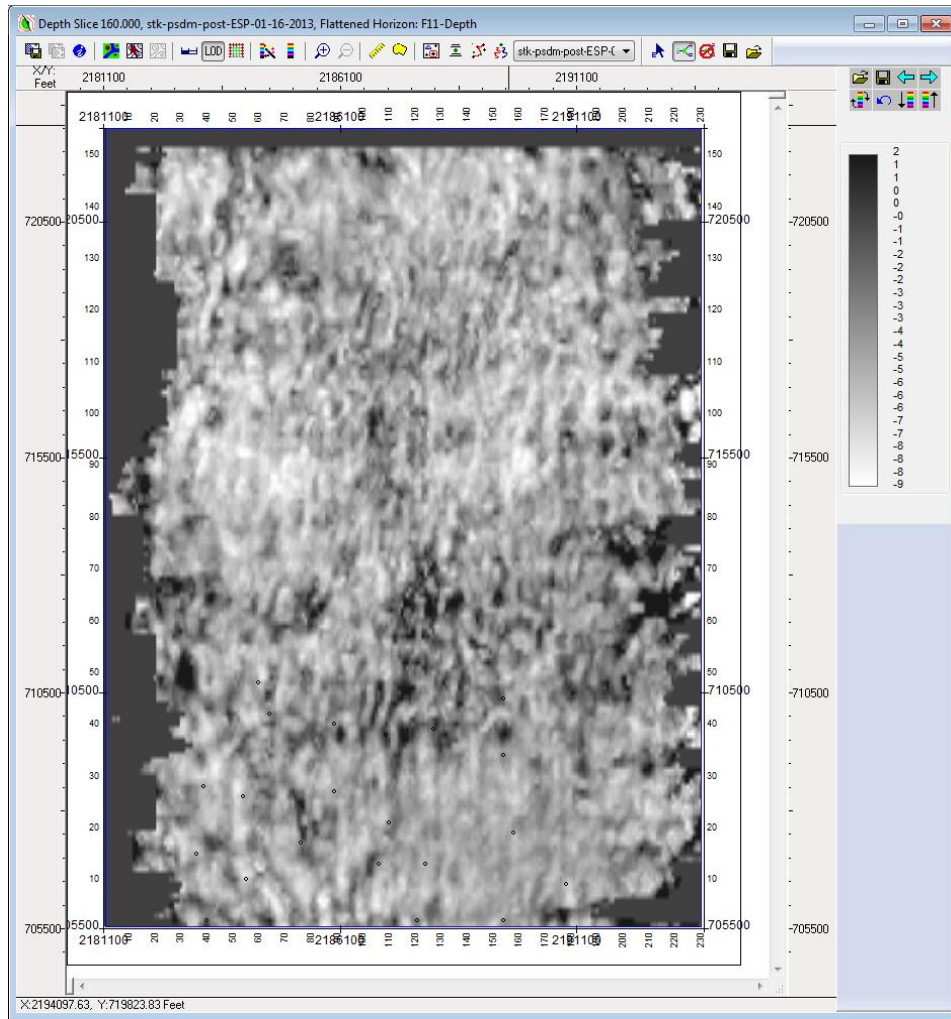
**Figure 41. (c) DI Volume – XL 100**

Figures 42, 43, and 44 shows a horizon slice at Formation F11 for the PSDM stack (Fig. 42) the PSDM Stack after ESP (Fig. 43) and DI Stack (Fig. 44). It can be observed in Figure 44, features (red arrows) that are not present in the other two horizon slices. Figure 45 shows a horizon slice at Formation F11 for the DI Stack and IL 99. The red arrow indicates a discontinuity in the horizon slice and in the cross section that cannot be observed in Figures 42 and 43.

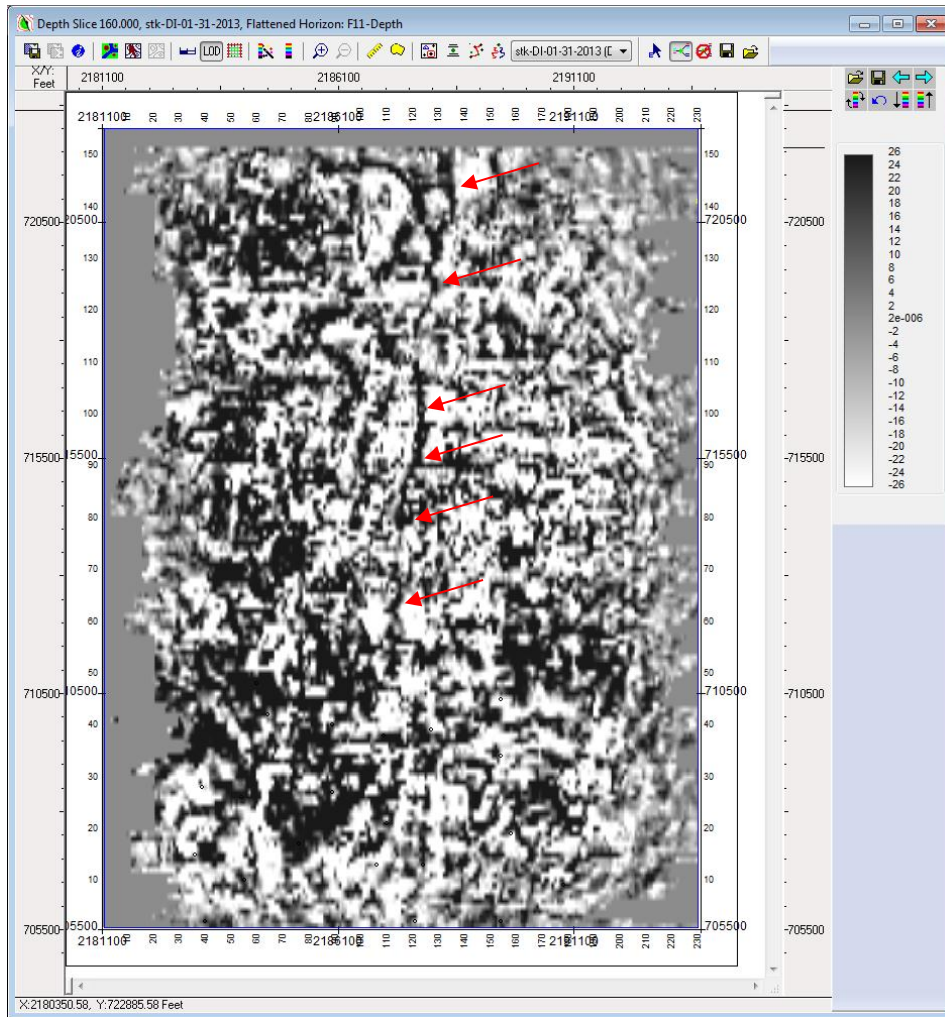
Figures 46, 47, and 48 shows a horizon slice at Formation C38 for the PSDM stack (Fig. 46) the PSDM Stack after ESP (Fig. 47) and DI Stack (Fig. 48). Again it can be observed in the Diffraction Imaging stack, features (red arrows) that are not present in the other two horizon slices.



**Figure 42.** PSDM Stack - Horizon Slice at Formation F11



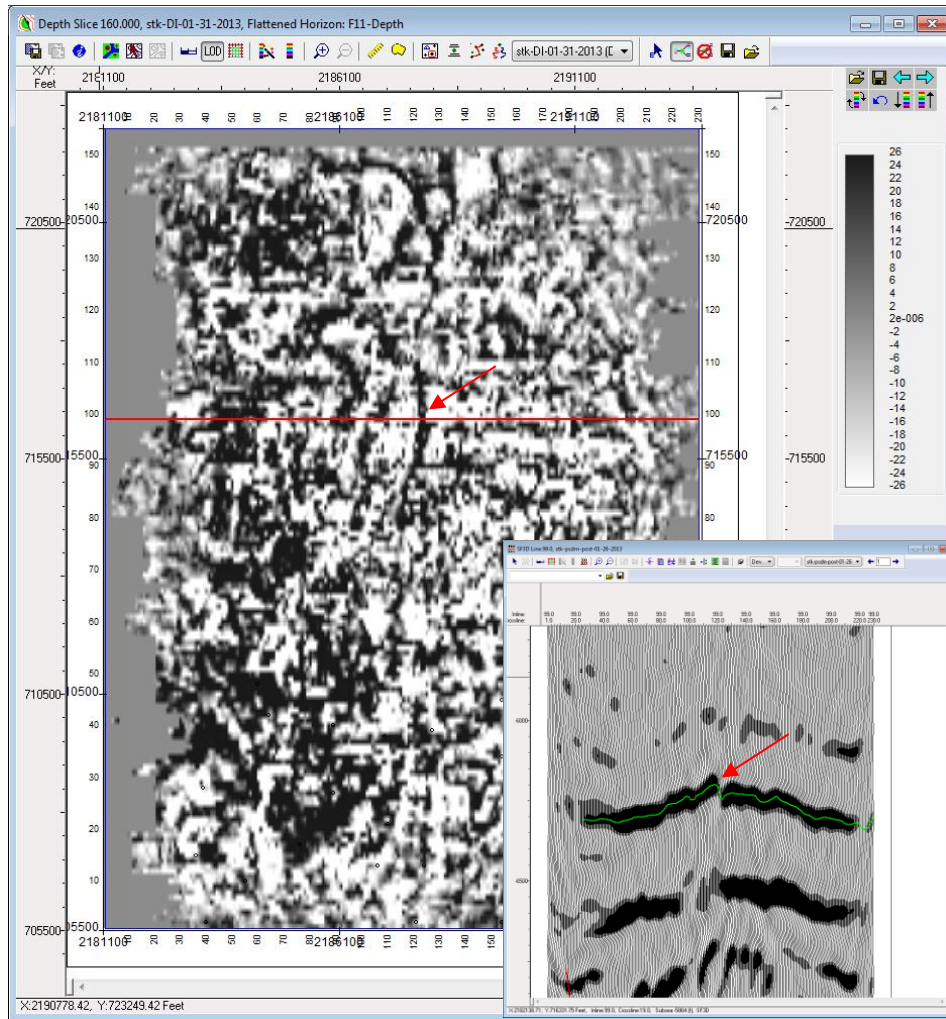
**Figure 43.** PSDM Stack after ESP - Horizon Slice at Formation F11



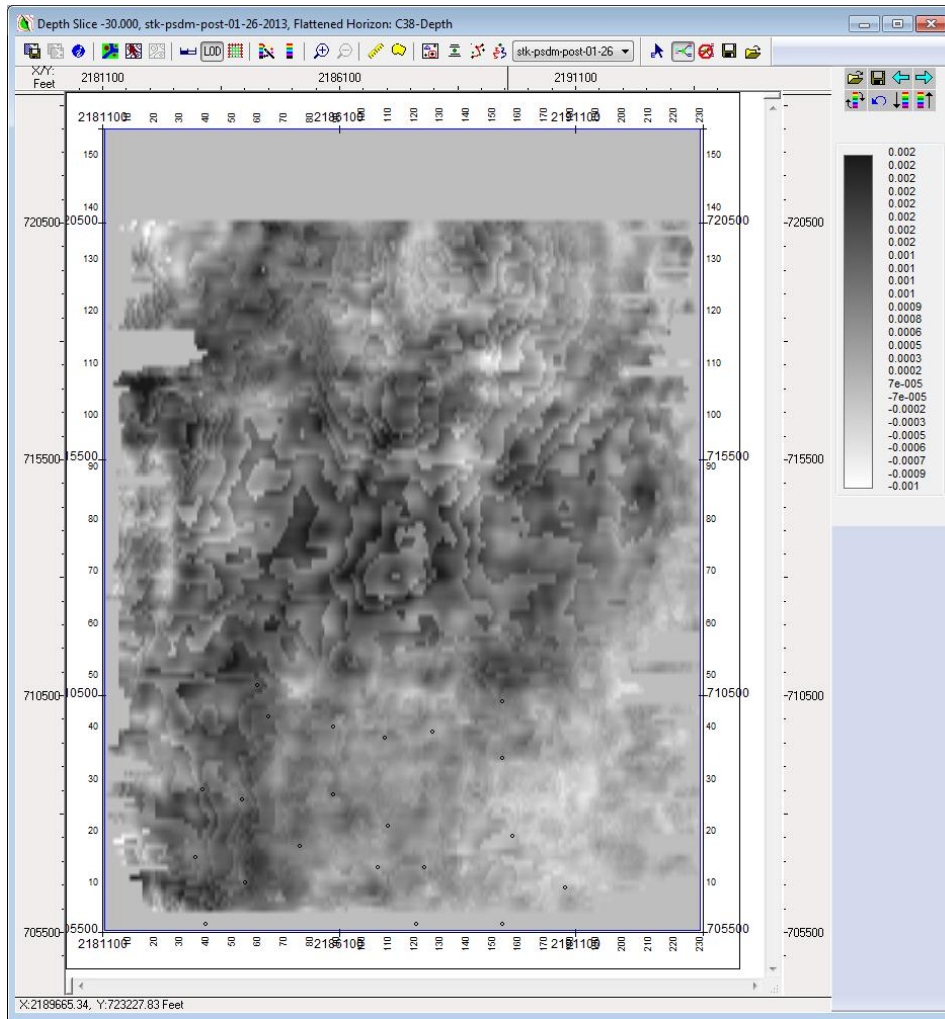
**Figure 44.** *Diffraction Imaging - Horizon Slice at Formation F11*

Figure 49 shows an arbitrary line perpendicular to the feature for the PSDM Stack. The red arrow indicates where the discontinuity is located. It can be observed a small bump in the horizon (C38 – orange) in the cross section, but there is no evidence of a discontinuity. Even though, the Diffraction Imaging shows a strong discontinuity, this type of feature is not being seen in the PSDM (Fig. 46) or in the PSDM after ESP (Fig.

47). Figure 50 shows a cross-section comparison of the PSDM volume and the DI volume where it can be seen a clear discontinuity in the DI (red arrow).



**Figure 45.** Diffraction Imaging - Horizon Slice at Formation F11 with IL 99 showing the discontinuity



**Figure 46.** PSDM Stack - Horizon Slice at Formation C38

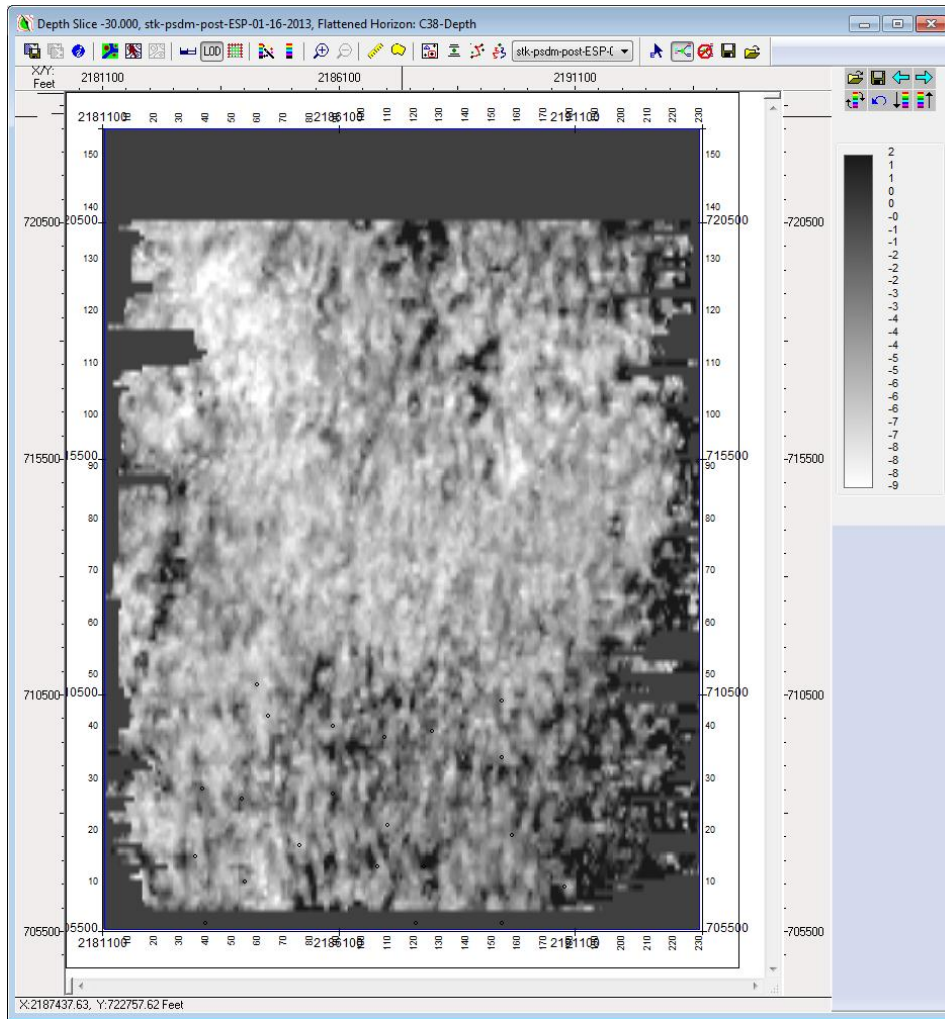


**Figure 47.** PSDM Stack after ESP - Horizon Slice at Formation C38

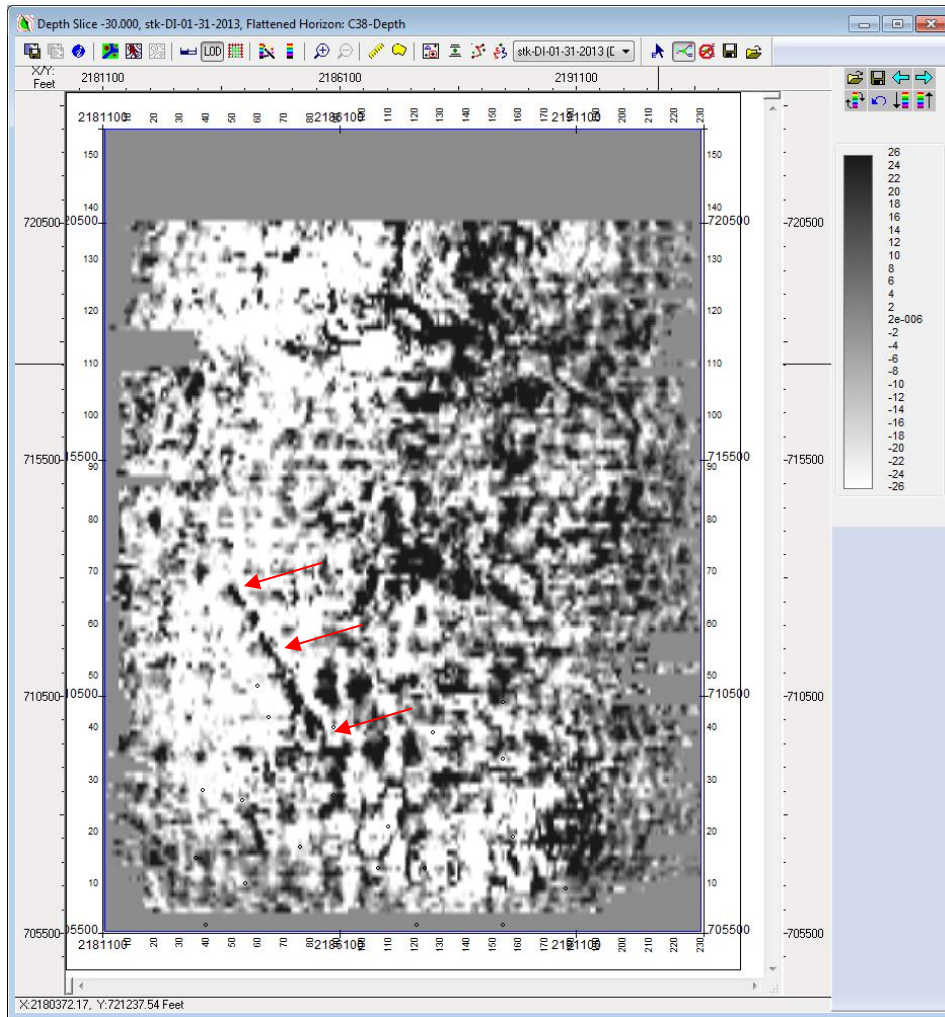


**Figure 48.** *Diffraction Imaging Stack - Horizon Slice at Formation C38*

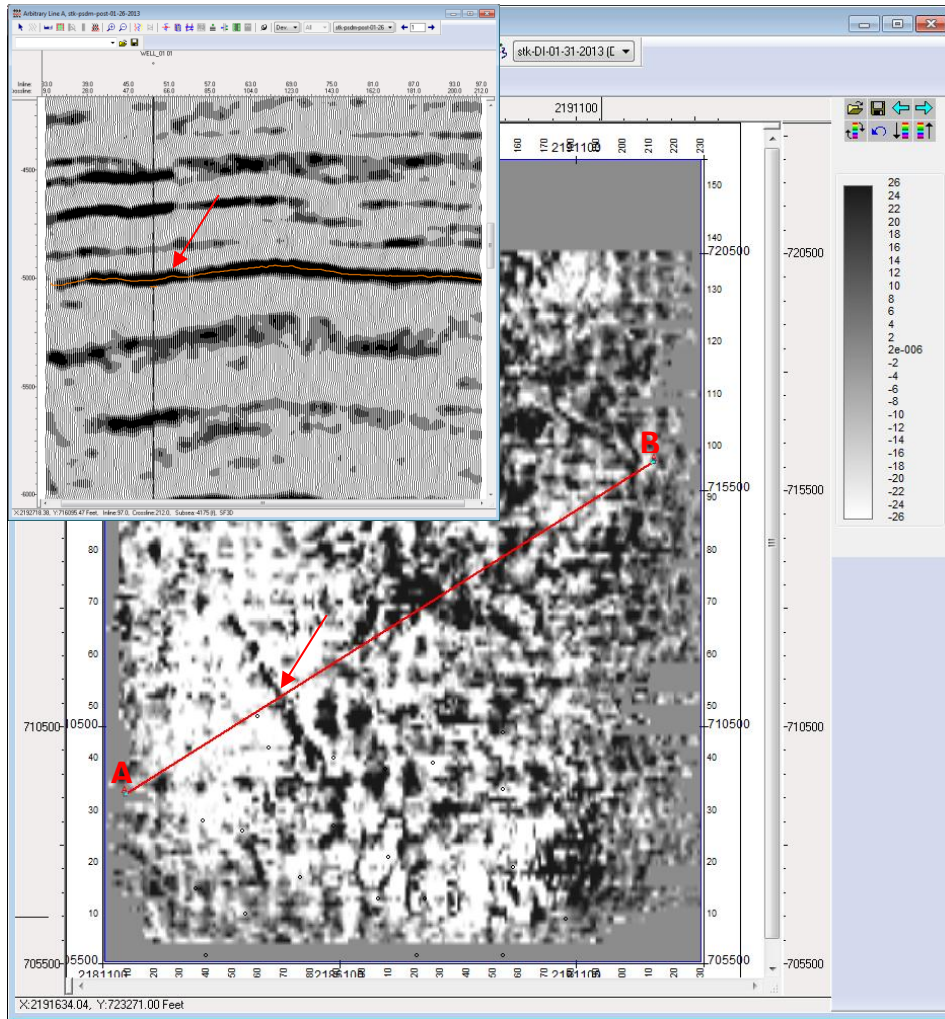


**Figure 49.** Diffraction Imaging - Horizon Slice at Formation C38 with an Arbitrary Line showing a possible discontinuity.

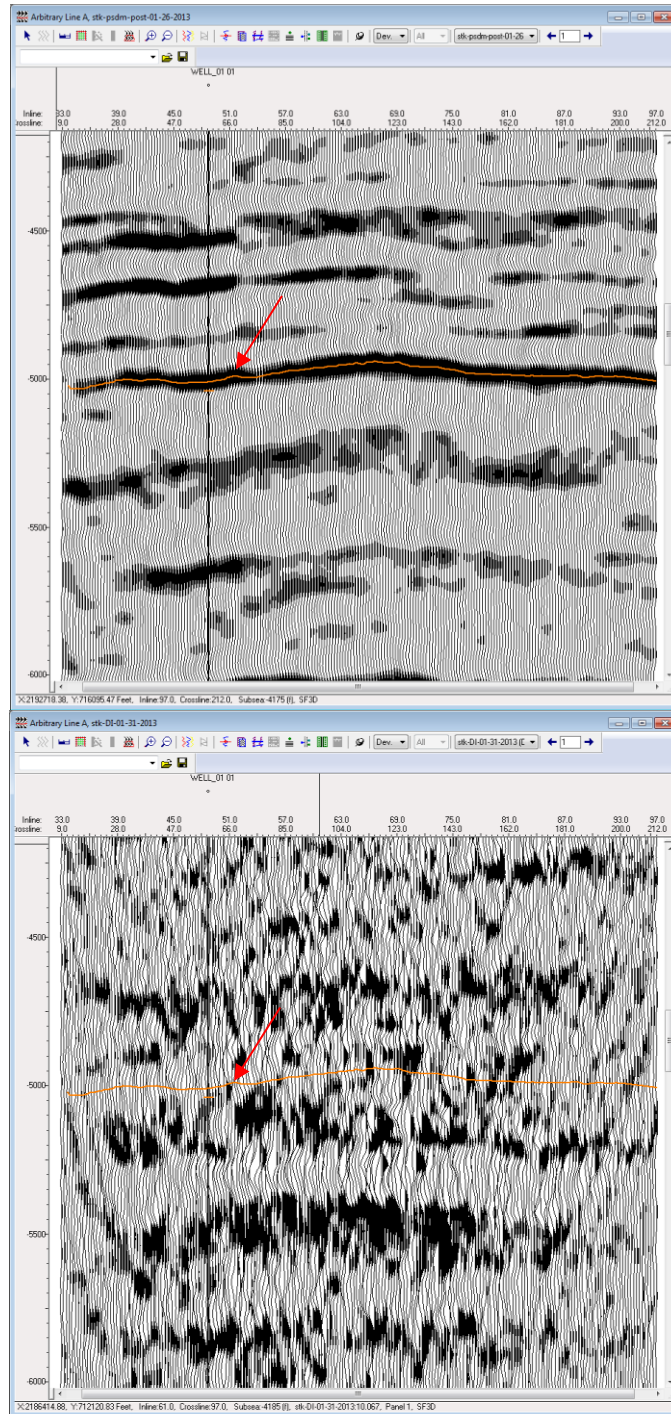


**Figure 50.** Cross sections of PSDM Volume (top) and Diffraction Imaging (bottom) – Formation C38 (Orange)

## CHAPTER 4: CONCLUSIONS

The comparison of the results shown in the previous chapter for Formation F39 (Figure 39), Formation F11 (Figures 42 to 45), and Formation C38 (Figures 46 to 50) indicates that Diffraction Imaging in depth could be used to complement conventional processing by adding a high resolution unconformities volume.

Figure 50 shows a strong feature in the Diffraction Imaging and a very small change in the PSDM volume. This could represent an advantage in areas where the faults are below conventional seismic resolution. As it was mentioned in the introduction, the need for technology that could image better the faults is crucial for non-conventional exploration and production.

Since this work is not meant to be an interpretation project, some of the identified features could represent something different from what it has been appointed. Future work could include a better understanding of the well logs and the construction of a geological model based on the available bibliography and the new results from the Diffraction Imaging technology.

It has been noticed that the acquisition footprint is enhanced in the Diffraction Imaging volume. Even though, it is not a good behavior and corresponds to the identification of discontinuities. Future work should include a Multidimensional Prestack

Regularization and Interpolation of the prestack data. The goal should be to reduce the acquisition footprint and then perform the Diffraction Imaging workflow to obtain a result and compare it with the one without interpolation.

If this technology should be evaluated, it could be said that it is a very good complement to conventional processing. The amount of detail and the identified features could represent a game changer in a drilling decision. The non-conventional explorations groups should test this technology.

A disadvantage of Diffraction Imaging could be the intensive time and effort on the previous steps and the basic idea of conventional time processing bias towards specular reflections. A full PSTM and PSDM workflow has to be done in order to gather the most accurate input data to produce a Diffraction Imaging volume. The next step in researching this field should be to reprocess the dataset avoiding certain applied processes that are known as destroyers of diffractions, such as F-XY Deconvolution. Comparing both Diffraction Imaging volumes may be very useful to identify pitfalls and limitations of the method.

Finally, results such as the ones shown in Figure 50 are very difficult to support and it could be disregarded by supporting the idea of that feature being coherent noise. It is very difficult to have full certainty when something is claimed to be under conventional seismic resolution. In order to go an extra mile, it is proposed to use Sparse

Layer Inversion (Ultra™ by Lumina Geophysical, LLC.) for the next work to invert the local frequency spectrum for the minimum number of layers that will reproduce the spectrum within the bandwidth of the recorded data. The goal will be to produce a high resolution PSDM volume, apply the same Event Similarity Prediction (ESP) algorithm and compare it with the Diffraction Imaging results. If the inversion improved the frequency of the seismic, the faults that Diffraction Imaging is enhancing should be imaged in the new PSDM after ESP volume. This should confirm once again that Diffraction Imaging has the advantage, by definition, of imaging features that are under conventional seismic resolution.

**APPENDIX: SEISMIC PROCESSING REPORT**



**STRATTON FIELD 3D**

**Kleberg & Nueces Counties, TX – USA**

**SEISMIC PROCESSING REPORT**

**- April 2013 -**

# TABLE OF CONTENTS

## SEISMIC PROCESSING REPORT

1. INTRODUCTION .....	84
2. ACQUISITION PARAMETERS .....	85
2.1 General Parameters .....	85
2.2 Vibroseis Records .....	85
2.2.1 Record Instrument .....	85
2.2.2 Receivers .....	85
2.2.3 Sources .....	85
3. SEISMIC PROCESSING REPORT .....	86
3.1 Field Data Loading and Reformatting .....	86
3.2 Geometry Building .....	86
3.3 Lines and Bins location .....	86
3.4 Shot Domain Noise Attenuation .....	87
3.5 Static Corrections .....	87
3.6 True Amplitude Recovery .....	88
3.7 Surface Consistent Amplitude Compensation .....	89
3.8 Surface Consistent Deconvolution .....	89
3.9 Velocity Analysis .....	90
3.10 Residual Static Corrections .....	90
3.11 Trim Statics .....	90
3.12 Mute Test (Stretching) .....	91
3.13 CDP Domain Noise Attenuation .....	91
3.14 Post-stack Time Migration .....	91
3.15 Pre-stack Time Migration (PSTM) .....	92
3.16 Post Processing .....	93
3.17 PSTM Final Processing Sequence .....	94
4. COMMENTS AND SUGGESTIONS .....	95
5. HEADER MAP FOR FINAL PRODUCTS .....	96
6. RESPONSIBLE STAFF .....	97
7. DELIVERABLES .....	97
8. LIST OF FIGURES .....	98

## 1. INTRODUCTION

The goal of this work was to perform a PSTM processing sequence of 92-BEG 3D (7.6 sq. mi) from Stratton Field 3D located in Kleberg and Nueces counties, South Texas. The acquisition was done by the Bureau of Economic Geology (BEG) in 1992 as an account of work sponsored by the Gas Research Institute (GRI).

Since these are public data, all the generated products including Gathers, Stacks, Velocity Fields and the Final Report will be delivered to the University of Houston, College of Natural Sciences and Mathematics, Department of Earth and Atmospheric Sciences to make it available for the student.

The obtained results will be used as an input for the PSDM workflow and later for the Diffraction Imaging sequence. Controlling the data from the acquisition helps to improve the final image. The PSTM Processing was done between March and October 2012 at DataSeismic Geophysical Services' Processing Center located in 2101 Smith St. Suite 250, Houston, TX - USA. To obtain a successful result, **ProMAX/SeisSpace R5000.0.2.0** was used for the entire processing sequence. **Focus 5.4** was used for noise attenuation and **Seismic Studio 1.6.20.0** was used for First Break Picking and Refraction Statics calculation.

## 2. ACQUISITION PARAMETERS

### 2.1 General Parameters

- Total number of receiver lines: 15
- Total number of source lines: 15
- Total processed sq mi: 7.6

### 2.2 Vibroseis records

#### 2.2.1. Record Instrument

- Instrument: N/A
- Alias filter: N/A
- Recording format: N/A
- Record length: 6 s
- Sample rate: 2 ms

#### 2.2.2. Receivers

- Receiver group interval: 110 ft
- Receiver line interval: 1320 ft
- Receiver lines per swath: 6
- Max. number of channels: 6 lines x 120 channels = 720 channels
- Minimum Offset: 134 ft
- Maximum Offset: 8341 ft
- Receiver orientation: E – W

#### 2.2.3. Sources

- Source Type (Vibrators): N/A
- Number of vibrators: 4
- Number of sweeps: 8
- Source point interval: 220 ft
- Sweep Length: N/A
- Sweep Type and frequency: Linear, 10-120 Hz
- Source line interval: 880 ft
- Source orientation: N – S
- Angle between Rcv&Sou: 90°
- Nominal Fold: 20

### 3. SEISMIC PROCESSING REPORT

The processing was done between March and October 2012 in DataSeismic Geophysical Services' Processing Center located in 2101 Smith St. Suite 250, Houston, TX - USA.

#### 3.1 Field Data Loading and Reformatting

The raw data was provided in SEG-Y format. There were no problems during data loading and reformatting to **ProMAX/SeisSpace** internal format.

#### 3.2 Geometry Building

The geometry information was in the trace headers of each seg-y file. Due to problems in the geometry building, help was requested to the Bureau of Economic Geology (BEG) at Austin, TX. Once the problem was fixed, a new set of seg-y files was generated and the geometry was completed properly.

The geometry was built with a bin of 110 ft x 55 ft (Figures A4, A5 and A6)

#### 3.3 Lines and Bins location

The following table shows inlines, crosslines and cdp's positions for the natural grid:

<b>CDP</b>	<b>INLINE</b>	<b>XLINE</b>	<b>CDP-X</b>	<b>CDP-Y</b>
1	1	1	2181139.25	705551.75
230	1	230	2181139.25	722491.75
35421	155	1	2193734.25	705551.75
35650	155	230	2193734.25	722491.75

### Live Inlines and Xlines:

Inlines: 1-155

Xlines: 1-230

### **3.4 Shot Domain Noise Attenuation**

In order to attenuate the noise in the shot domain, a proprietary noise attenuation workflow was applied to each shot.

The workflow consists in analyzing different frequency bands and identifying the high amplitude noise and the signal, followed by an adaptive filter that will put together the signal with the attenuated noise. The RMS amplitude will be calculated in order to put a threshold for what should be noise and signal.

In this dataset 7 (seven) frequency bands were selected as follows: 0-10, 10-15, 15-20, 20-30, 30-40, 40-55, 55-150 Hz. After applying the workflow, the difference between the input and the output was calculated to ensure that no coherent signal was attenuated. Also, it was stacked to ensure the improvement in the image. Results of the noise attenuation can be seen in Figures A1, A2 and A3.

### **3.5 Static Corrections**

For static corrections calculation, the delay time method was used with GLI (Generalized Linear Inversion) of Seismic Studio.

All the processing was done at a datum of 150 ft (45.72 m) as the maximum elevation was 117 ft (35.66 m). At the final stage of the processing, gathers and stacks were shifted to sea level.

The selected offset for refractor velocity calculation was 500-4000 ft (152.4-1219.2 m). A one weathering layer model was chosen. A constant weathering velocity was used, because there were no upholes or refraction profiles available. The final results can be observed in Figure A8 (refraction static map).

Model summary:

- Weathering Velocity: 4500 ft/s (1371.6 m/s)
- Refractor Velocity: 5700 – 6200 ft/s (1737.36-1889.76 m)
- First Breaks Picking Offset: 500-4000 ft (152.4-1219.2 m)
- Final Datum: 150 ft (45.72 m)
- Replacement Velocity: 6000 ft/s (1828.8 m/s)

### 3.6 True Amplitude Recovery

In order to determine the best parameters to correct for amplitude recovery, the following tests were performed. All tests were done Inline 70:

S. Spreading	Inelastic Attenuation	Curve	Length	Time-power constant	File
NO	NO	NO	2000 ms	2	tar-1
NO	NO	NO	3000 ms	2	tar-2
NO	NO	NO	3500 ms	2	tar-3
NO	NO	NO	4000 ms	2	tar-4
NO	NO	NO	3000 ms	0.5	tar-5
NO	NO	NO	3000 ms	1	tar-6

After analyzing the results we decided to use tar-2:

- Time-power constant: 2
- Application Length: 3000 ms

### 3.7 Surface consistent amplitude compensation

Once these corrections were applied, we calculated surface consistent amplitudes using receivers, shots, and offset. A noise reduction by Air Blast Attenuation (ABA) was also applied before the analysis.

Then, using the amplitudes' mean values, a trace rejection with “out of range” amplitudes was done. At this point it was important to analyze the amplitudes in order to eliminate the anomalous ones.

Finally, with the compensated amplitudes, we performed a deconvolution (see next point for description) and a new Air Blast Attenuation (ABA).

### 3.8 Surface Consistent Deconvolution

Starting with an initial autocorrelation and power spectrum, we decided to test the following operator lengths and types of deconvolution:

Type	Operator Length	Distance	White Noise	Components	File
Spiking	80 ms	-	0.10%	S-R	decon-1
Spiking	120 ms	-	0.10%	S-R	decon-2
Spiking	160 ms	-	0.10%	S-R	decon-3
Spiking	200 ms	-	0.10%	S-R	decon-4
Spiking	240 ms	-	0.10%	S-R	decon-5
Predictive	160 ms	10 ms	0.10%	S-R	decon-6
Predictive	160 ms	30 ms	0.10%	S-R	decon-7
Predictive	160 ms	10 ms	0.10%	S-R-O	decon-8
Predictive	160 ms	10 ms	0.10%	S-R-O-C	decon-9

After analyzing the results we decided to use decon-9:

- Type: Surface consistent predictive deconvolution
- Operator length: 160 ms
- White Noise: 0.10 %
- Components: Source, Receiver, Offset and CDP

### **3.9 Velocity Analysis**

We performed velocity analysis every 1000 m before first residual static calculation, and every 500 m after the first residual static calculation using Semblance, Gather, Dynamic Stack and CVS (Constant Velocity Stack).

### **3.10 Residual Static Corrections**

After the first velocity analysis we run the program Maximum Power Autostatics (Ronen-Claerbout, 1985) for Residual Static Calculation.

These static corrections are surface consistent with an analysis window width of 1800 milliseconds centered in a hand-picked horizon that followed the structural trend and a smash of 11. After the second Velocity Analysis, we run a second pass of Maximum Power Autostatics with the same parameters, diminishing dispersion. Figures A9 and A10.

### **3.11 Trim Statics**

Trim statics with the following parameters were applied:

- Statics maximum shift: 10 ms
- Min. live samples: 30%

### 3.12 Mute Test (Stretching)

Several tests with different stretch percentages were conducted:

Stretch %	File
5	mute-1
10	mute-2
15	mute-3
20	mute-4
30	mute-5
40	mute-6
50	mute-7
60	mute-8
70	mute-9

For stacking we've decided to use a stretch mute of 40%

### 3.13 CDP Domain Noise Attenuation

F-XY Decon Pre-Stack was used in order to attenuate random noise and get better continuity of events. A proprietary workflow was used to select offset ranges and apply the filter. Selected Parameters:

- Number of Inlines: 3
- Number of Xlines: 3
- Operator Length: 500 ms
- Frequency range: 5-200 Hz

### 3.14 Post-stack Time Migration

A post-stack Stolt 3D time migration was run with 100% of the velocity. The velocity field was smoothed using a smoothing operator length of 20 cdps. This migration

was done to compare and QC with the pre-stack time migration results. Figures A17 and A24.

Input	Migration Type	Vel. %	Stretch	File
stk-v2r2 fxy trim	Stolt	100	-	mig-1
stk-v2r2 fxy trim	Stolt	90	-	mig-2
stk-v2r2 fxy trim	Stolt	80	-	mig-3
stk-v2r2 fxy trim	Stolt	70	-	mig-4
stk-v2r2 fxy trim	Stolt	110	-	mig-5
stk-v2r2 fxy trim	Kirchhoff	100	5	mig-6
stk-v2r2 fxy trim	Kirchhoff	100	15	mig-7
stk-v2r2 fxy trim	Kirchhoff	100	30	mig-8

### 3.15 Pre-stack Time Migration (PSTM)

Aperture test were done over the line defining a migration aperture stretch mute in the  $x-t$  domain, considering the offsets to be migrated. The following tests were performed:

Migration Type	Stretch	Aperture Limit	File
Kirchhoff	10	-	pstm-01
Kirchhoff	20	-	pstm-02
Kirchhoff	40	-	pstm-03
Kirchhoff	60	-	pstm-04
Kirchhoff	-	0-8500	pstm-05
Kirchhoff	-	0-4000	pstm-06
Kirchhoff	-	0-2000	pstm-07
Kirchhoff	manual	-	pstm-08

After reviewing the test, we decided to use a manual picked aperture mute. A 3D Kirchhoff Pre-stack Time Migration was run on the line and new semblance (every 500 square meters) was created to do the Residual velocity analysis. We finally run another PSTM with the refined velocity. The PSTM gathers were kept with an offset range of 330 - 8250 ft., every 330 ft. between traces. Figures A18 and A25.

### **3.16 Post Process**

The following post-stack processes were applied:

- F-XY Deconvolution
- 3D Mix
- Bandpass filter
- AGC

### 3.17 PSTM Final Processing Sequence

1. Input Data (SEG-Y)
2. Geometry generation and QC
3. Minimum Phase Filter
4. Shot Domain Noise Attenuation and QC
5. Air Blast Attenuation (ABA)
6. True Amplitude Recovery (TAR):
  - 6.1. Time-power const.: 2
  - 6.2. Application Length: 3000 ms
7. Surface Consistent Amplitude Compensation (SCAC) sources, receivers and offset.
8. Surface Consistent Deconvolution:
  - 8.1. Type: Surface consistent predictive deconvolution
  - 8.2. Operator length: 160 ms
  - 8.3. White Noise: 0.10 %
  - 8.4. Components: Source, Receiver, Offset and CDP
9. Air Blast Attenuation (ABA)
10. Surface Consistent Amplitude Compensation (SCAC) sources, receivers and offset.
11. Refraction Statics Corrections application
12. First Velocity Analysis (1 every sq. km)
13. Surface Consistent Residual Statics Corrections First calculation and Application
14. Second Velocity Analysis (4 every sq. km)
15. Surface Consistent Residual Statics Corrections Second calculation and Application
16. Normal Moveout application
17. Trim Statics
18. F-XY Decon Pre-stack
19. Multidimensional Prestack Regularization & Interpolation
20. 3D Kirchhoff Pre-stack Time Migration (First Iteration)
21. First Residual Velocity Analysis (4 every sq. km)
22. 3D Kirchhoff Pre-stack Time Migration (Second Iteration)
23. Second Residual Velocity Analysis (4 every sq. km)
24. Final 3D Kirchhoff Pre-stack Time Migration
25. CRP gathers generation
26. Front Mute (MUTE)
27. Stack & shift to Final Datum, (D=sea level, VR=6000 ft/s)
28. F-XY Deconvolution
29. AGC (1000 ms)
30. Band Pass Filter (5-8-100-150 Hz)

#### **4. COMMENTS AND SUGGESTIONS**

The overall data quality shown in the stacks is very good. It presents a good signal-to-noise ratio and continuity of the events. The main challenge of this dataset was to improve the steep dips produced by Agua Dulce growth fault. Two other issues are pointed out and would be addressed in a future appendix to this work.

The first one is the presence on multiples generated by the stack of shale-sand-shale sequence in the first 1500 ms. It can be seen in the deeper part where the structure tends to have certain dips. The second issue is the acquisition footprint noticed in the first at least 1250 ms. A Prestack Multidimensional Regularization and Interpolation will be applied to solve it.

A CDP-Gather with statics and pre-processing and a velocity field will be delivered and it could be the input to any de-multiple and/or interpolation process.

The next step will include Prestack Depth Migration in order to improve the image in the areas where conventional PSTM Processing is not good enough to resolve complex structures and velocity fields.

## 5. HEADER MAPS - FINAL PRODUCTS

The following table describes the location and type of the information included in the trace headers, in all final stacks and migrations:

Bytes 21-24	(Integer)	CDP
Bytes 33-34	(Integer)	Trace Fold
Bytes 181-184	(Integer)	CDP X Coordinates
Bytes 185-188	(Integer)	CDP Y Coordinates
Bytes 189-192	(Integer)	INLINE
Bytes 193-196	(Integer)	XLINE
Bytes 205-208	(Integer)	CDP Elevation

The following table describes the location and type of the information included in the trace headers of the CDP and CRP GATHERS:

Bytes 1-4	(Integer)	Trace no.
Bytes 9-12	(Integer)	Field File ID.
Bytes 13-16	(Integer)	Channel number
Bytes 21-24	(Integer)	CDP
Bytes 33-34	(Integer)	CDP Fold
Bytes 37-40	(Integer)	Offset
Bytes 41-44	(Integer)	Receiver Elevation
Bytes 45-48	(Integer)	Source Elevation
Bytes 73-76	(Integer)	Source X
Bytes 77-80	(Integer)	Source Y
Bytes 81-84	(Integer)	Receiver X
Bytes 85-88	(Integer)	Receiver Y
Bytes 111-112	(Integer)	Mute
Bytes 181-184	(Integer)	CDP X
Bytes 185-188	(Integer)	CDP Y
Bytes 189-192	(Integer)	INLINE
Bytes 193-196	(Integer)	XLINE
Bytes 205-208	(Integer)	CDP Elevation
Bytes 217-220	(Integer)	Receiver Line
Bytes 221-224	(Integer)	Receiver Station
Bytes 225-228	(Integer)	Source Line
Bytes 229-232	(Integer)	Source Station

## 6. RESPONSIBLE STAFF

- Alejandro Juranovic

## 7. DELIVERABLES

- One (1) Hard Drive containing the following products:
  - Field RAW data with applied geometry
  - CDP-Gathers
  - PSTM Gathers
  - Conditioned PSTM Gathers
  - Conditioned Near Offset (0-25°) PSTM Gathers
  - Conditioned Mid Offset (20-40°) PSTM Gathers
  - Conditioned Far Offset (35-60°) PSTM Gathers
  - Final Stack (RAW)
  - Final Stack (Enhanced)
  - Post-stack Time Migrated Stack (RAW)
  - Post-stack Time Migrated Stack (Enhanced)
  - PSTM Stack (RAW)
  - PSTM Stack (Enhanced)
  - Near Offset PSTM Stack (0-25°)
  - Mid Offset PSTM Stack (20-40°)
  - Far Offset PSTM Stack (35-60°)
  - PSDM Stack (RAW)
  - PSDM Stack (Enhanced)
  - Diffraction Imaging Stack (RAW)
  - Diffraction Imaging Stack (Enhanced)
  - RMS Velocity Field in Time
  - Migration RMS Velocity Field in Time
  - Interval Velocity Field in Time
  - Interval Velocity Field in Depth
  - Final Processing Report

## LIST OF FIGURES

Figure A1: Shot before shot domain noise attenuation.....	99
Figure A2: Shot after shot domain noise attenuation.....	100
Figure A3: Attenuated noise.....	101
Figure A4: Base map.....	102
Figure A5: Processing grid.....	103
Figure A6: Fold map.....	104
Figure A7: Topography map.....	105
Figure A8: Refraction Statics map.....	106
Figure A9: First Residual Statics map.....	107
Figure A10: Second Residual Statics map.....	108
Figure A11: Location of IL 70 and XL 110.....	109
Figure A12: Brute stack with Elevation Statics – IL 70.....	110
Figure A13: Brute stack with Refraction Statics – IL 70.....	111
Figure A14: Stack with First Velocity Analysis and Residual Statics – IL 70.....	112
Figure A15: Stack with Second Velocity Analysis and Residual Statics – IL 70.....	113
Figure A16: Final Stack – IL 70.....	114
Figure A17: Post-stack Migration – IL 70.....	115
Figure A18: PSTM Stack – IL 70.....	116
Figure A19: Brute stack with Elevation Statics – XL 110.....	117
Figure A20: Brute stack with Refraction Statics – XL 110.....	118
Figure A21: Stack with First Velocity Analysis and Residual Statics – XL 110.....	119
Figure A22: Stack with Second Velocity Analysis and Residual Statics – XL 110.....	120
Figure A23: Final Stack – XL 110.....	121
Figure A24: Post-stack Migration – XL 110.....	122
Figure A25: PSTM Stack – XL 110.....	123
Figure A26: PSTM stack - Time Slice 750 ms.....	124
Figure A27: PSTM stack - Time Slice 1000 ms.....	125
Figure A28: PSTM stack - Time Slice 1250ms.....	126
Figure A29: PSTM stack - Time Slice 1500 ms.....	127
Figure A30: PSTM stack - Time Slice 1750 ms.....	128
Figure A31: PSTM stack - Time Slice 2000 ms.....	129
Figure A32: PSTM stack - Time Slice 2250 ms.....	130
Figure A33: PSTM stack - Time Slice 2500 ms.....	131
Figure A34: PSTM stack - Time Slice 2750 ms.....	132
Figure A35: PSTM stack - Time Slice 3000 ms.....	133
Figure A36: PSTM stack - Time Slice 3250 ms.....	134
Figure A37: PSTM stack - Time Slice 3500 ms.....	135

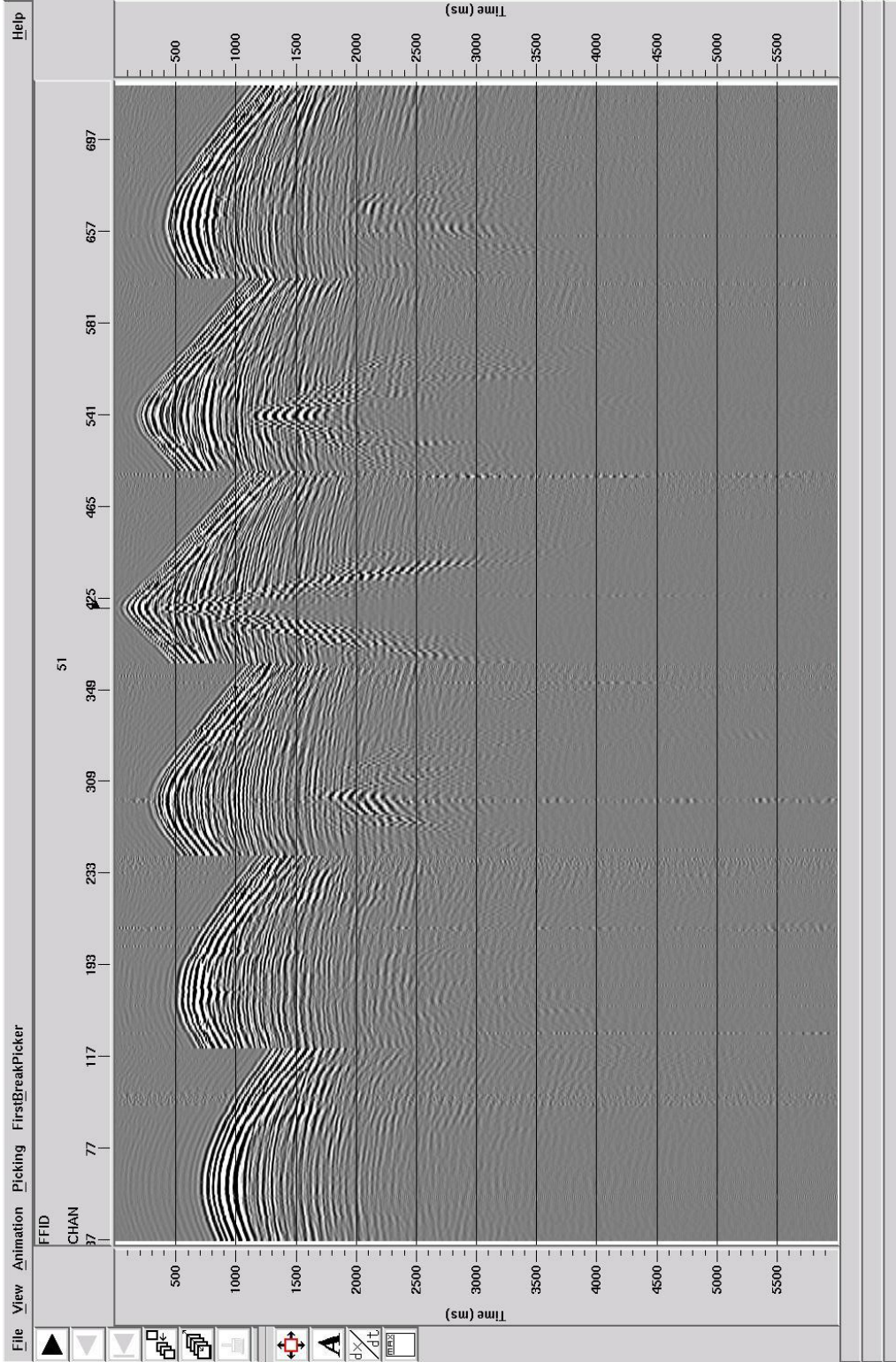


**Figure A1: Shot before noise attenuation**

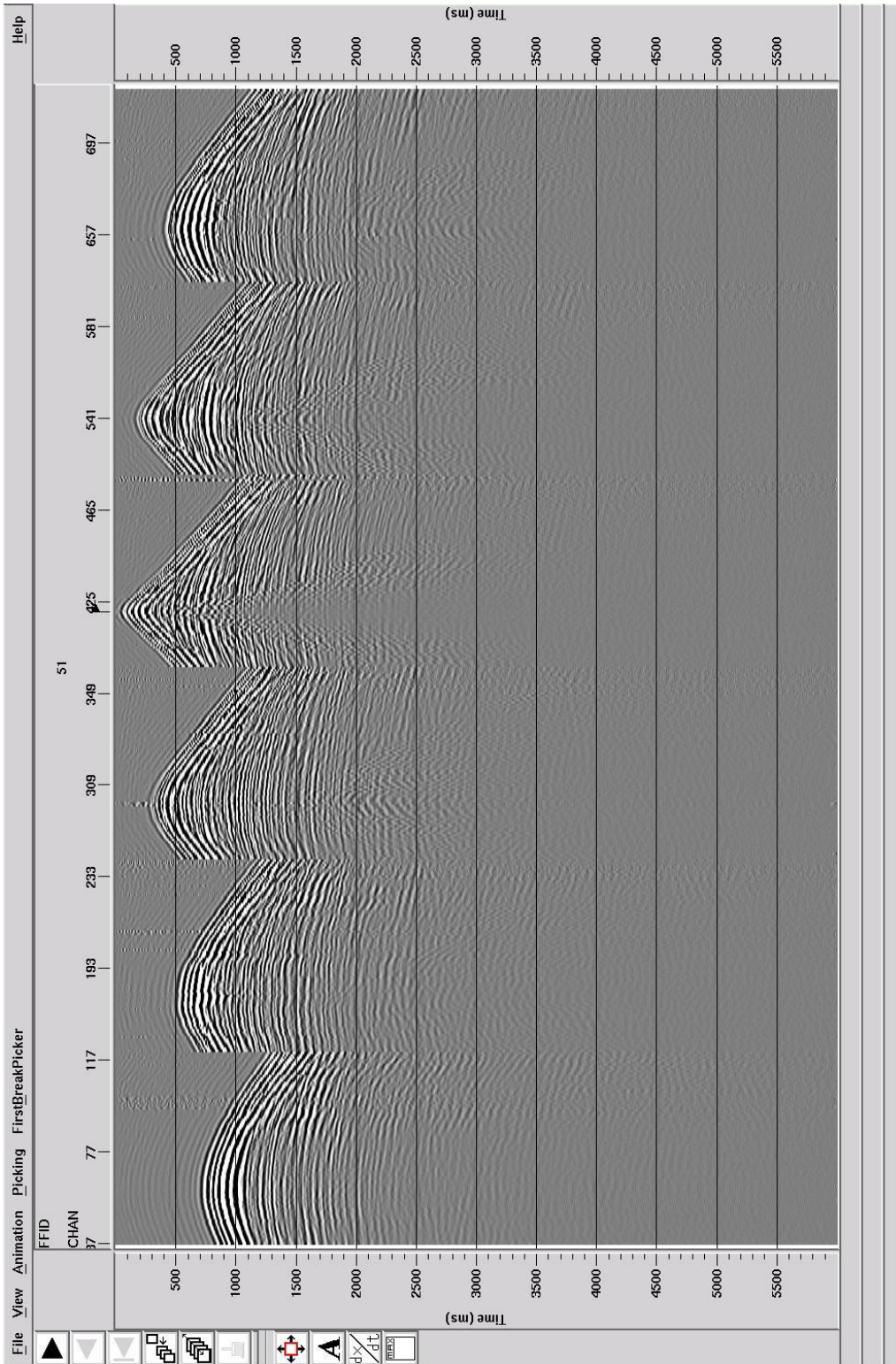


**Figure A2: Shot after noise attenuation**

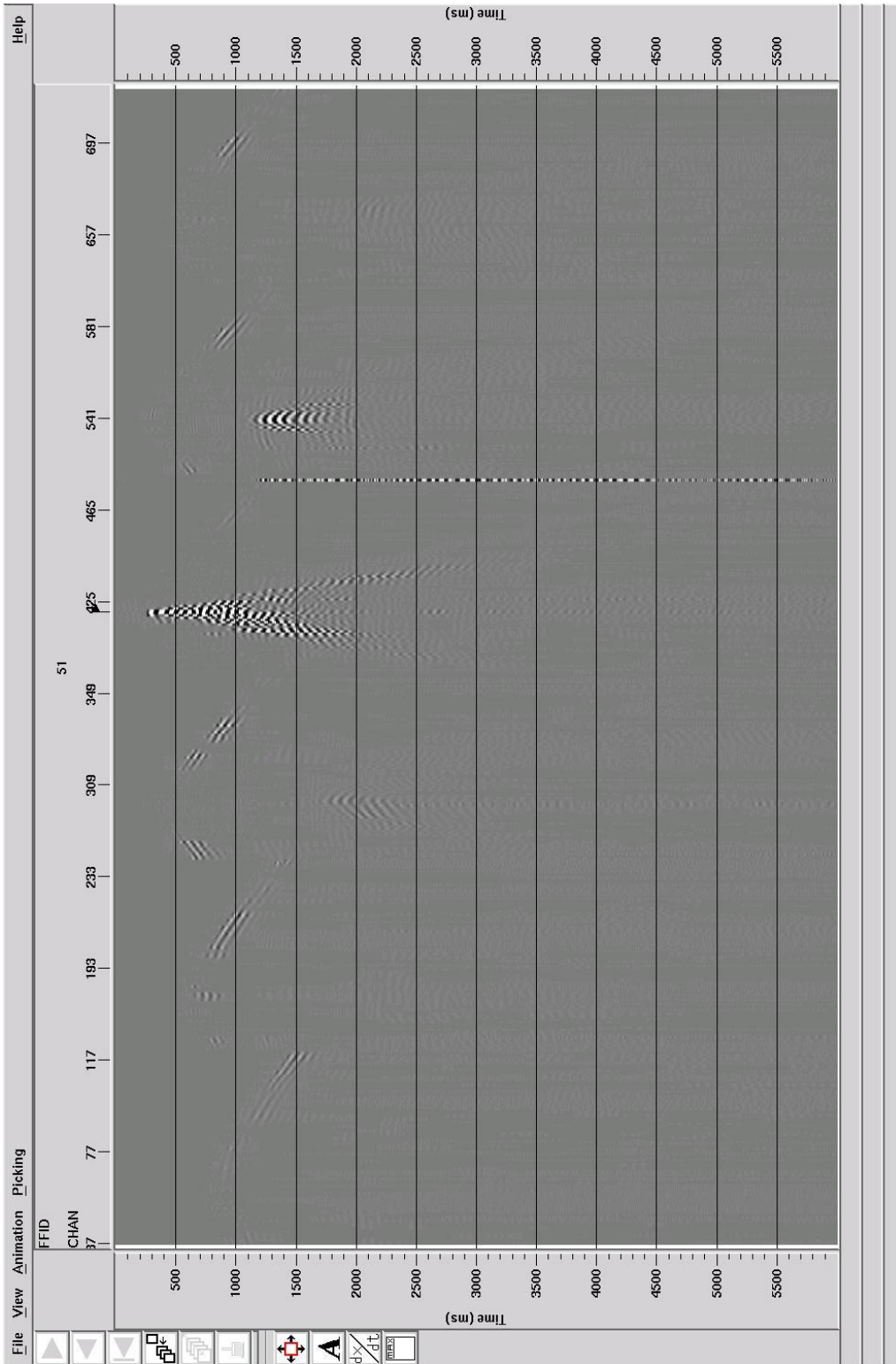
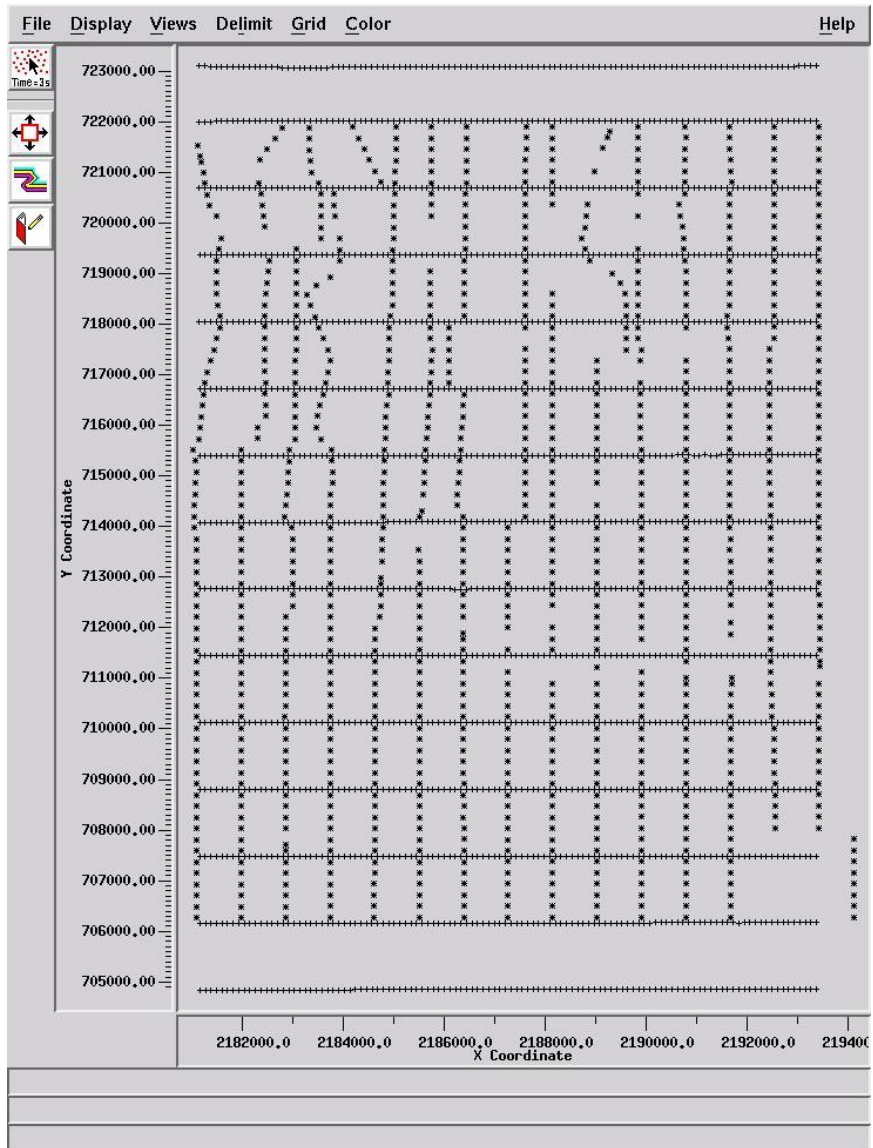
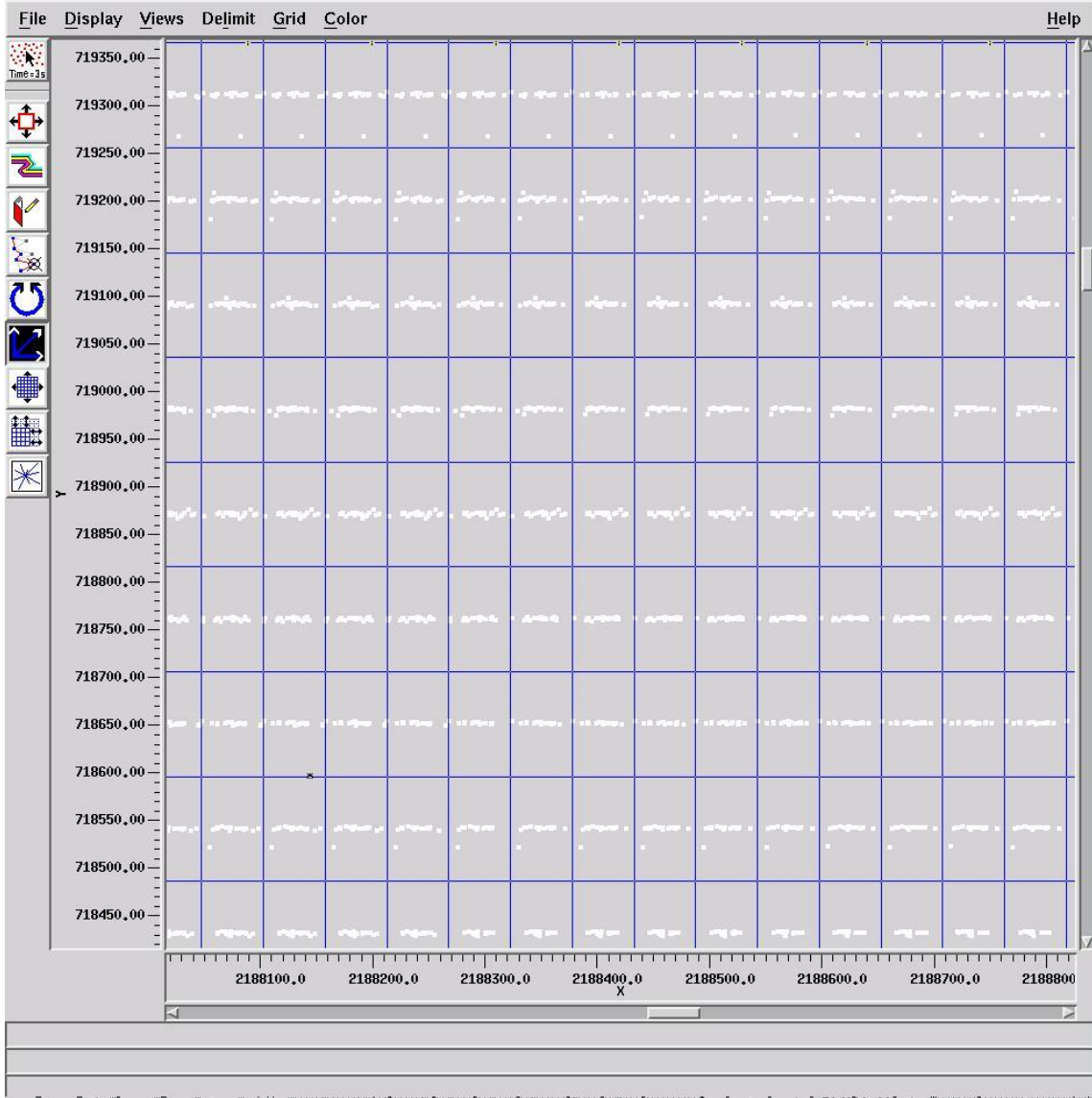


Figure A3: Attenuated Noise



**Figure A4: Base Map**



**Figure A5: Processing Grid**

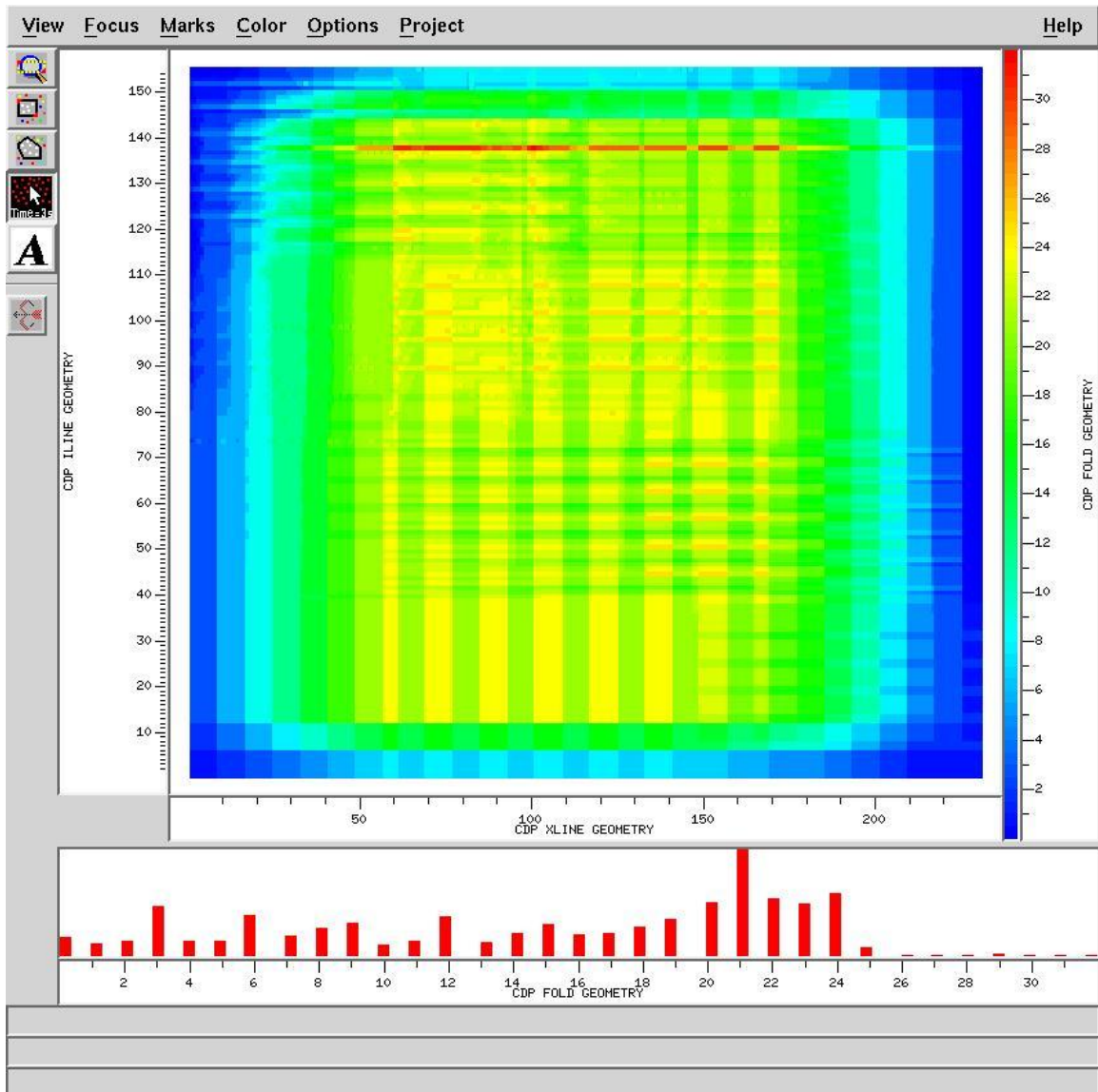


**Figure A6: Fold Map**

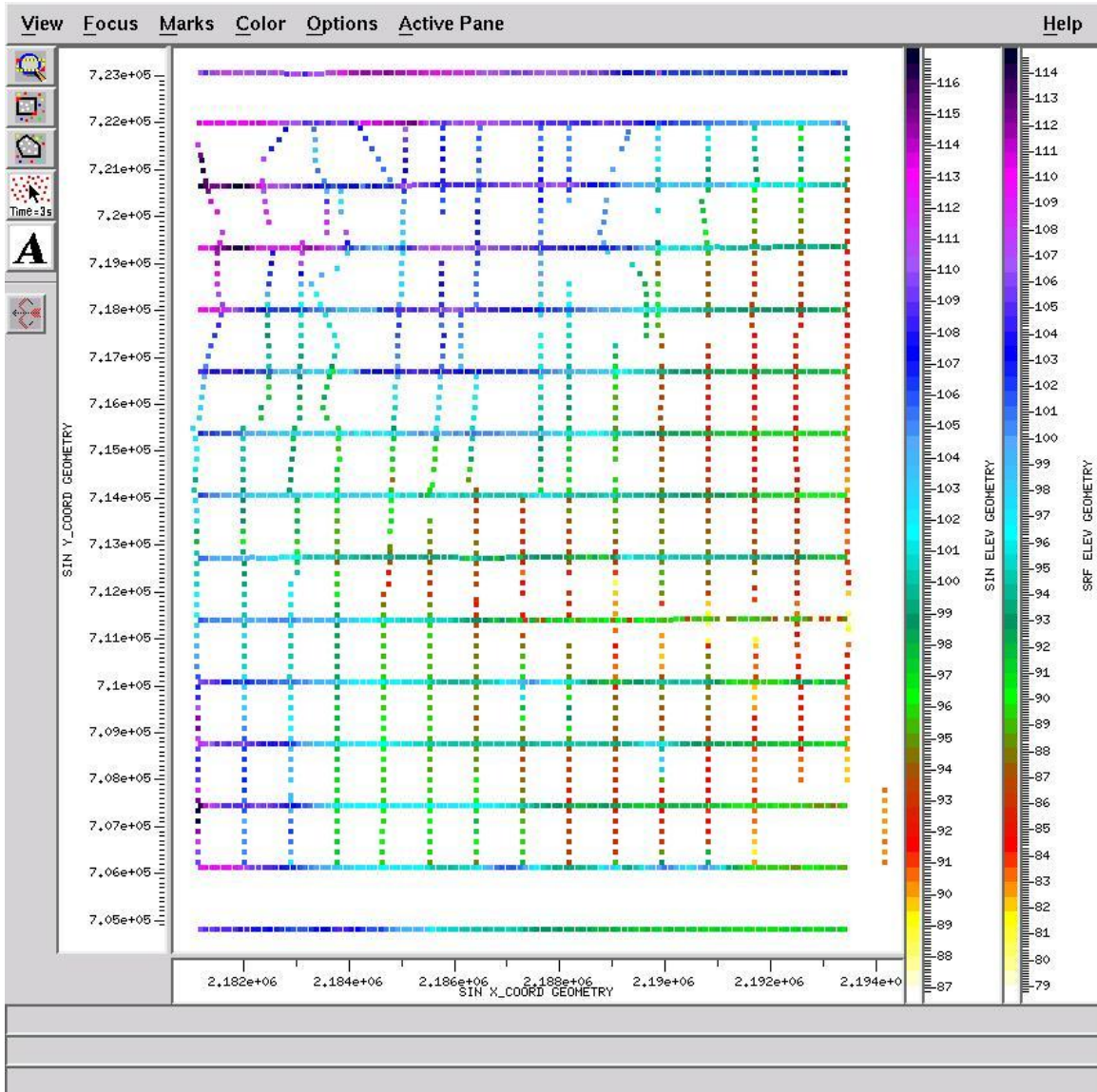
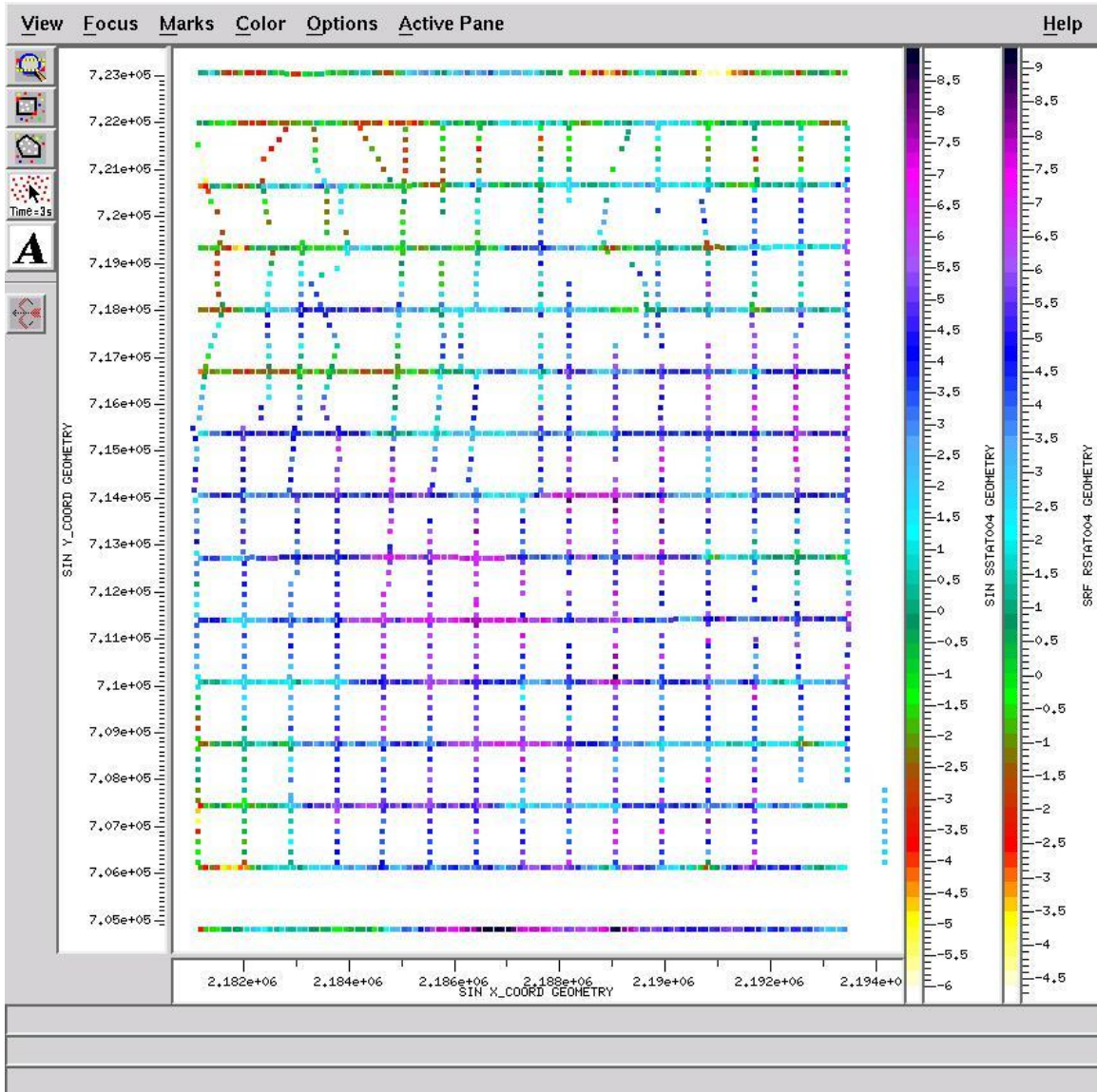


Figure A7: Topography Map



**Figure A8: Refraction Statics Map**

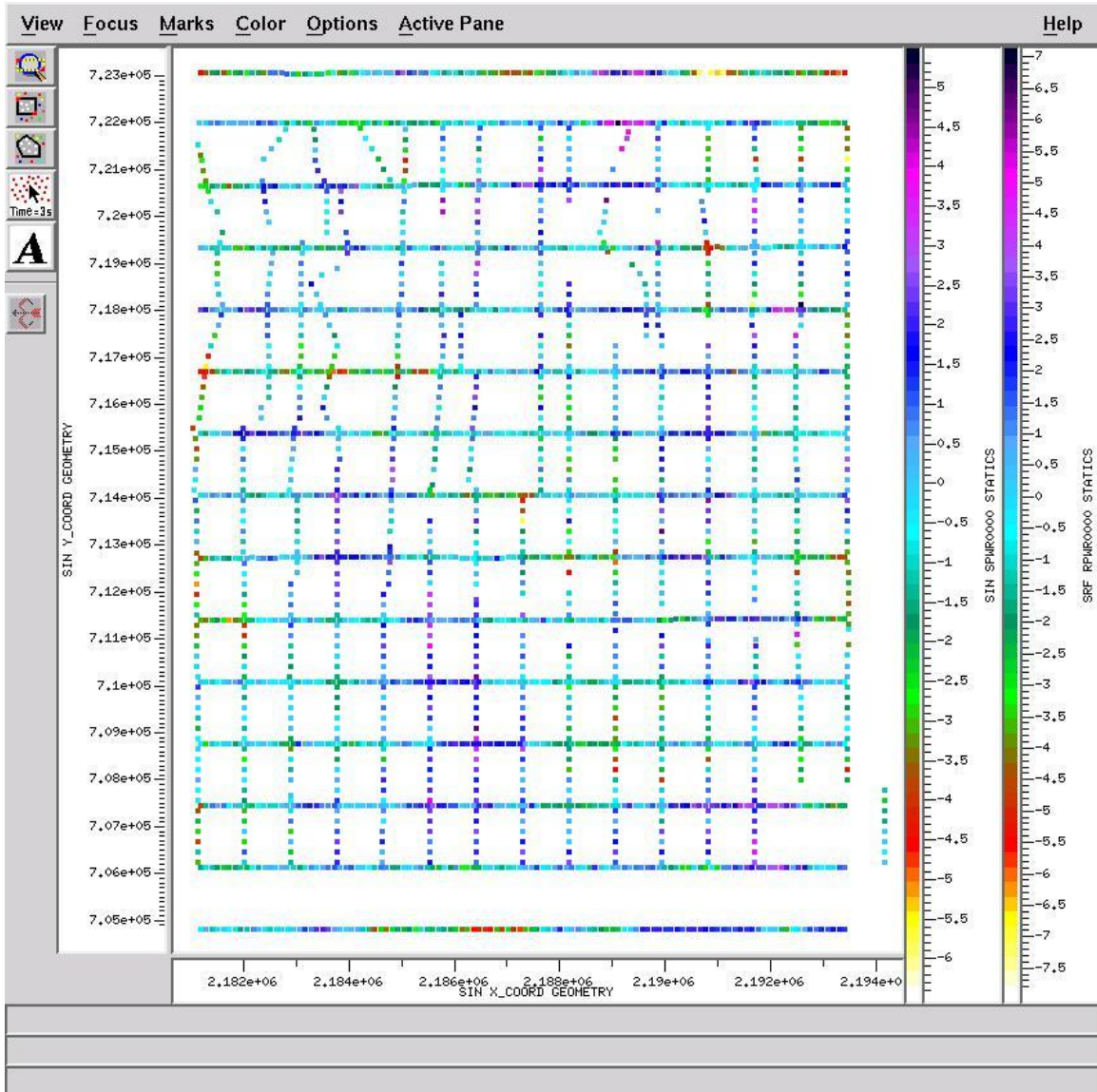
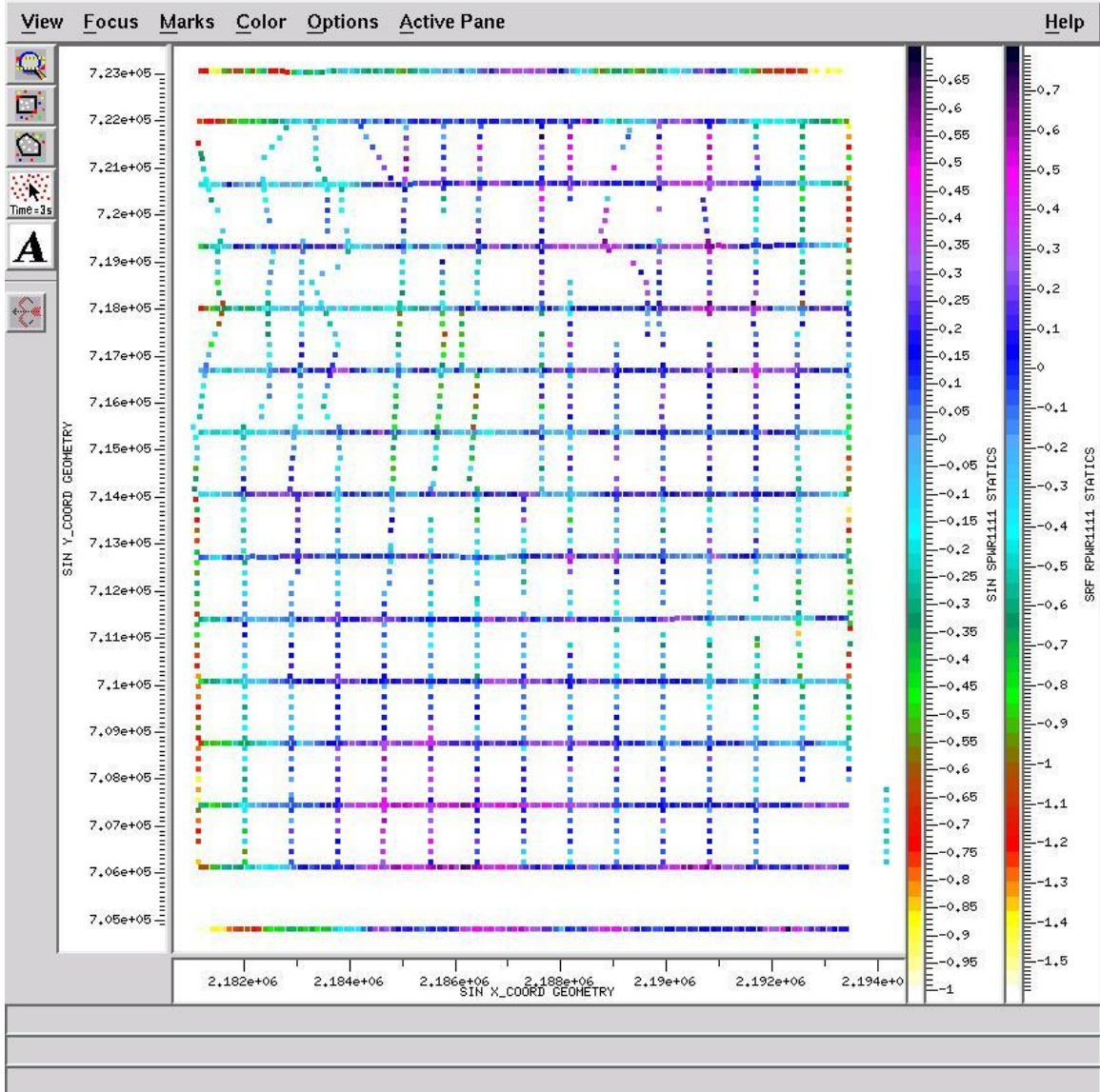
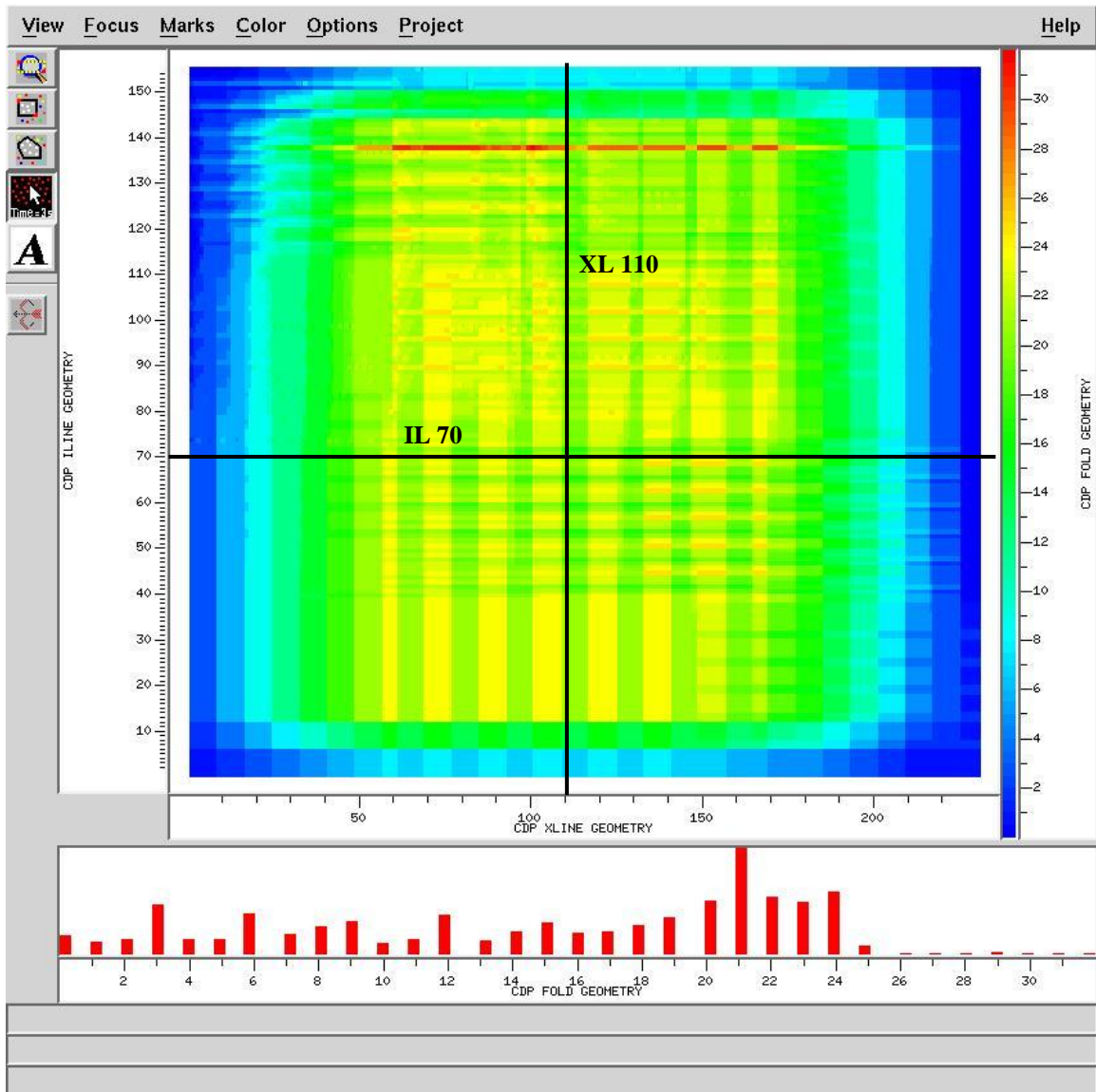


Figure A9: First Residual Statics Map



**Figure A10: Second Residual Statics Map**



**Figure A11: Location of IL 70 and XL 110**

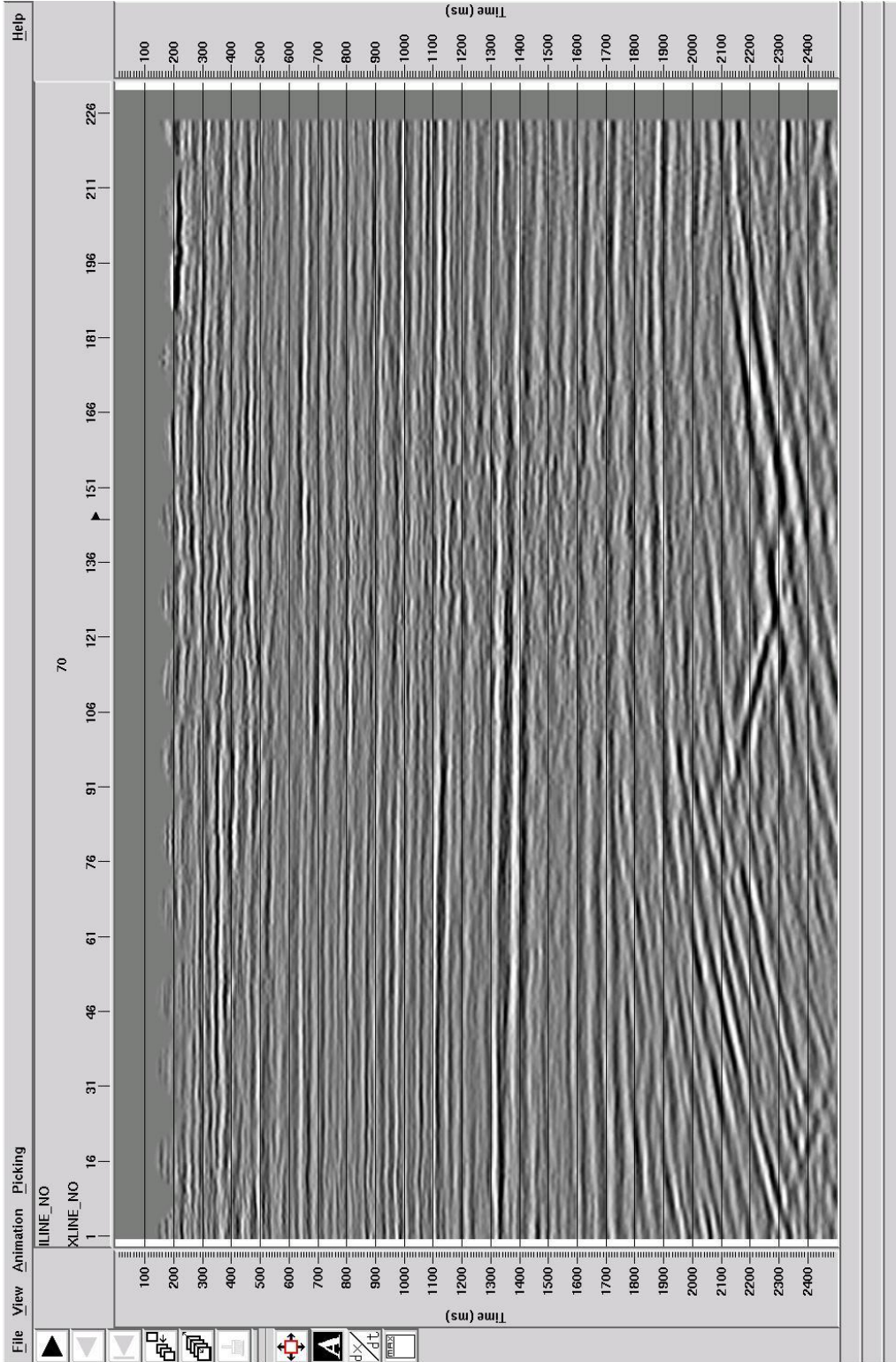


**Figure A12: Brute Stack with Elevation Statics – IL 70**

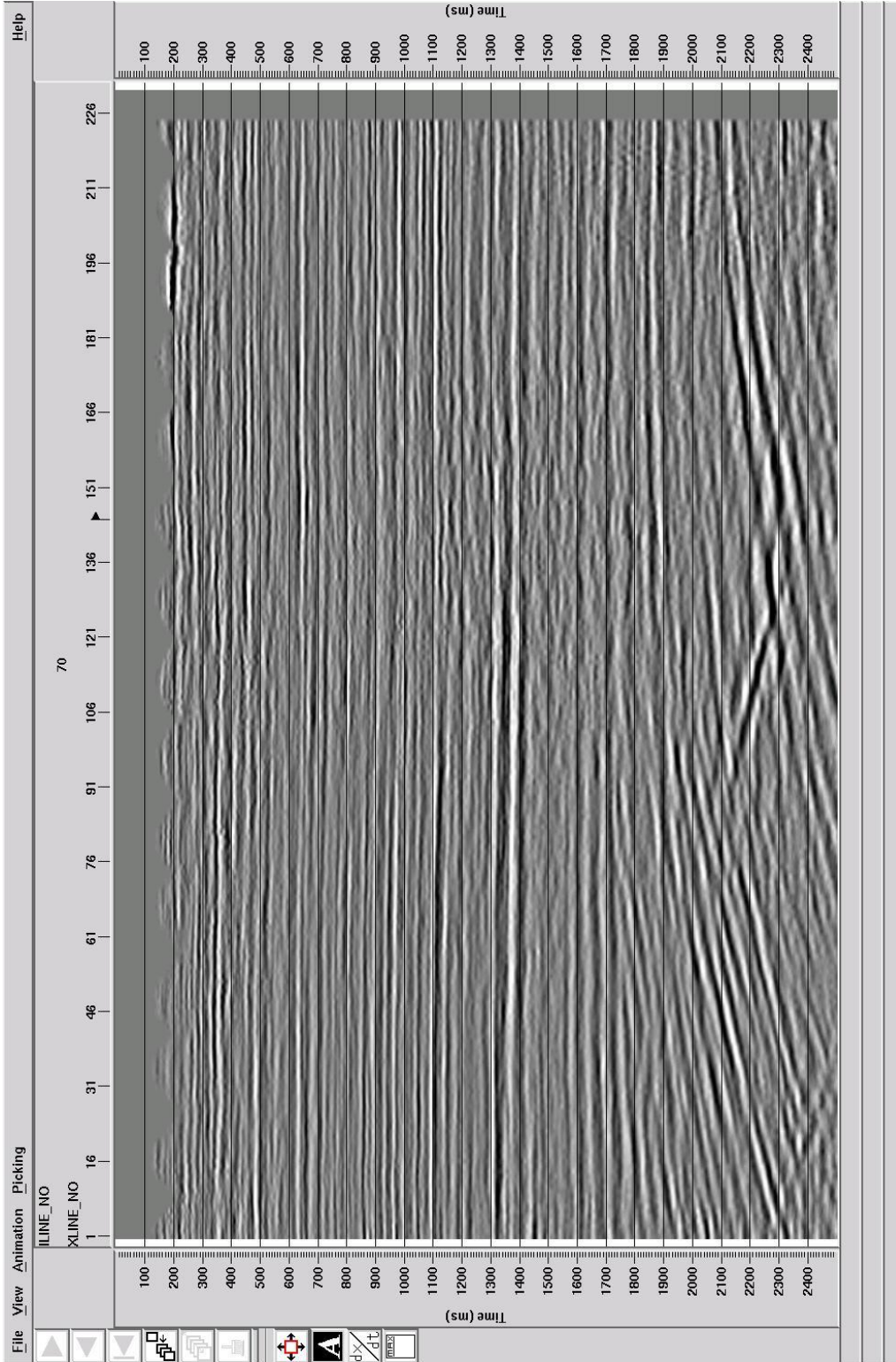


**Figure A13: Brute Stack with Refraction Statics – IL 70**

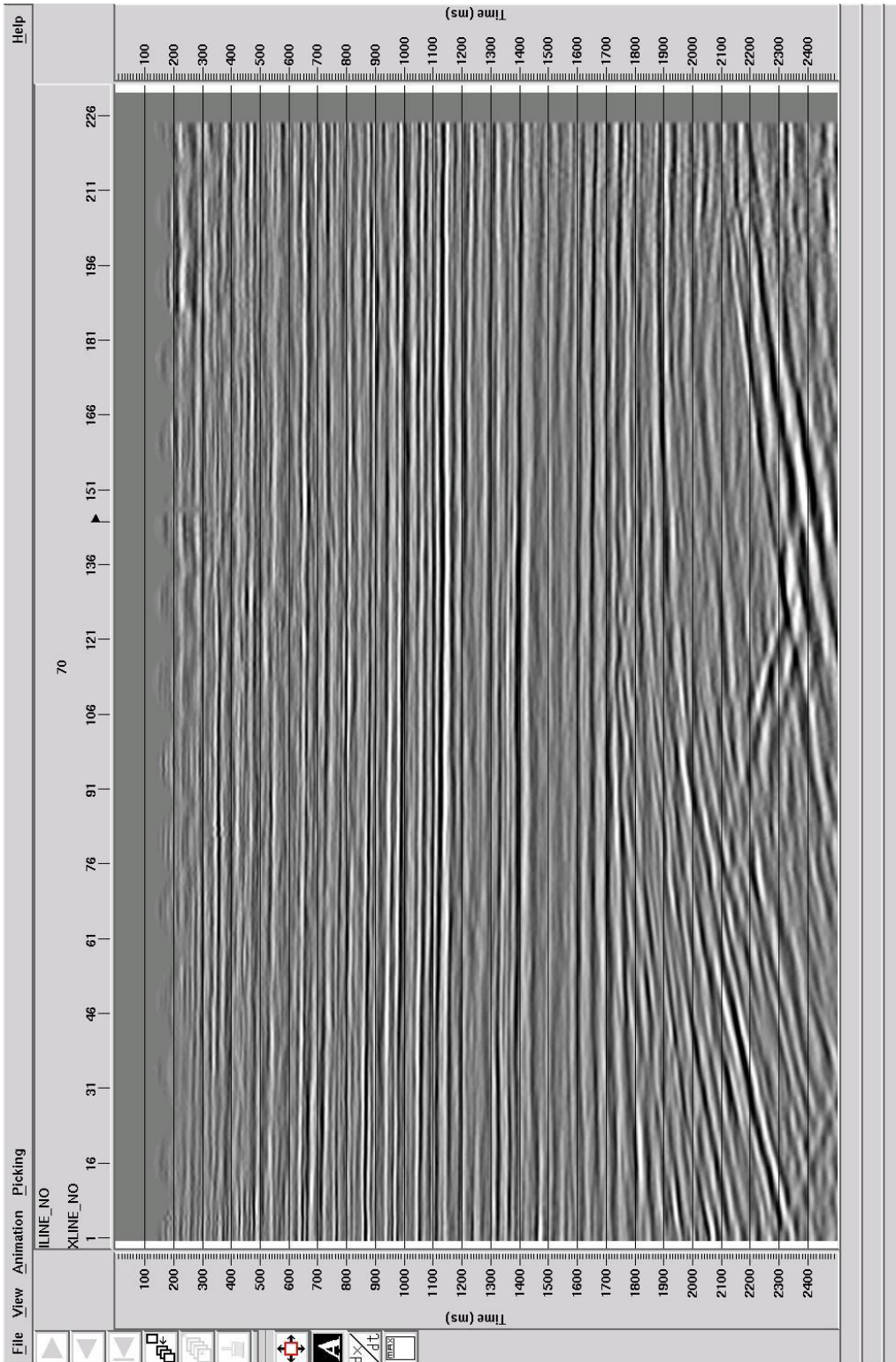


**Figure A14: Stack with First Velocity Analysis and Residual Statics – IL 70**

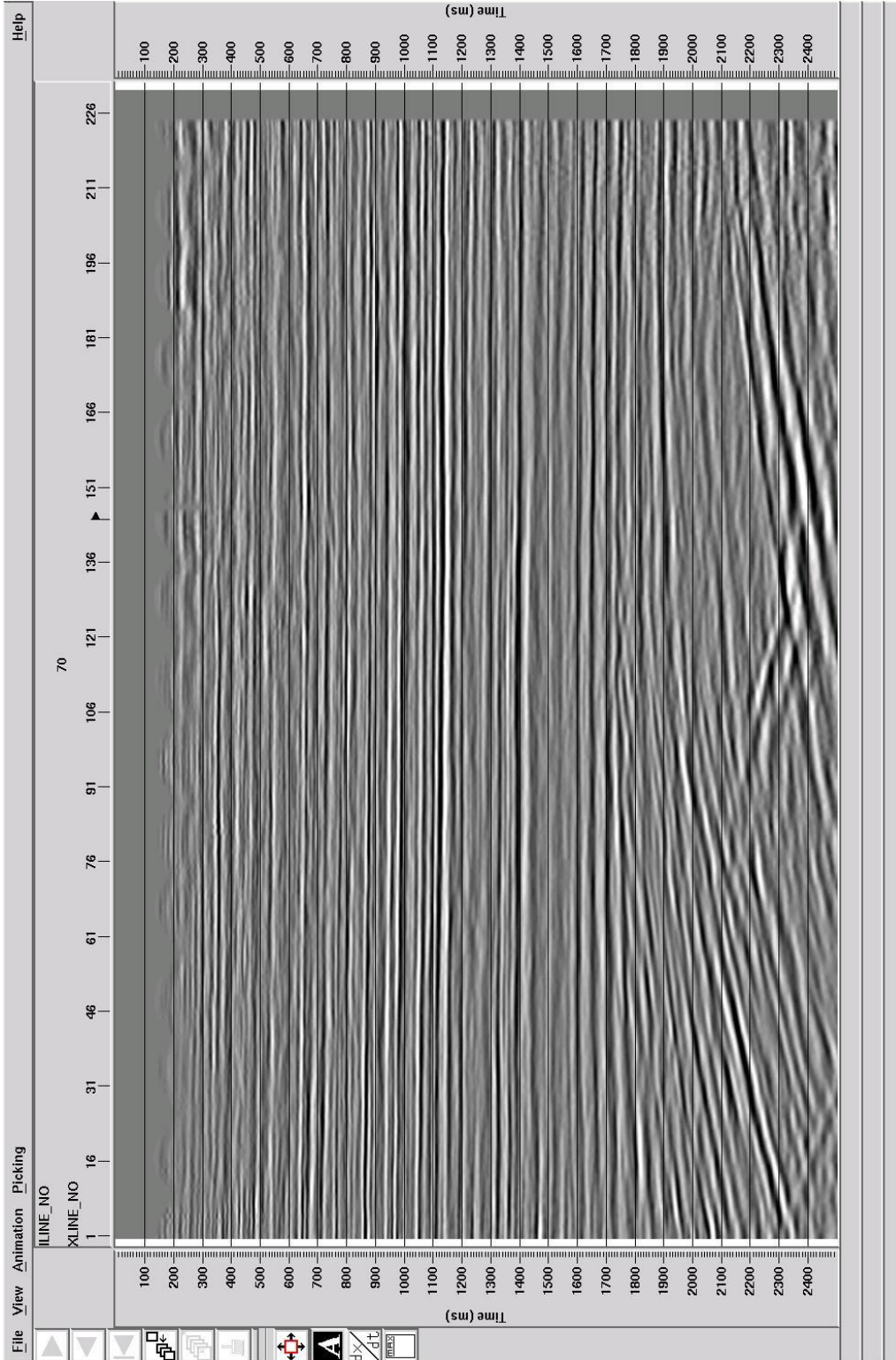


**Figure A15: Stack with Second Velocity Analysis and Residual Statics – IL 70**

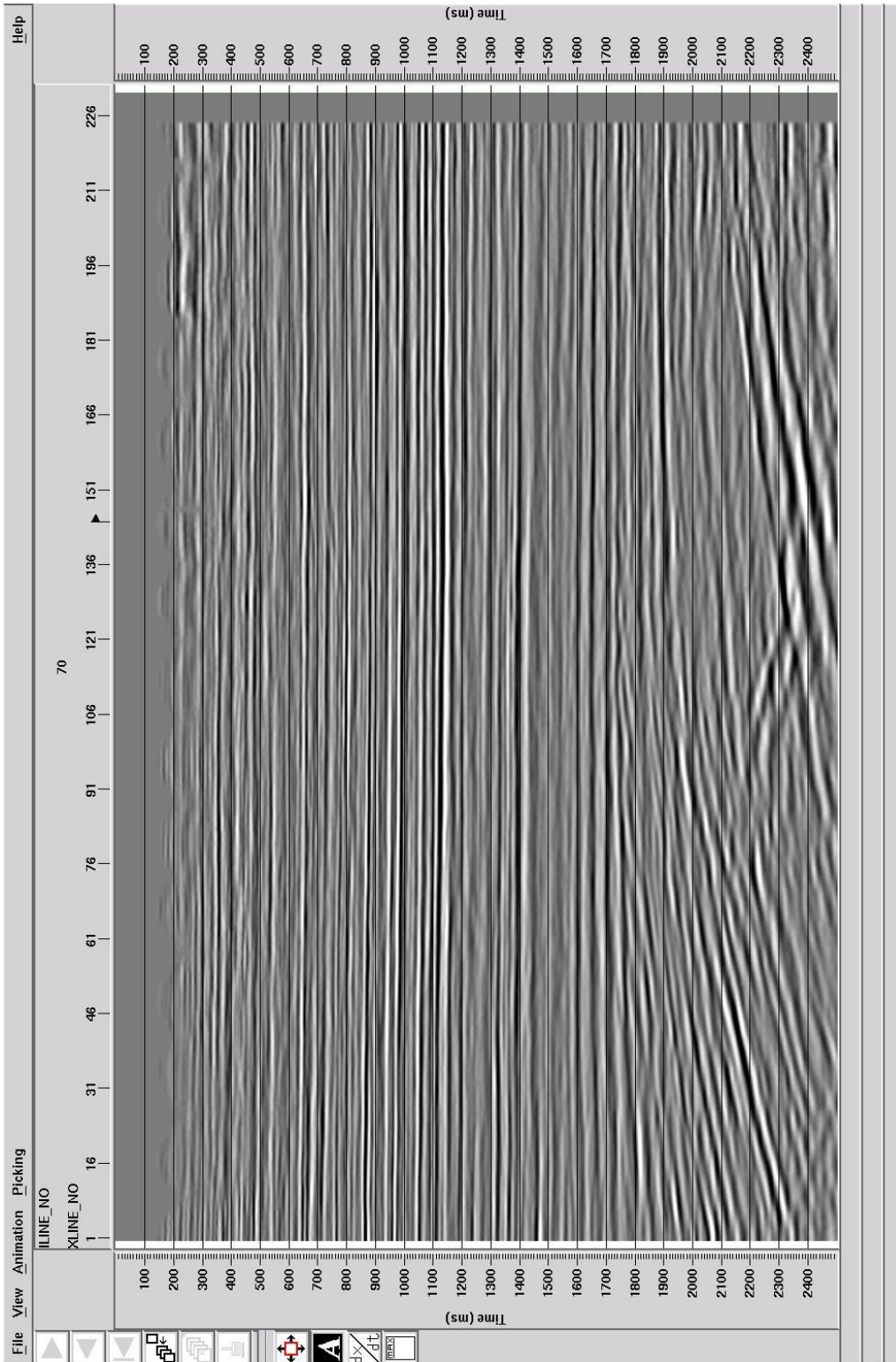


**Figure A16: Final Stack – IL 70**

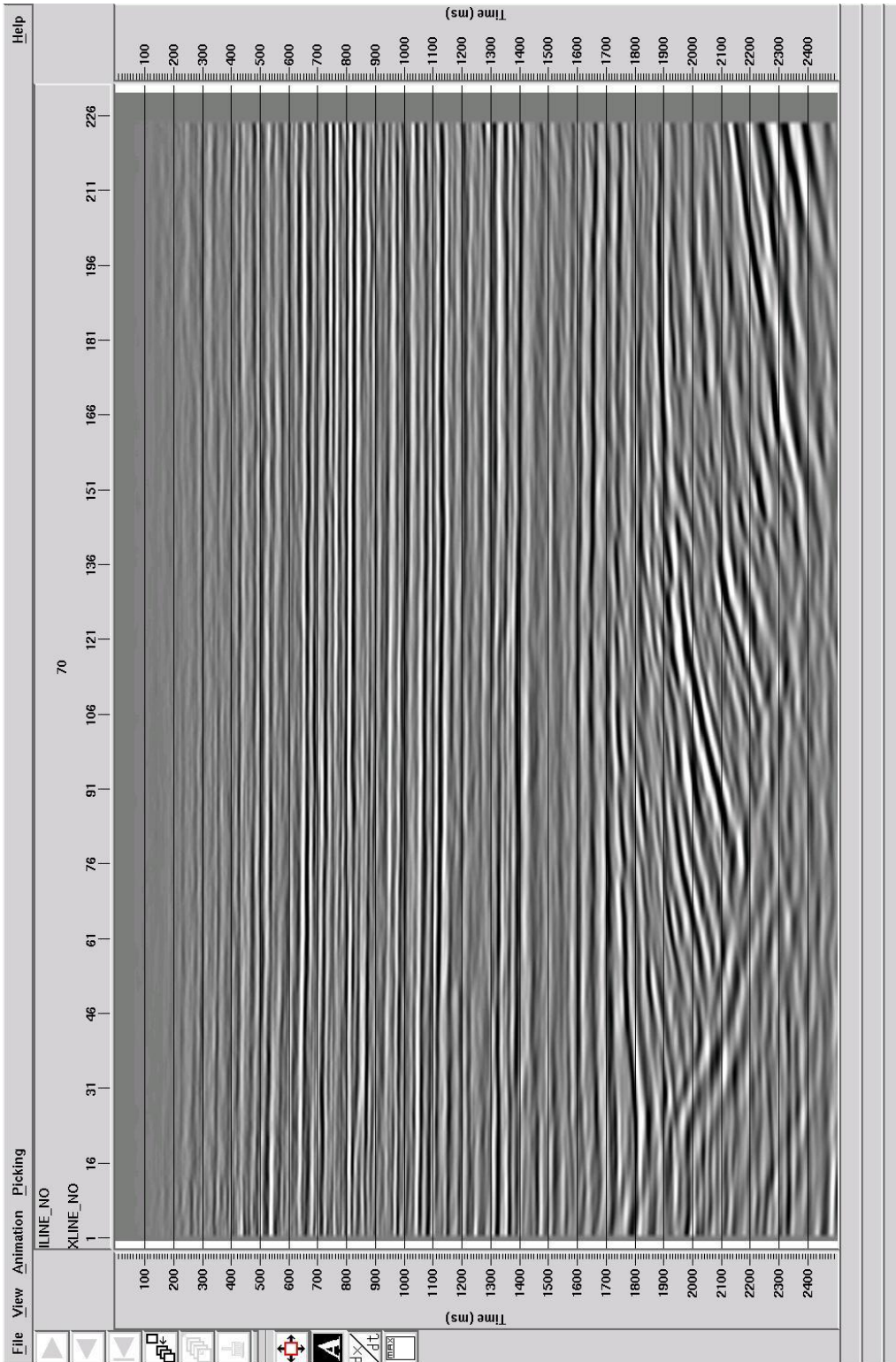


**Figure A17: Post-stack Migration – IL 70**

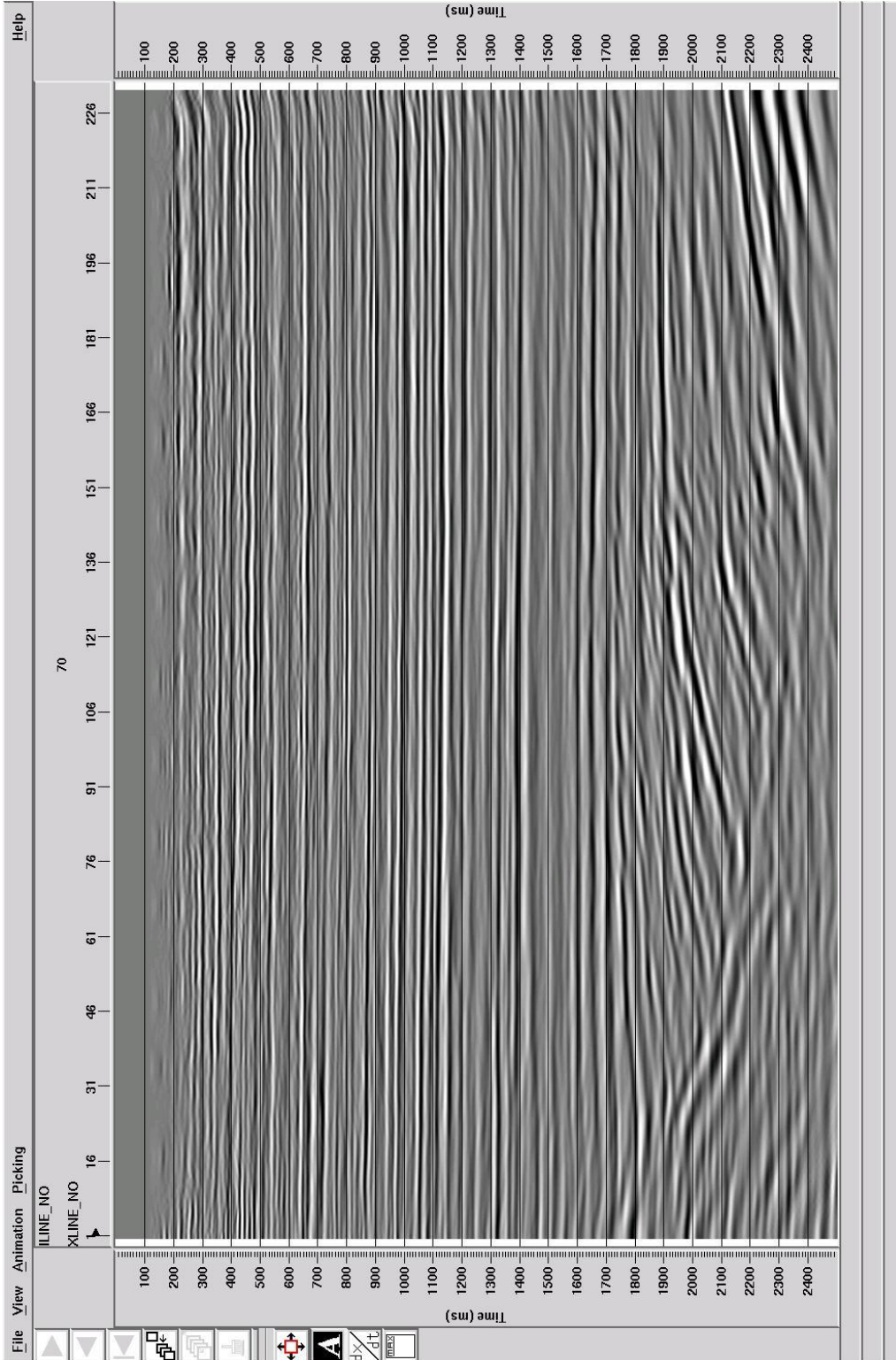


**Figure A18: PSTM Stack – IL 70**

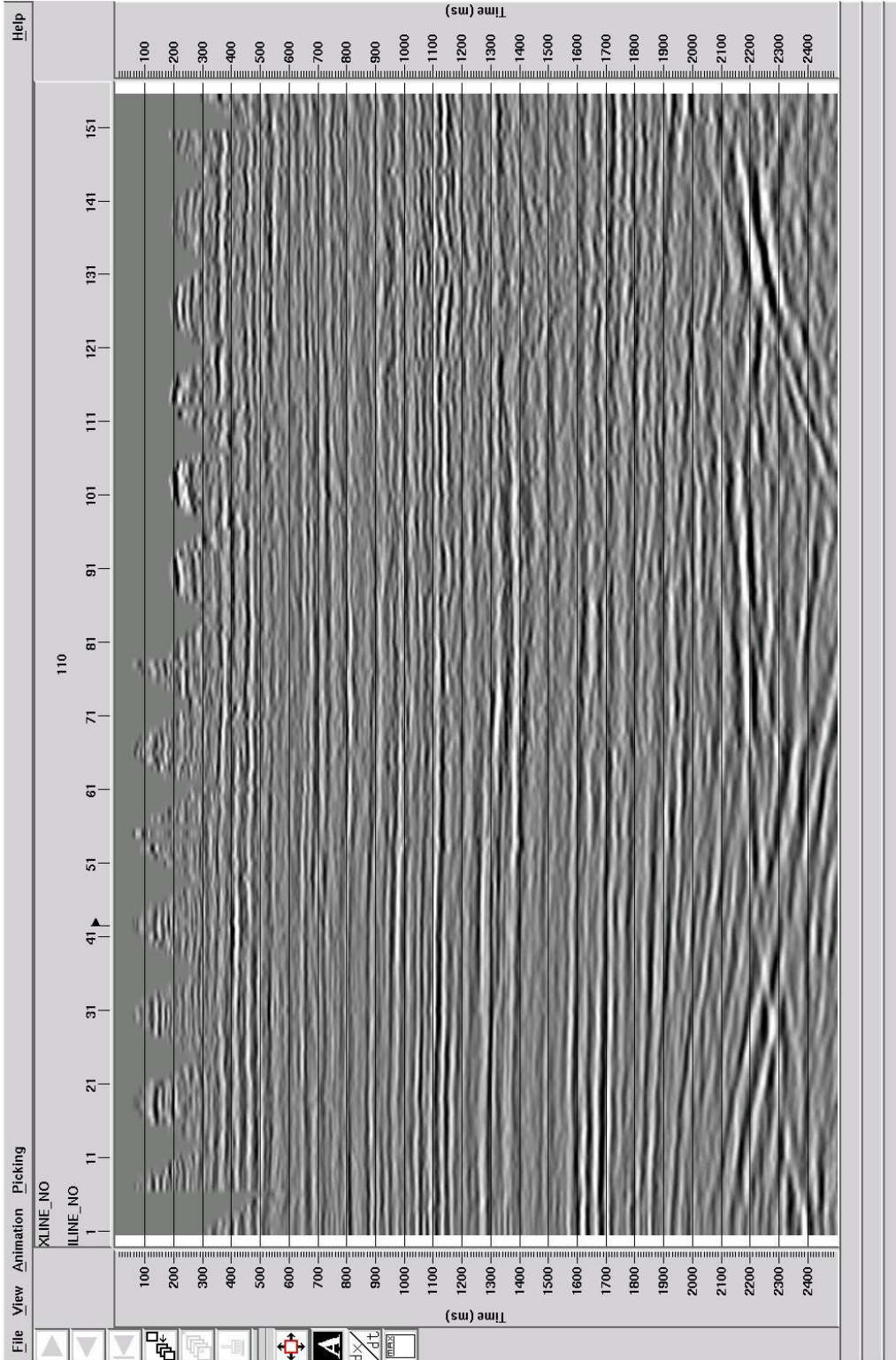


**Figure A19: Brute Stack with Elevation Statics – XL 110**

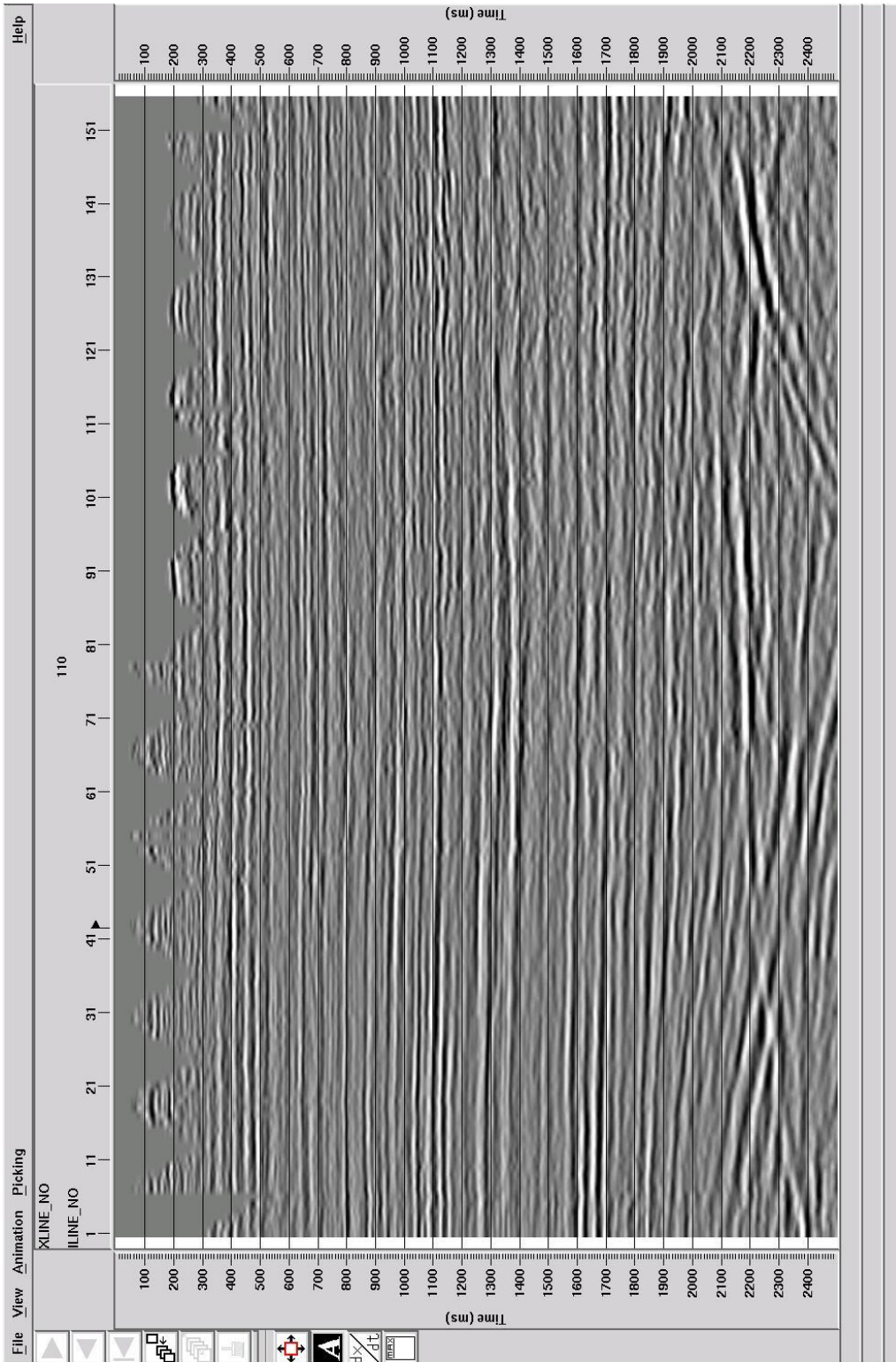


**Figure A20: Brute Stack with Refraction Statics – XL 110**

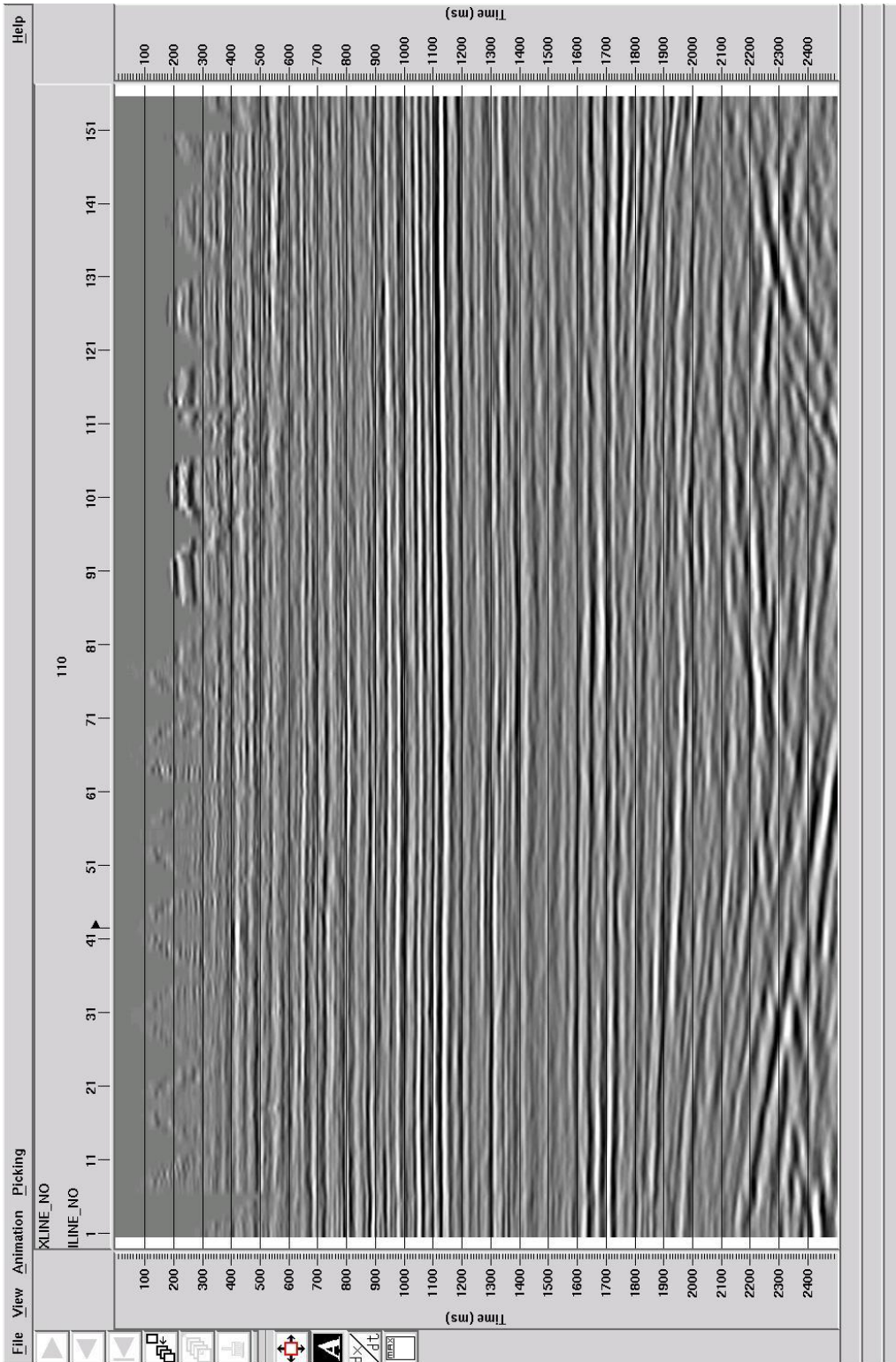


**Figure A21: Stack with First Velocity Analysis and Residual Statics – XL 110**

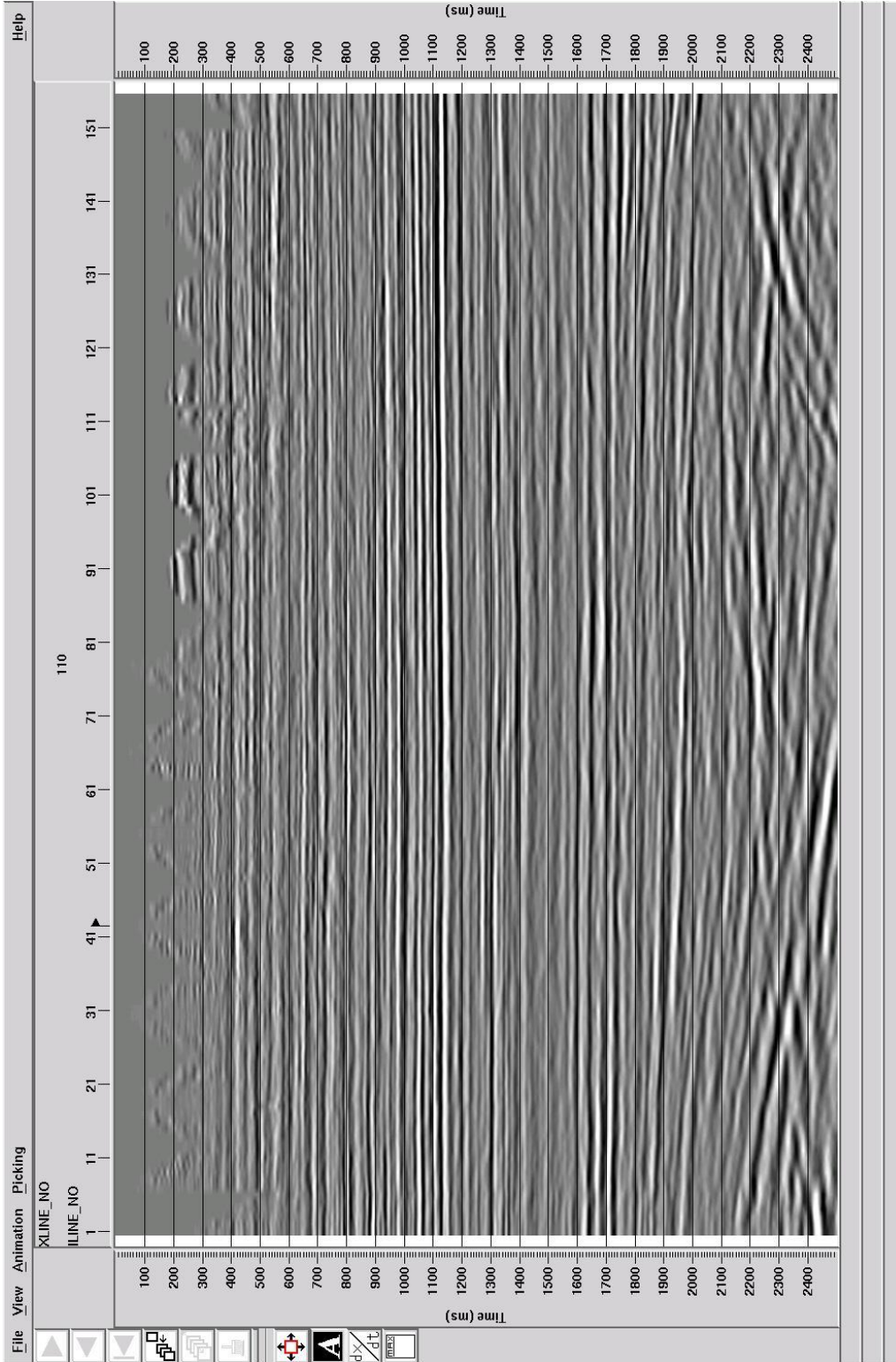


**Figure A22: Stack with Second Velocity Analysis and Residual Statics – XL 110**

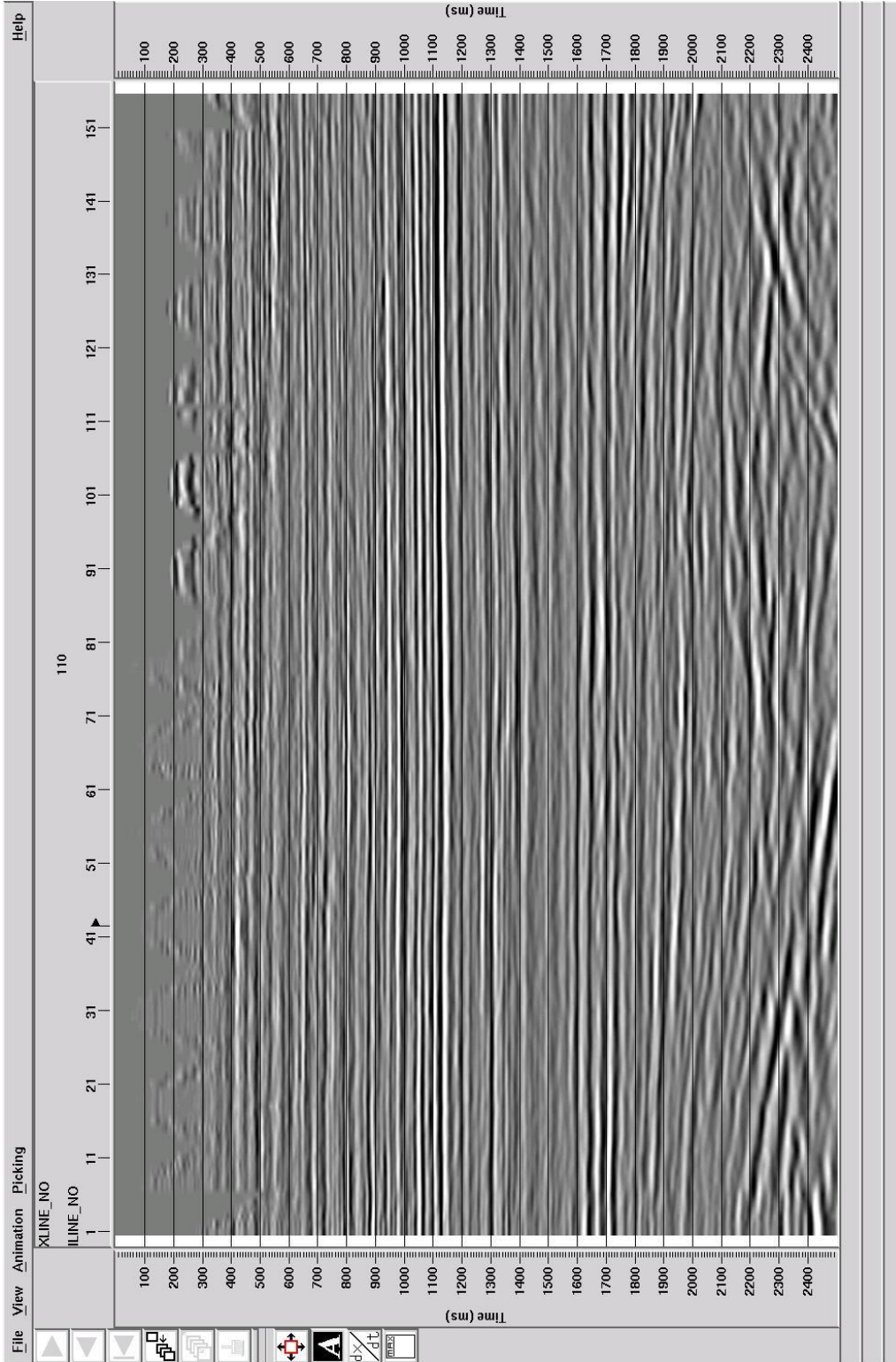


**Figure A23: Final Stack – XL 110**

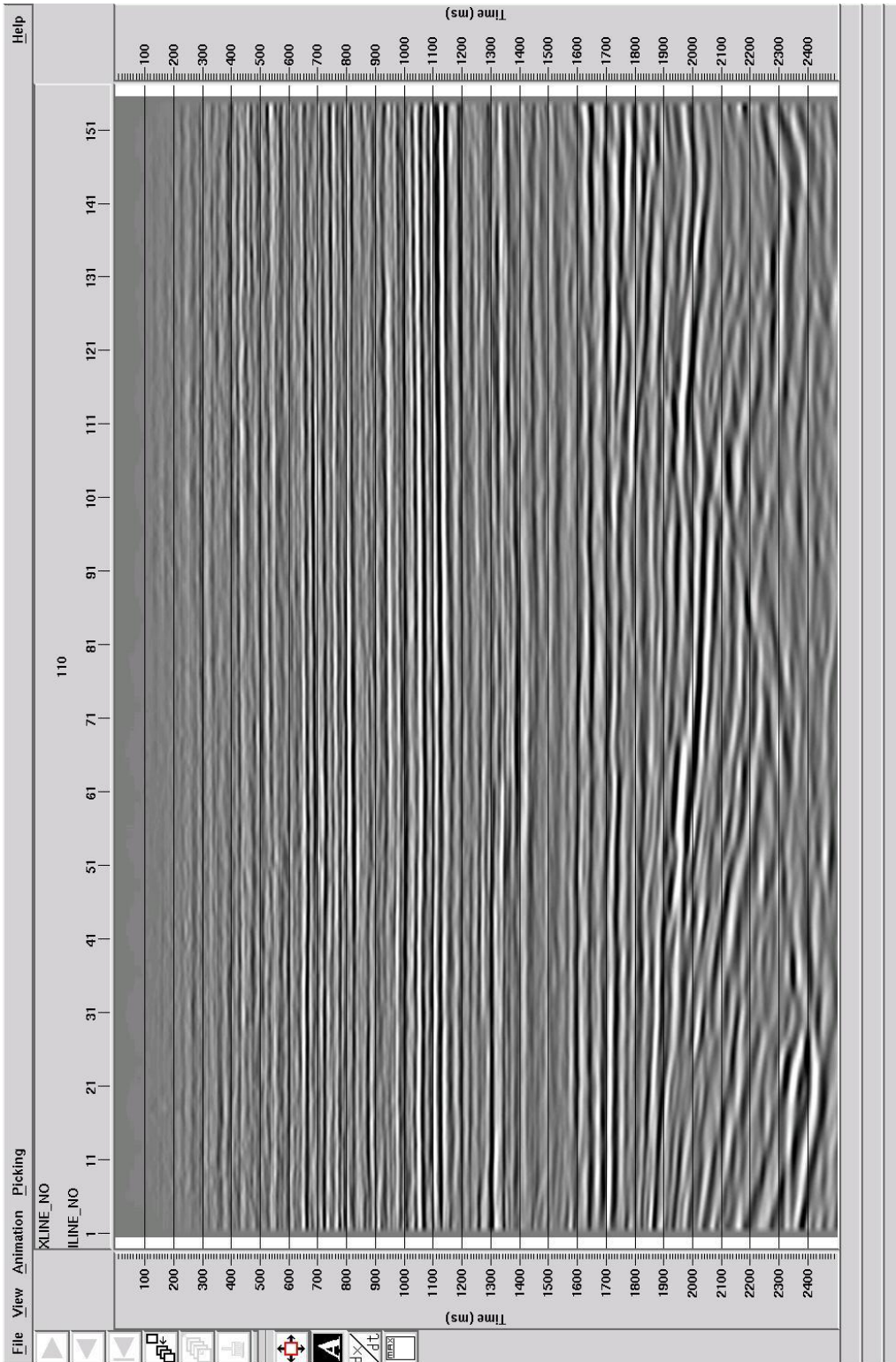


**Figure A24: Post-stack Migration – XL 110**

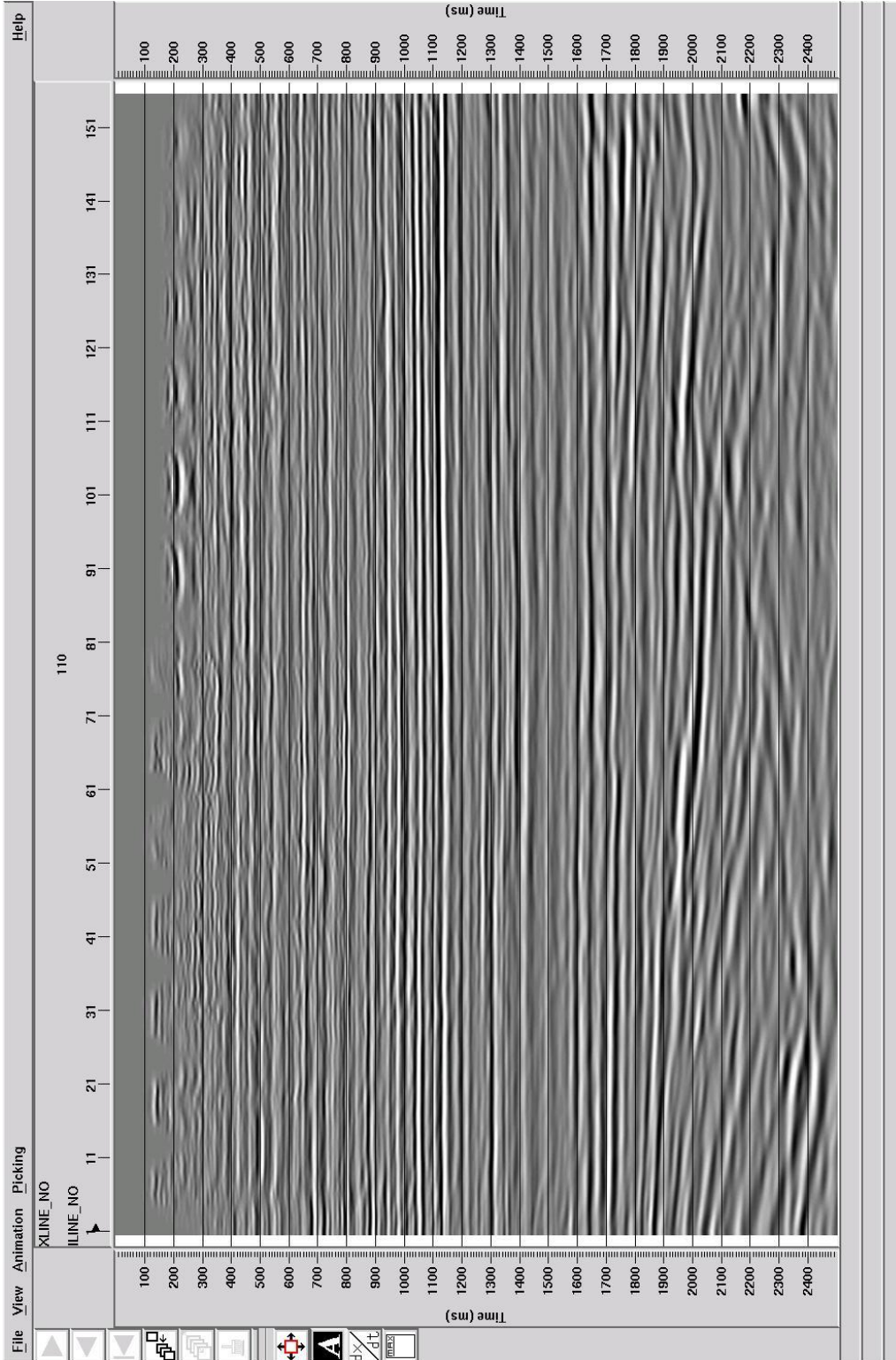


**Figure A25: PSTM Stack – XL 110**

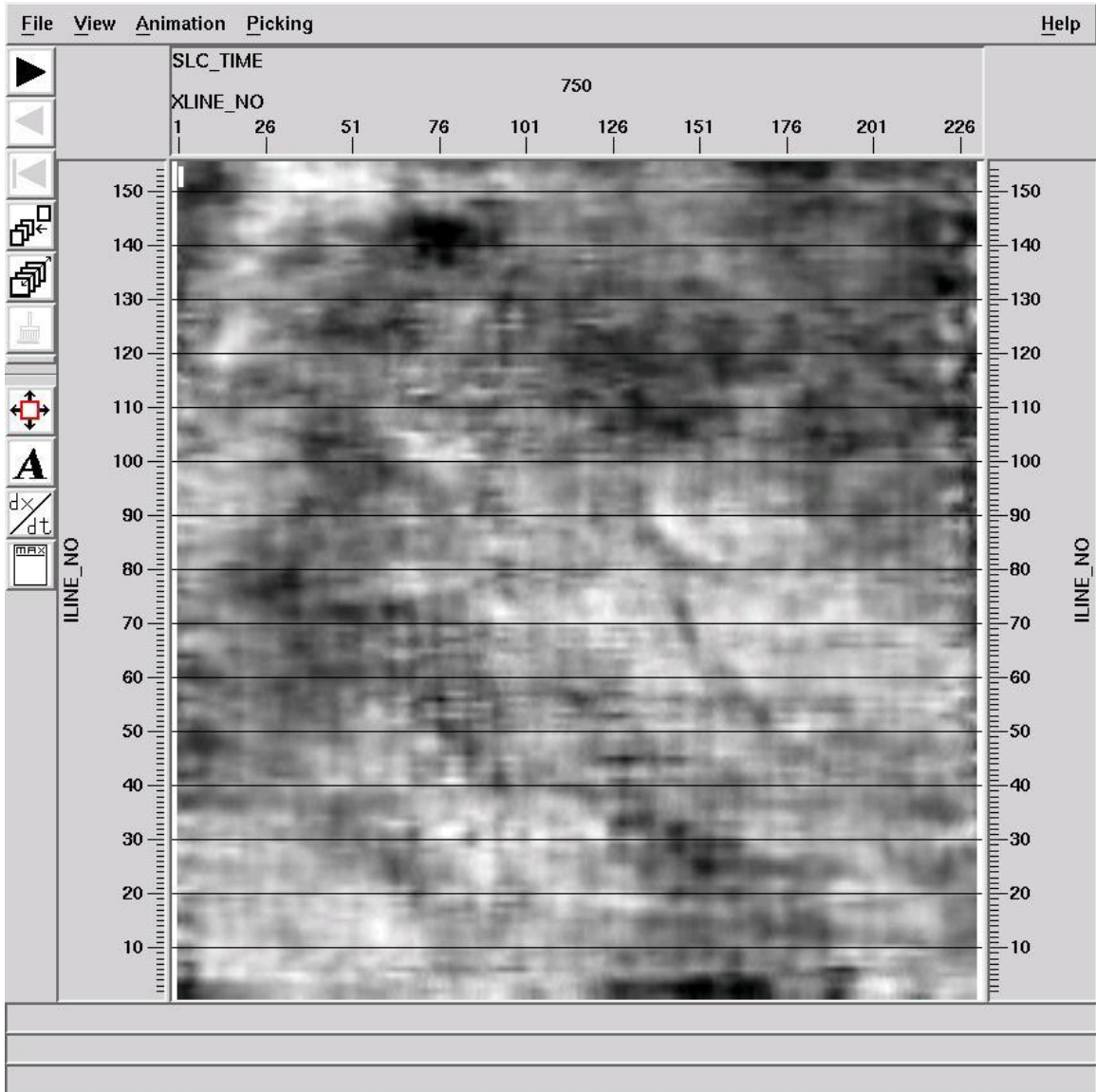


**Figure A26: PSTM stack - Time Slice 750 ms**

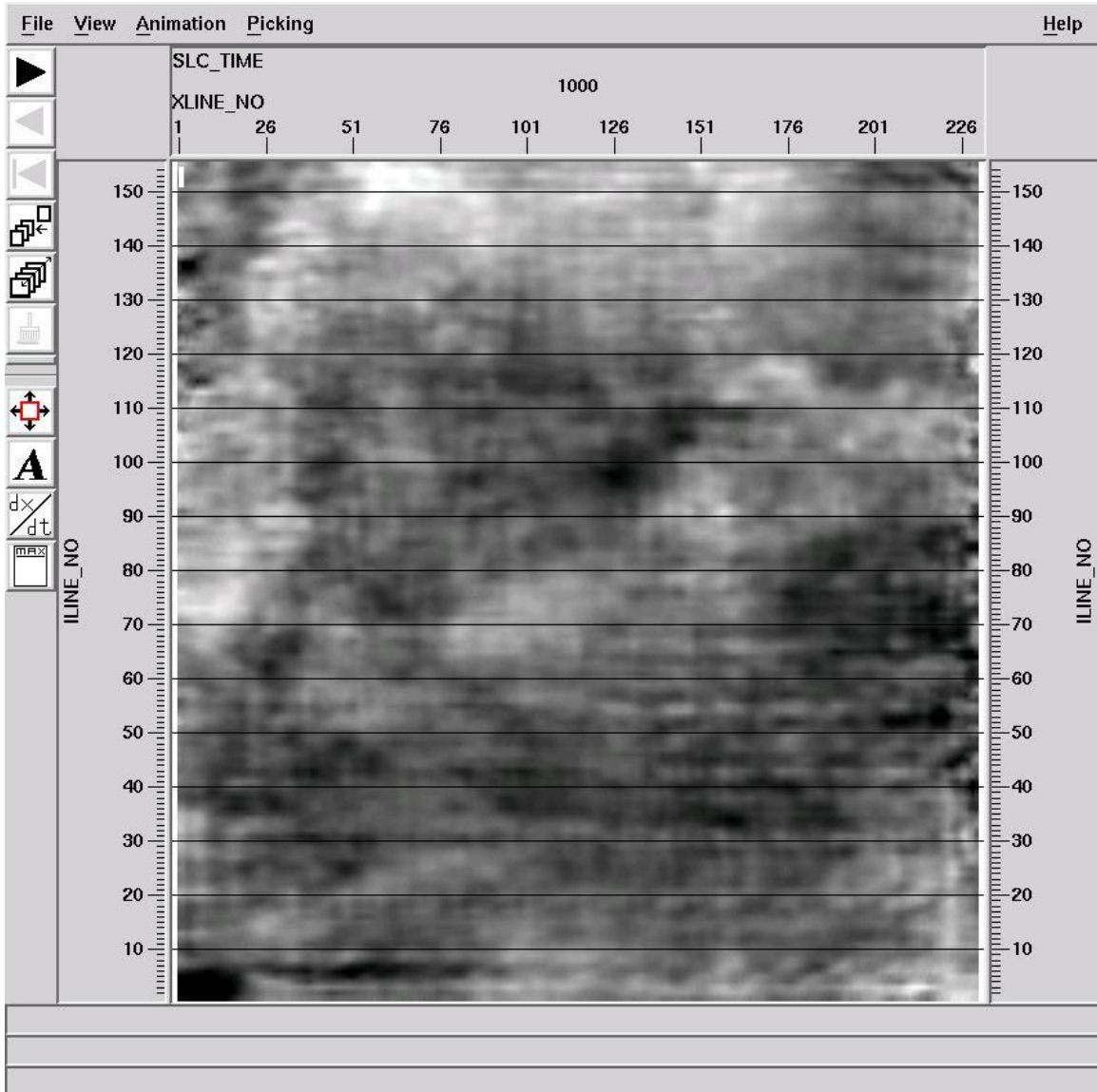


**Figure A27: PSTM stack - Time Slice 1000 ms**

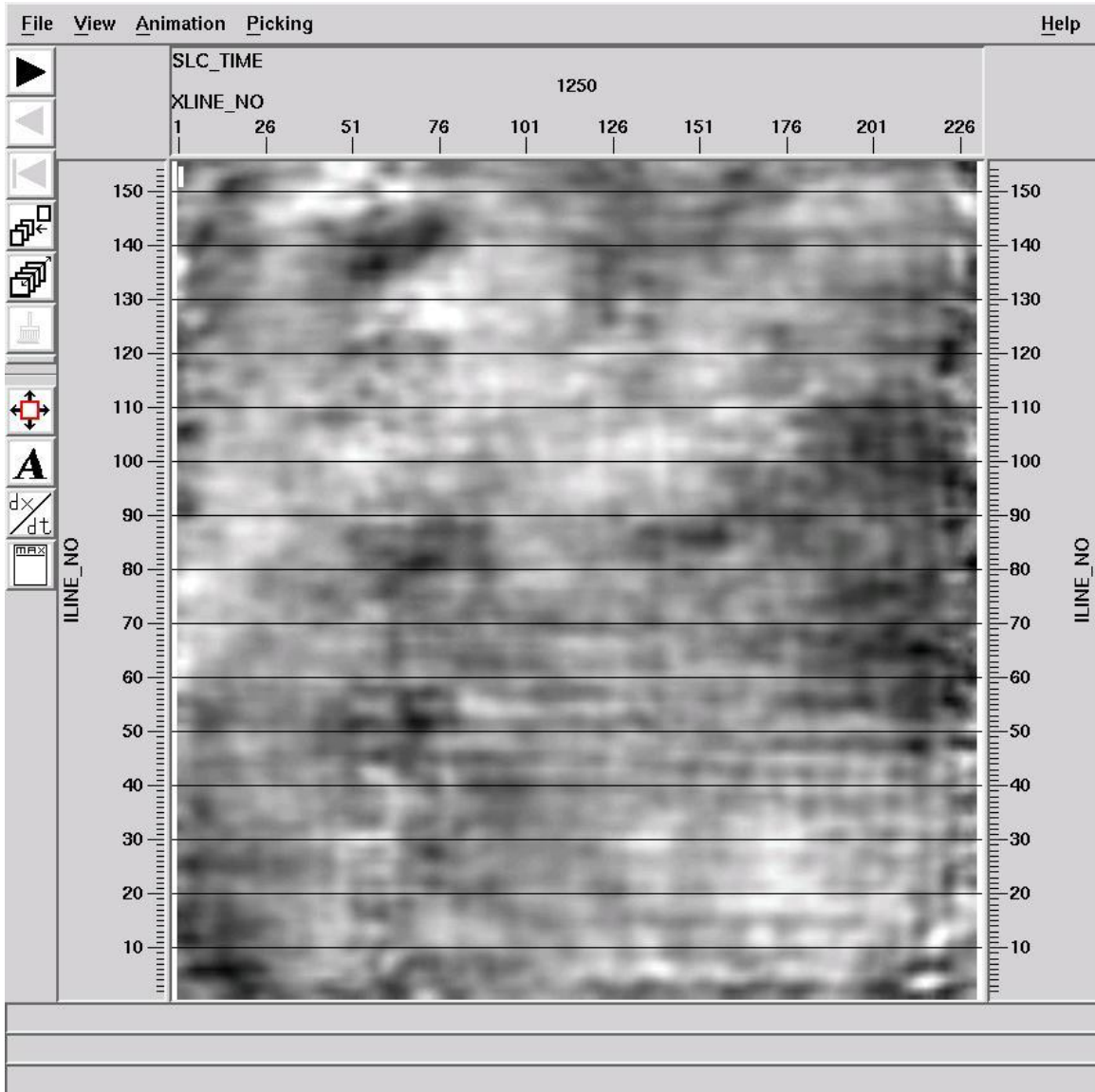


**Figure A28: PSTM stack - Time Slice 1250 ms**

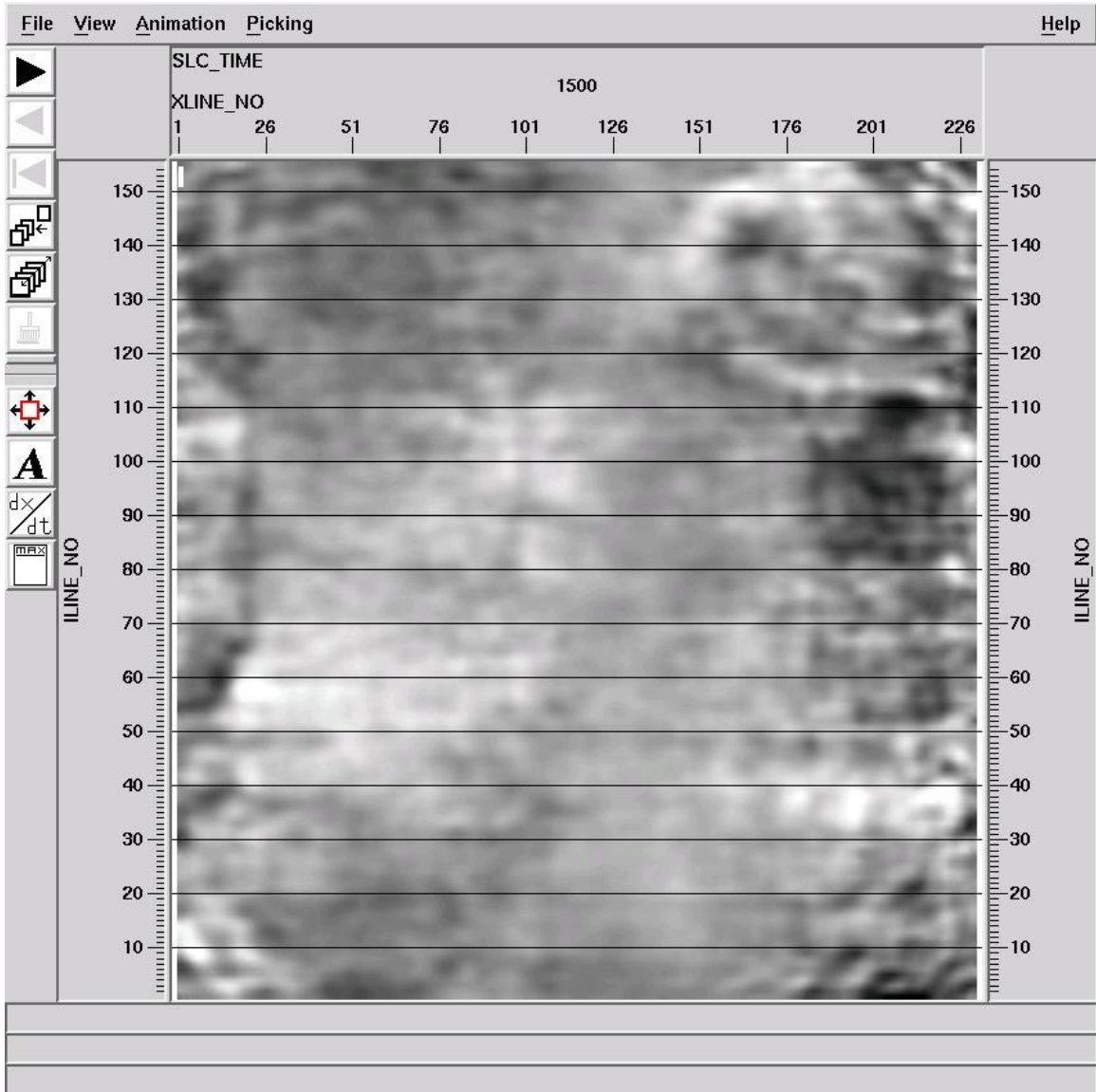


**Figure A29: PSTM stack - Time Slice 1500 ms**

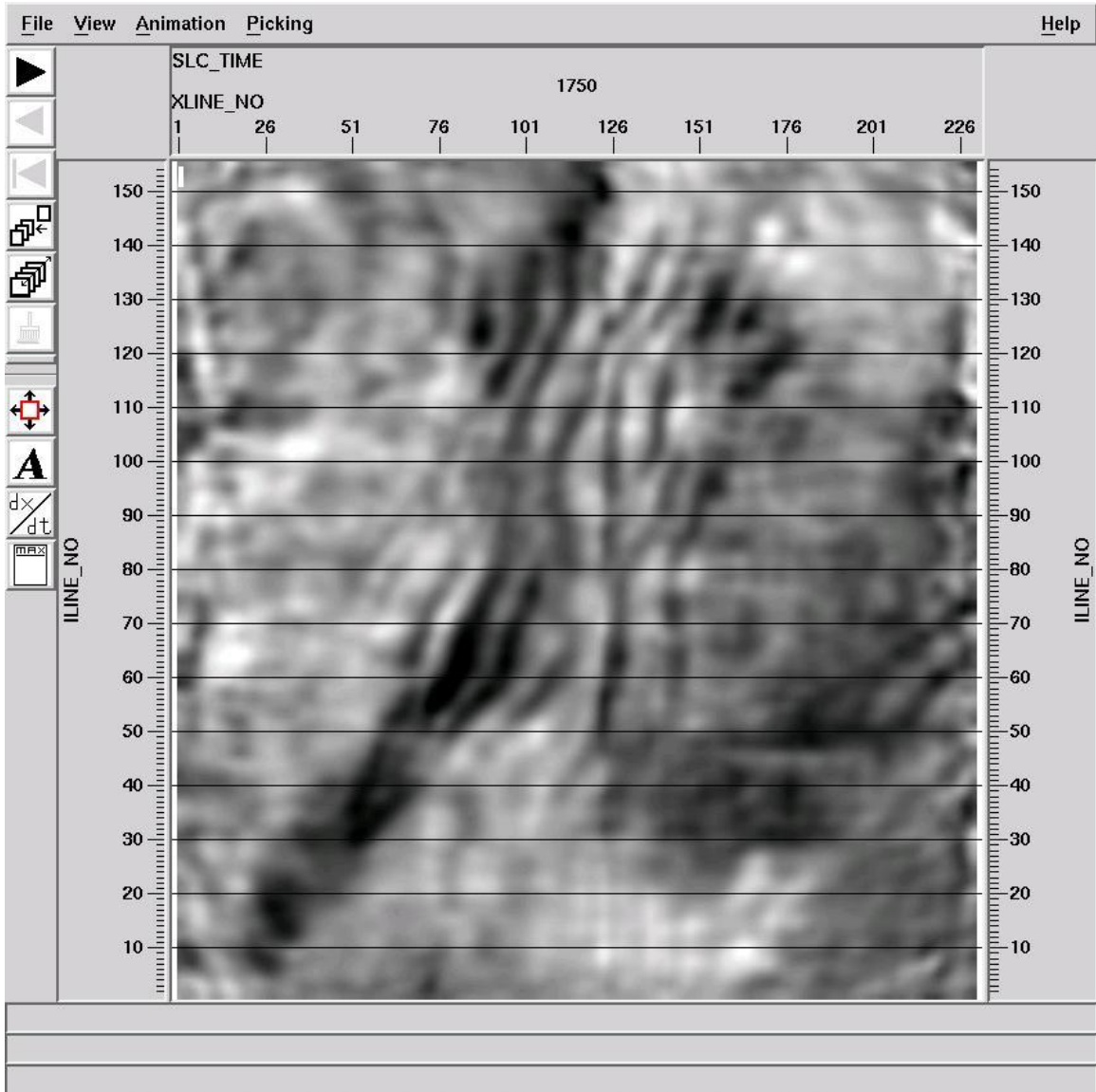


Figure A30: PSTM stack - Time Slice 1750 ms

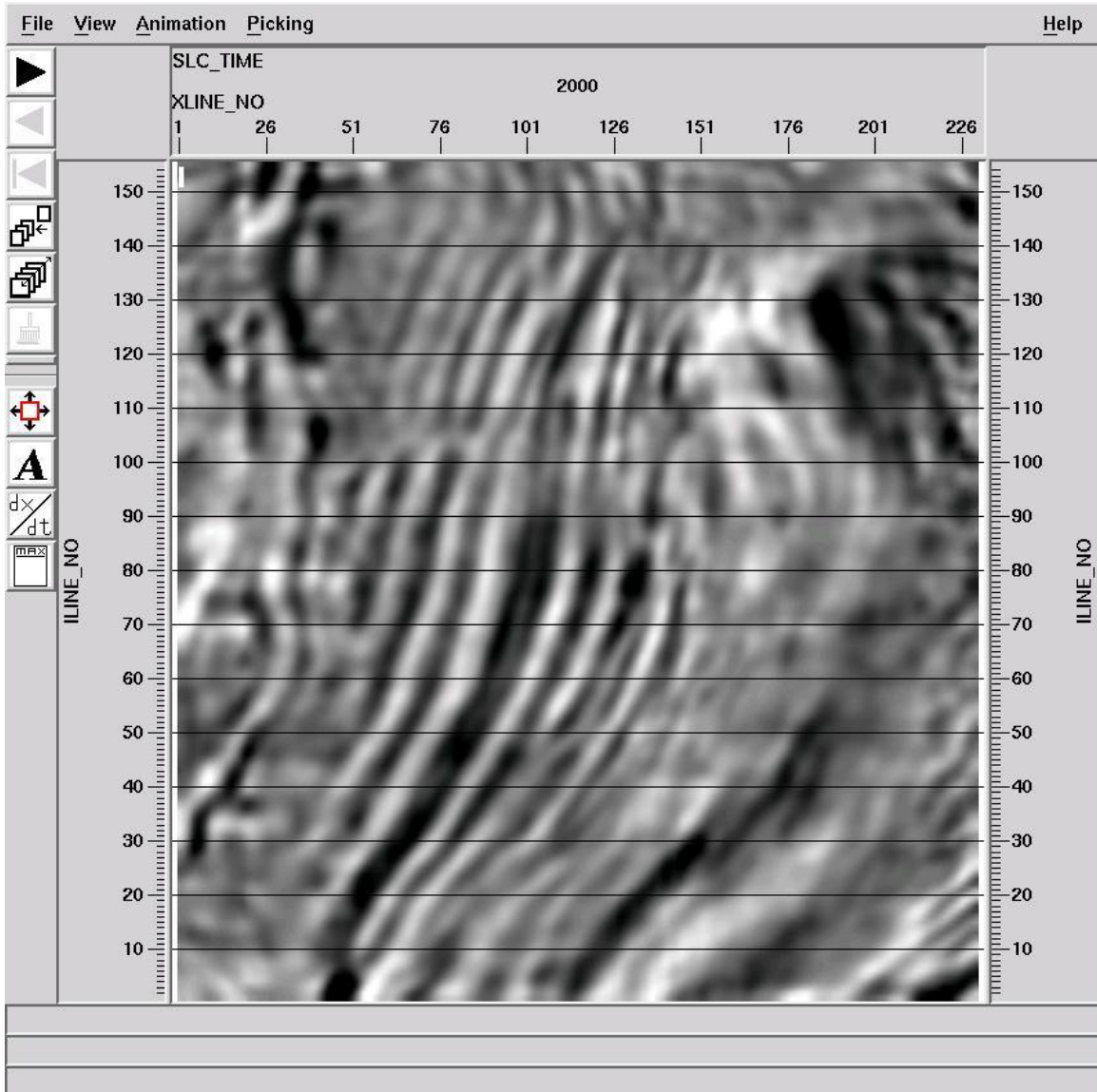


Figure A31: PSTM stack - Time Slice 2000 ms

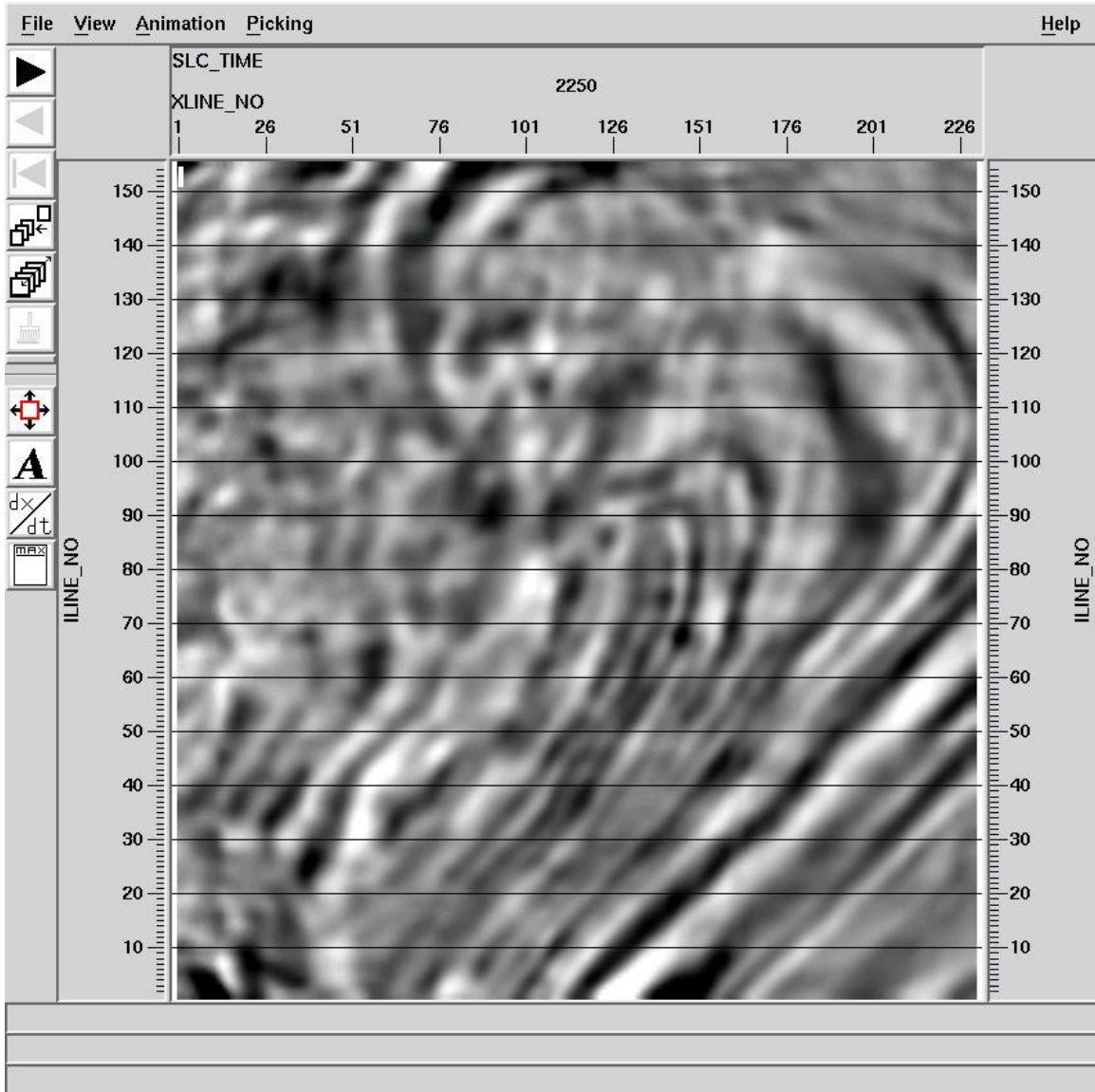


Figure A32: PSTM stack - Time Slice 2250 ms

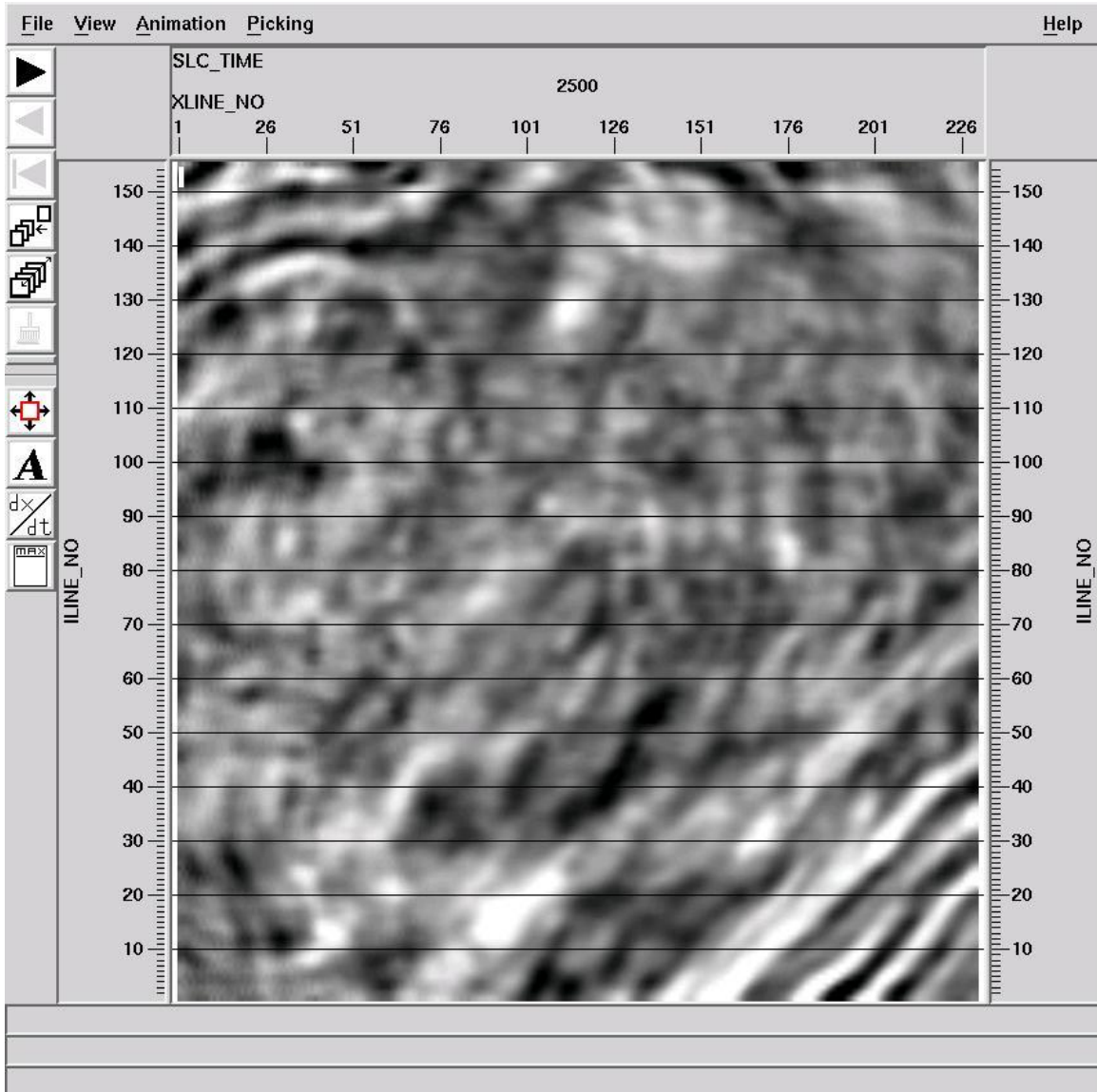


Figure A33: PSTM stack - Time Slice 2500 ms

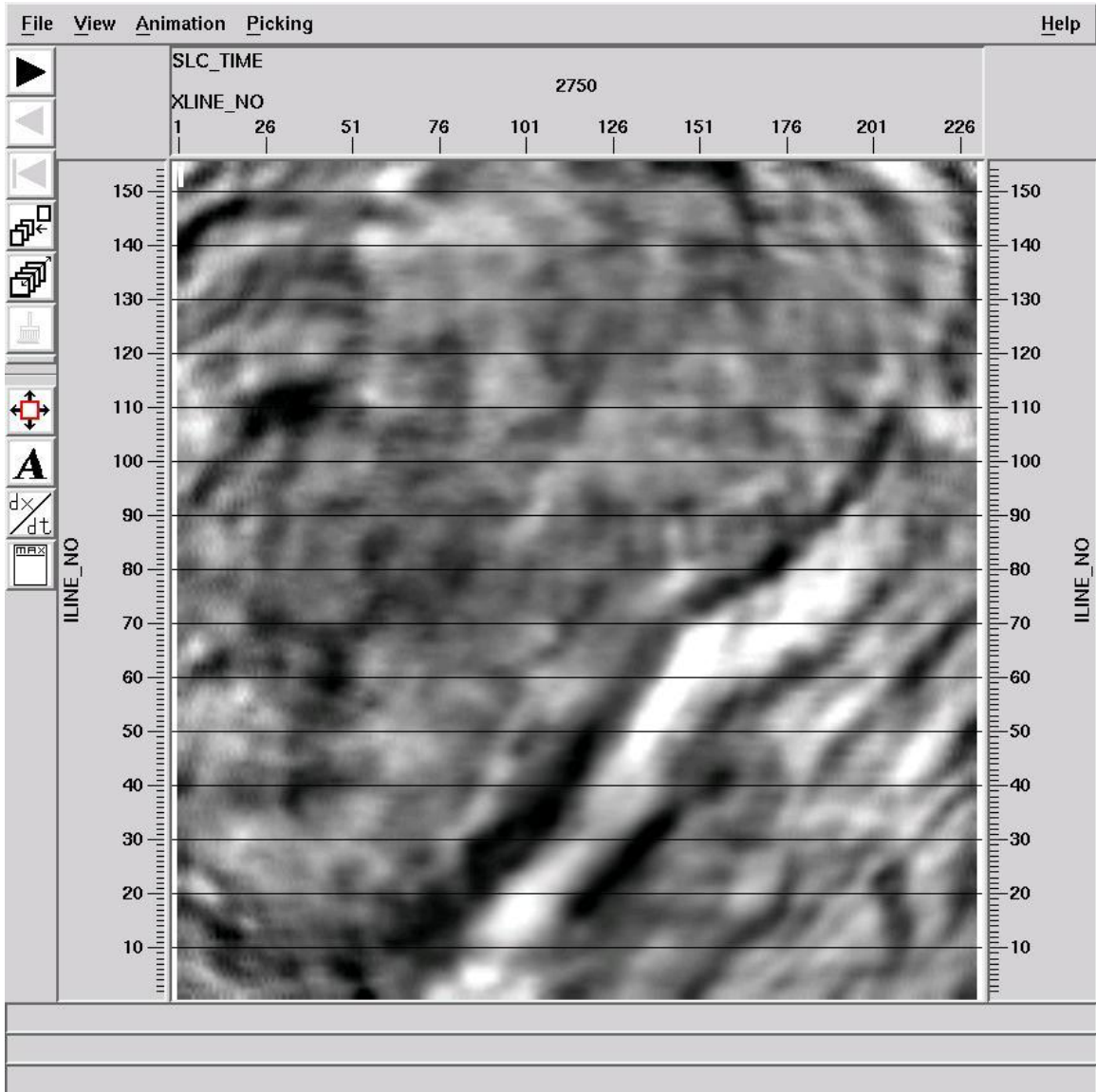
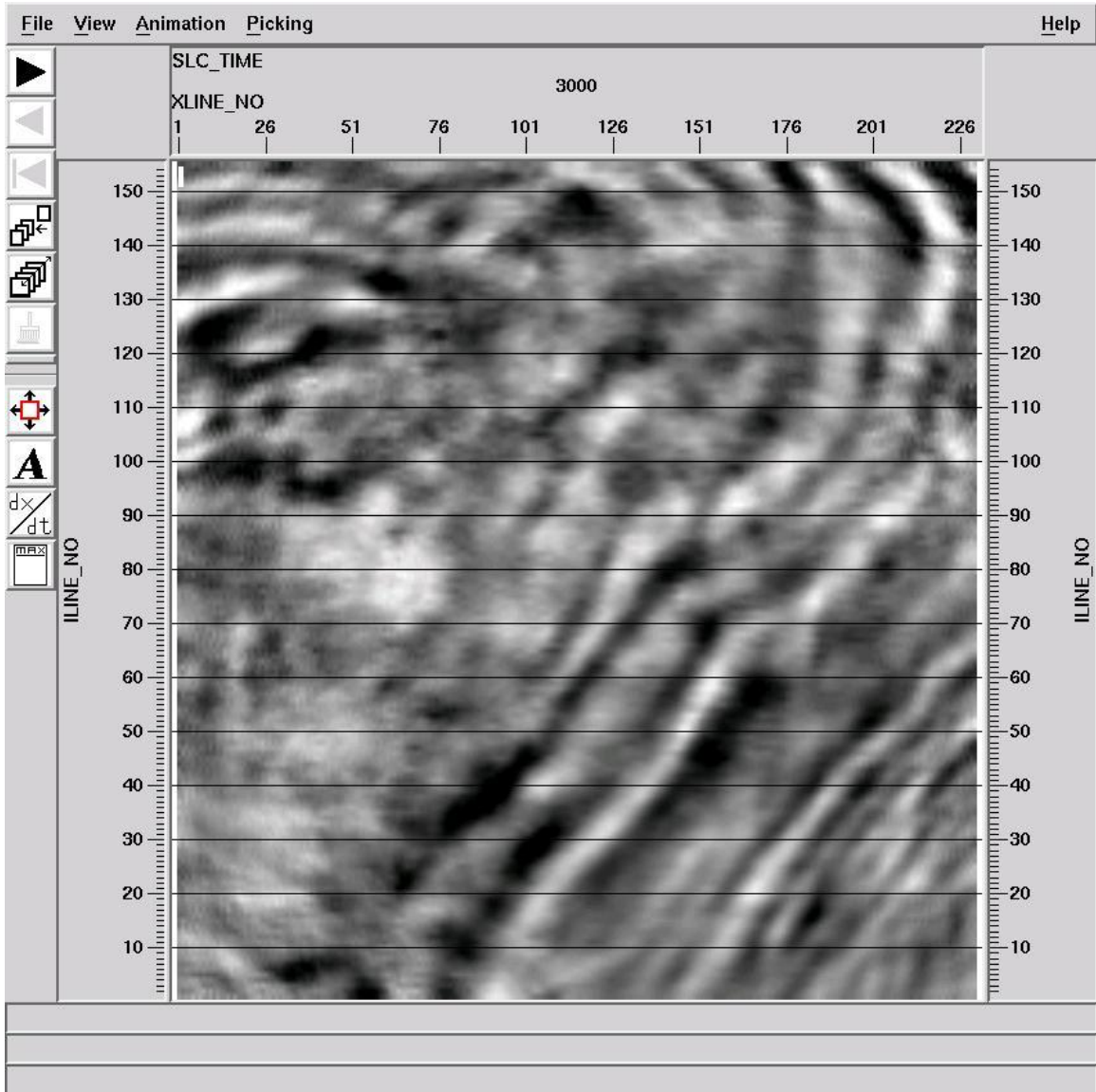


Figure A34: PSTM stack - Time Slice 2750 ms



**Figure A35: PSTM stack - Time Slice 3000 ms**

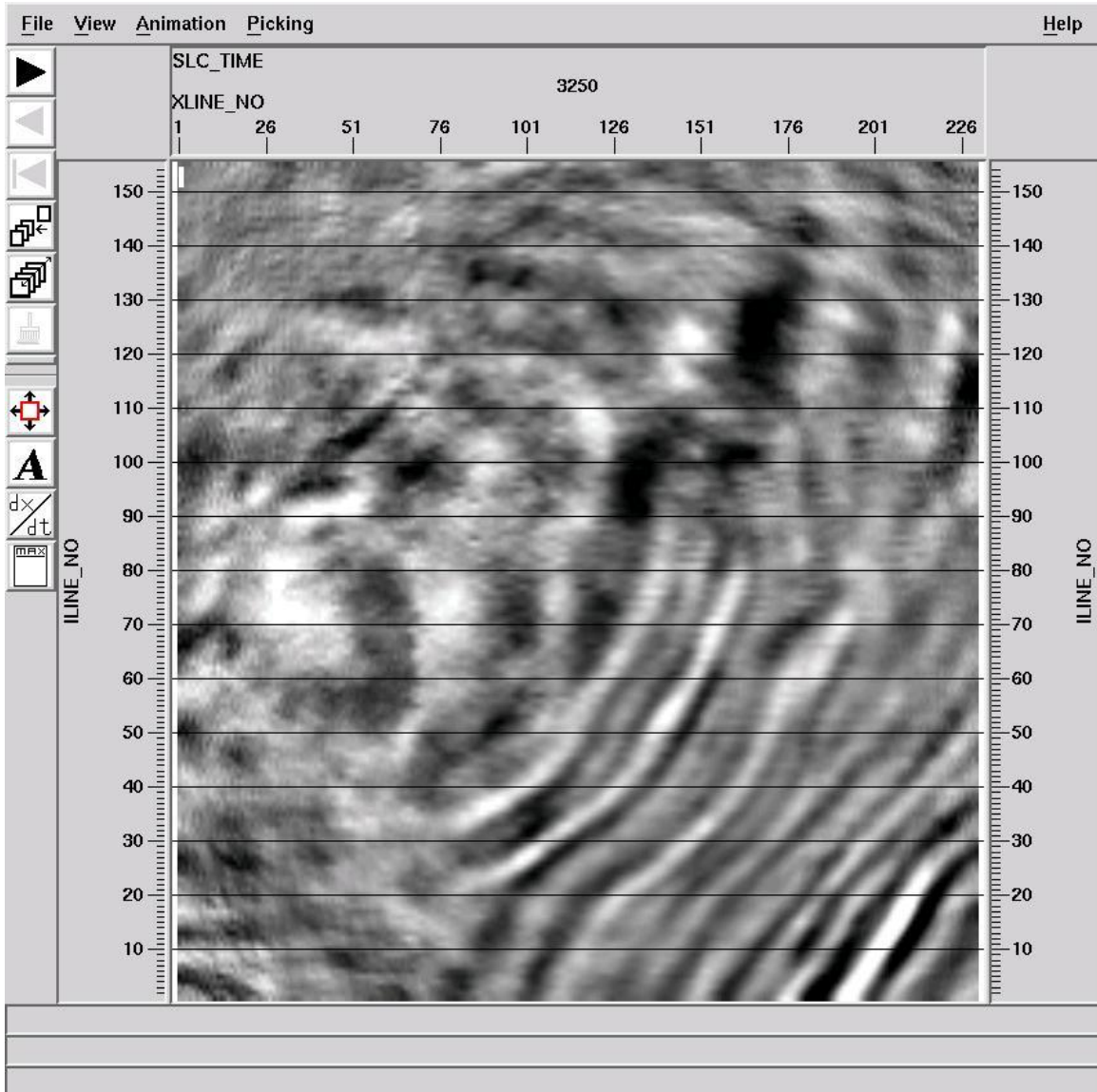


Figure A36: PSTM stack - Time Slice 3250 ms

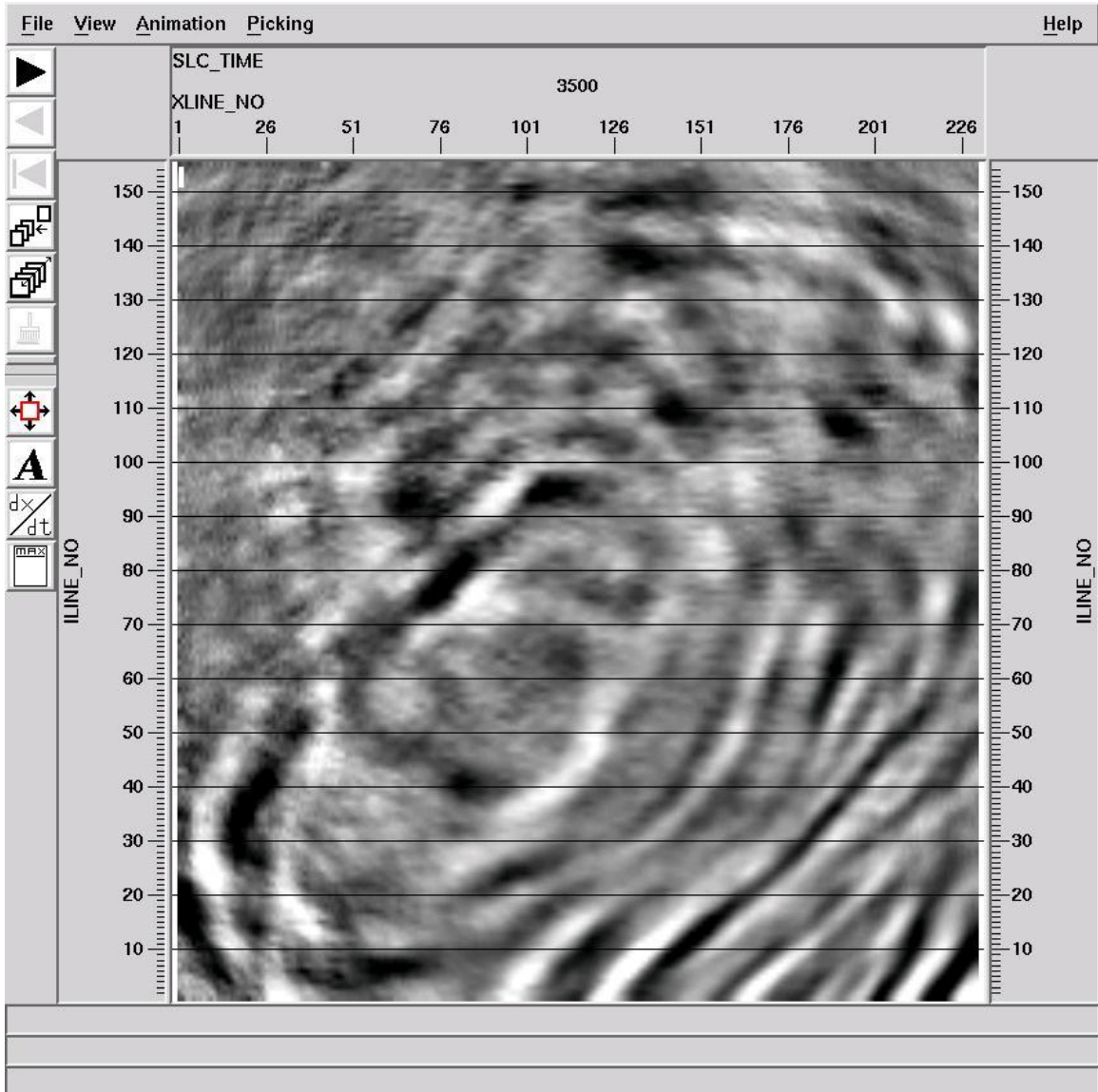


Figure A37: PSTM stack - Time Slice 3500 ms

## REFERENCES

- Berkovitch, A., Belfer, I., Hassin, Y., Landa, E., 2009, Diffraction imaging by multifocusing: *Geophysics*, 74, 6, WCA75-WCA81.
- Claerbout, J. F., 1971, Toward a unified theory of reflector mapping: *Geophysics*, 36, 467-481.
- El-Mowafy, H., and Marfurt, K. J., 2006, Integration of 3-D seismic attributes and sequence stratigraphy in interpreting the middle Frio Formation fluvial architecture. Case history: Stratton and Agua Dulce Fields, South Texas, USA: *SEG Expanded Abstracts*, 25, 619-623.
- El-Mowafy, H., and Marfurt, K. J., 2008, Structural interpretation of the middle Frio Formation using 3D seismic and well logs: An example from The Texas Gulf Coast of The United States: *The Leading Edge*, 27, 840-854.
- Etgen, J., Gray, S. H., and Zhang, Y., 2009, An overview of depth imaging in exploration geophysics: *Geophysics*, 74, WCA5-WCA17.
- Fomel, S., 2002, Applications of plane-wave destruction filters: *Geophysics* 67, 1946-1960.
- Galloway, W. E., Hobday, D. K., and Magara, K., 1982, Frio Formation of Texas Gulf Coastal Plain: Depositional systems, structural framework, and hydrocarbon distribution: *AAPG Bulletin*, 66, 649-688.
- Hardage, B. A., Levey, R. A., Pendleton, V., Simmons, J., and Edson, R., 1994, A 3-D seismic case history evaluating fluviially deposited thin-bed reservoir in a gas-producing property: *Geophysics*, 59, 1650-1665.
- Khaidukov, V., Landa, E., and Moser, T. J., 2004, Diffraction imaging by focusing-defocusing: An outlook on seismic super-resolution: *Geophysics*, 69, 1478-1490.
- Le Rousseau, J. H., and de Hoop, M. V., 2001, Modeling and Imaging with the scalar generalized-screen algorithms in isotropic media: *Geophysics*, 66, 1551-1568.
- Moser, T. J., and Howard, C. B., 2008, Diffraction imaging in depth: *Geophysical Prospecting*, 56, 627-641.
- Schneider, W. A., 1978, Integral formulation for migration in two and three dimensions: *Geophysics*, 43, 49-76.

- Stoffa, P. L., Fokkema, J. T., de Luna Freire, R. M., and Kessinger, W. P., 1990, Split-step Fourier migration: *Geophysics*, 55, 410-421.
- Sturzu, I., Popovici, A. M., Musat, I., Tamushev, N., and Moser, T. J., 2012, High Resolution Diffraction Imaging of Small Scale Fractures in Thin Shale Layers: Internal Report, Z-Terra, Inc.
- Sturzu, I., Popovici, A. M., and Musat, I., 2013, ZTK Software Manual. Z-Terra, Inc.
- Sturzu, I., Popovici, A. M., Tamushev, N., Musat, I., Pelissier, M. A., and Moser, T. J., 2013, Specularity gathers for diffraction imaging: Extended Abstract, 75<sup>th</sup> EAGE Conference & Exhibition, London, England.
- Taner, M. T., Fomel, S., and Landa, E., 2006, Separation and imaging of seismic diffractions using plane-wave decomposition, 76<sup>th</sup> SEG meeting, New Orleans, Louisiana, USA, Expanded Abstracts, 2401.

